

Validation of neutrino energy estimation using electron scattering data

M. Khachatryan¹ and L. Weinstein¹

¹Old Dominion University, Norfolk, VA 23529

November 10, 2017

Abstract

To study neutrino oscillations the knowledge of the neutrino initial energy is required. This energy cannot be determined directly because neutrino beams have a broad energy distribution. Instead the initial energy is estimated from the final state particles. It can be determined from the total energy of all the final state particles. Alternatively, if the neutrino scatters from a free nucleon at rest, then the initial energy can be calculated using the scattered angle and the energy of the outgoing charged lepton. However this is not the case in real experiments, where nuclei such as argon, iron, carbon or other heavy nuclei are used to have higher interaction rates.

We have applied the methods of neutrino energy estimation to the Jefferson Lab CLAS electron scattering data and show how well we can reconstruct the beam energy from the scattered electron alone and from the scattered electron plus proton for a variety of targets and beam energies.

Contents

1	Introduction	5
2	Particle detection	7
2.1	Electron identification	7
2.2	Proton identification	16
2.3	Pion identification	17
2.4	Photon identification	18
2.5	Electron momentum corrections	18
2.6	Proton Energy Loss Correction	21
2.7	Electron fiducial cuts	21
2.8	Proton fiducial cuts	22
2.9	Z-vertex correction and cuts of protons and electrons	25
3	Physics analysis	30
3.1	Electron and neutrino scattering from nuclei	31
3.2	Analysis of CLAS6 data	33
4	To summarize	48

A Appendix

52

A.1	Z-vertex correction and cuts of protons and electrons for ^4He , ^{12}C and ^{56}Fe targets for 2.2 GeV and 4.4 GeV beam energies.	52
A.2	The $A(e, e')$ and $A(e, e'p)$ analysis plots for ^4He and ^{12}C targets for 2.2 GeV and 4.4 GeV beam energies.	60

List of Figures

1	The neutrino oscillation signal as function of distance traveled divided by the neutrino energy from the KamLand experiment.	6
2	The ratio of the total energy deposited in the calorimeter over the momentum for the electron at 4.4 GeV.	8
3	The energy deposited in the inner layer of the calorimeter for the electron candidates at 4.4 GeV.	9
4	The total energy deposited in the calorimeter for the electron candidates at 4.4 GeV. . . .	9
5	The ratio of the total energy deposited in the calorimeter over the momentum for the electron candidates at 2.2 GeV.	10
6	The energy deposited in the inner layer of calorimeter with the cut for the electron candidates at 2.2 GeV.	10
7	The total energy deposited in the calorimeter for the electron candidates at 2.2 GeV. . . .	11
8	The distribution of the angle between a CC hit and the nearest SC hit at 2.2 GeV.	11
9	The time difference between hits of the electron candidate in CC and SC, corrected for the distance traveled from CC to SC at 2.2 GeV.	12
10	The distribution of the number of photo-electrons detected in the CC at 2.2 GeV.	13
11	Beta from the SC vs momentum from the DC for positively charged particles at 4.4 GeV. . .	14
12	Beta from the SC vs momentum from the DC for particles with proton ID at 4.4 GeV. . .	14
13	The Δt plot as a function of momentum for positive particles at 4.4 GeV.	15
14	Beta from the SC vs momentum from the DC for positively charged particles at 2.2 GeV. . .	15
15	Beta from the SC vs momentum from the DC for particles with proton ID at 2.2 GeV. . .	16
16	The plot of Δt as a function of momentum from the DC for positive particles with proton ID at 2.2 GeV.	16
17	The ratio of the corrected and uncorrected electron momentum. There is a peak at 1 because the correction function works only for $\theta_e > 16$ Deg.. The results are shown for the ^3He target at 4.4 GeV.	19
18	The ratio of the corrected and uncorrected electron momentum at 2.2 GeV.	19
19	The ratio of proton momentum after the energy loss correction over the one before the correction at 4.4 GeV.	20
20	The ratio of proton momentum after the energy loss correction over the one before the correction. The results are shown for the ^3He target at 2.2 GeV.	20
21	The distributions for the electron EC local coordinates for sector 1 at 4.4 GeV.	23
22	The θ vs ϕ distributions for electrons for two momentum bins before and after fiducial cuts.	24
23	The distributions of the electron EC local coordinates for sector 5 at 2.2 GeV.	25
24	The θ vs ϕ distributions of the electron for two momentum bins before and after fiducial cuts at 2.2 GeV.	26
25	The θ vs ϕ distributions for the proton before and after fiducial cuts at 4.4 GeV.	27
26	The θ vs ϕ distributions for the proton before and after fiducial cuts at 2.2 GeV.	27

27	Vertex correction function for ${}^3\text{He}$ at 4.4 GeV	28
28	The ϕ angle of the electrons plotted vs the z component of the vertex for the ${}^3\text{He}$ target at 4.4 GeV.	28
29	Electron z vertex for ${}^3\text{He}$ at 4.4 GeV	29
30	The electron and proton z vertex difference for ${}^3\text{He}$ at 4.4 GeV	29
31	Vertex correction function for ${}^3\text{He}$ at 2.2 GeV	30
32	The ϕ angle of the electrons plotted vs the z component of the vertex for the ${}^3\text{He}$ target at 2.2 GeV.	30
33	Electron z vertex for ${}^3\text{He}$ at 2.2 GeV	31
34	The electron and proton z vertex difference for ${}^3\text{He}$ at 2.2 GeV	31
35	The diagrams of QE scattering of an electron on a nucleon and CC QE scattering of a neutrino on a nucleon.	32
36	The diagrams of different two-body interactions of electrons in a nucleus.	33
37	Current neutrino sources as a function of neutrino energy.	34
38	The θ vs ϕ angular distribution of e^- , π^+ , π^- and protons for ${}^3\text{He}$ at 4.4 GeV.	36
39	Multiplicity distributions of π^\pm for ${}^3\text{He}$ and ${}^{56}\text{Fe}$ targets at 4.4 GeV.	37
40	Multiplicity distributions of protons for ${}^3\text{He}$ and ${}^{56}\text{Fe}$ targets at 4.4 GeV.	37
41	Reconstructed energy E_{rec} as a function of the total perpendicular momentum for the scattered electron and the knockout nucleon system before and after pion rejection cuts at 4.4 GeV.	38
42	Reconstructed energy E_{rec} after different cuts at 4.4 GeV.	39
43	The diagrams for the pion and proton rotation around the three momentum transfer (\vec{q}) for the estimation of events with undetected pions in $A(e, e')$ and $A(e, e'p)$ analysis.	39
44	Reconstructed energy E_{rec} of $A(e, e')$ no pion spectrum before and after subtraction for undetected pions for different targets at 4.4 GeV.	40
45	E_{rec} and E_{tot} distributions of $A(e, e'p)$ no pion spectrum before subtraction for undetected pions, after subtraction for undetected pions and after subtraction for undetected pions and undetected two proton events for different targets at 4.4 GeV.	41
46	E_{rec} distributions of $A(e, e')$ and $A(e, e'p)$ no pion spectrum and E_{tot} distribution of $A(e, e'p)$ no pion spectrum after subtraction for undetected pions and undetected protons for different targets at 4.4 GeV.	42
47	E_{tot} and E_{rec} distributions of $A(e, e'p)$ no pion spectrum after subtraction for undetected pions and undetected protons for different regions of p_{perp} for different targets at 4.4 GeV.	43
48	The θ vs ϕ angular distribution of e^- , π^+ , π^- and protons for ${}^3\text{He}$ at 2.2 GeV.	44
49	Multiplicity distributions of π^\pm for ${}^3\text{He}$ and ${}^{56}\text{Fe}$ targets at 2.2 GeV.	45
50	Multiplicity distributions of protons for ${}^3\text{He}$ and ${}^{56}\text{Fe}$ targets at 2.2 GeV.	45
51	Reconstructed energy E_{rec} as a function of the total perpendicular momentum for the scattered electron and the knockout nucleon system before and after pion rejection cuts at 2.2 GeV.	46
52	Reconstructed energy E_{rec} after different cuts at 2.2 GeV.	47
53	Reconstructed energy E_{rec} of $A(e, e')$ no pion spectrum before and after subtraction for undetected pions for different targets at 2.2 GeV.	48
54	E_{rec} and E_{tot} of $A(e, e'p)$ no pion spectrum before subtraction for undetected pions, after subtraction for undetected pions and after subtraction for undetected pions and undetected two proton events for different targets at 2.2 GeV.	49

55	E_{rec} distributions of $A(e, e')$ and $A(e, e'p)$ no pion spectrum and E_{tot} distribution of $A(e, e'p)$ no pion spectrum after subtraction for undetected pions and undetected protons for different targets at 2.2 GeV.	50
56	E_{tot} and E_{rec} distributions of $A(e, e'p)$ no pion spectrum after subtraction for undetected pions and undetected protons for different regions of p_{perp} for different targets at 2.2 GeV. .	51
57	E_{rec} distributions of $A(e, e')$ and $A(e, e'p)$ no pion spectrum and E_{tot} distribution of $A(e, e'p)$ no pion spectrum after subtraction for undetected pions and undetected protons for all targets at 2.2 GeV and 4.4 GeV.	54
58	The ϕ angle of the electrons plotted vs z component of vertex for ^4He target at 4.4 GeV. .	55
59	The distributions of electron z vertex and electron and proton z vertex differences for ^4He at 4.4 GeV	55
60	The ϕ angle of the electrons plotted vs z component of vertex for ^4He target at 4.4 GeV. .	56
61	The distributions of electron z vertex and electron and proton z vertex differences for ^{12}C at 4.4 GeV	56
62	The ϕ angle of the electrons plotted vs z component of vertex for ^{56}Fe target at 4.4 GeV. .	57
63	The distributions of electron z vertex and electron and proton z vertex differences for ^{56}Fe at 4.4 GeV	57
64	The ϕ angle of the electrons plotted vs z component of vertex for ^4He target at 2.2 GeV. .	58
65	The distributions of electron z vertex and electron and proton z vertex differences for ^4He at 2.2 GeV	58
66	The ϕ angle of the electrons plotted vs z component of vertex for ^4He target at 2.2 GeV. .	59
67	The distributions of electron z vertex and electron and proton z vertex differences for ^{12}C at 2.2 GeV	59
68	The ϕ angle of the electrons plotted vs z component of vertex for ^{56}Fe target at 2.2 GeV. .	60
69	The distributions of electron z vertex and electron and proton z vertex differences for ^{56}Fe at 2.2 GeV	60
70	The ϕ angle of the electrons plotted vs z component of vertex for ^{56}Fe target at 2.2 GeV for runs with exploded target.	61
71	The distributions of electron z vertex and electron and proton z vertex differences for ^{56}Fe at 2.2 GeV for runs with exploded target.	61
72	Multiplicity distributions of π^\pm for ^4He and ^{12}C targets at 4.4 GeV.	62
73	Multiplicity distributions of protons for ^4He and ^{12}C targets at 4.4 GeV.	62
74	Reconstructed energy E_{rec} as a function of the total perpendicular momentum for the scattered electron and the knockout nucleon system before and after pion rejection cuts at 4.4 GeV.	63
75	Reconstructed energy E_{rec} after different cuts at 4.4 GeV.	64
76	Reconstructed energy E_{rec} of $A(e, e')$ no pion spectrum before and after subtraction for undetected pions for different targets at 4.4 GeV.	65
77	E_{rec} and E_{tot} of $A(e, e'p)$ no pion spectrum before subtraction for undetected pions, after subtraction for undetected pions and after subtraction for undetected pions and undetected two proton events for different targets at 4.4 GeV.	66
78	E_{tot} and E_{rec} distributions of $A(e, e'p)$ no pion spectrum after subtraction for undetected pions and undetected protons for different regions of p_{perp} for different targets at 4.4 GeV. .	67
79	Multiplicity distributions of π^\pm for ^4He and ^{12}C targets at 2.2 GeV.	68
80	Multiplicity distributions of protons for ^4He and ^{12}C targets at 2.2 GeV.	68

81	Reconstructed energy E_{rec} as a function of the total perpendicular momentum for the scattered electron and the knockout nucleon system before and after pion rejection cuts at 2.2 GeV.	69
82	Reconstructed energy E_{rec} after different cuts at 2.2 GeV.	70
83	Reconstructed energy E_{rec} of $A(e, e')$ no pion spectrum before and after subtraction for undetected pions for different targets at 2.2 GeV.	71
84	E_{rec} and E_{tot} of $A(e, e'p)$ no pion spectrum before subtraction for undetected pions, after subtraction for undetected pions and after subtraction for undetected pions and undetected two proton events for different targets at 2.2 GeV.	72
85	E_{tot} and E_{rec} distributions of $A(e, e'p)$ no pion spectrum after subtraction for undetected pions and undetected protons for different regions of p_{perp} for different targets at 2.2 GeV. .	73

List of Tables

1	Cut values on the time difference between hits of the electron candidate in CC and SC, corrected for the distance traveled from CC to SC for different sectors of CLAS.	13
2	The table of cut values on the u , v , w EC local coordinates of an electron for different sectors of CLAS, used to select fiducial region used for the 2.2 GeV analysis.	22
3	The cut values on the electron z vertex, and the difference between the vertexes of the electron and the proton for different targets and beam energies. These cut values are used to select particles that are coming from the target region and correspond to the same event.	32
4	Number of good (e, e') and $(e, e'p)$ events.	35
5	Fraction of events reconstructed within 5% of beam energy at 2.2 GeV and 4.4 GeV analysis.	47
6	Fraction of events reconstructed within 10% of beam energy at 2.2 GeV and 4.4 GeV analysis.	52
7	Fraction of events reconstructed within 20% of beam energy at 2.2 GeV and 4.4 GeV analysis.	52

1 Introduction

Neutrinos created by charged current weak interactions are in electron, muon or tau flavor eigenstates. The “flavor states” don’t have well defined masses, but instead are superpositions of mass eigenstates. As the neutrinos travel away from their source, they can change flavor or oscillate.

In neutrino oscillation experiments the neutrino beam travels a long distance (about few hundred meters) before it reaches the detector, where its flavor composition is studied after it interacts with target material. Experiments that are interested in this type of physics include ongoing MINER ν a (US, Fermilab), Microboone (US, Fermilab), Tokai-to-Kamioka (T2K) (Japan) and NO ν A (US, Fermilab) as well as future Hyper-Kamiokande (HK)(Japan) and Deep Underground Neutrino Experiment (DUNE) (US, Fermilab), where the beam will travel 1300 km before it reaches the detector at Sanford Underground Research Laboratory.

Experiments that study neutrino oscillations as well as nucleon weak form factors, scatter neutrinos from nucleons in nuclei. They are particularly interested in quasi-elastic (QE) scattering of a neutrino from a bound nucleon via neutral current (NC) mediated by the Z boson $\nu + N \rightarrow \nu + N$ or scattering via charged currents (CC) mediated by W^+ , W^- bosons : $\nu_l + n \rightarrow l^- + p$ or $\bar{\nu}_l + p \rightarrow l^+ + n$, as in this reactions nucleon comes out intact and the two body nature of the interaction allows the kinematics to be fully reconstructed from the outgoing particles.

To study neutrino oscillations the knowledge of the neutrino initial energy is required. The neutrino oscillation parameters are determined from the fit to the neutrino oscillation signal, which is usually

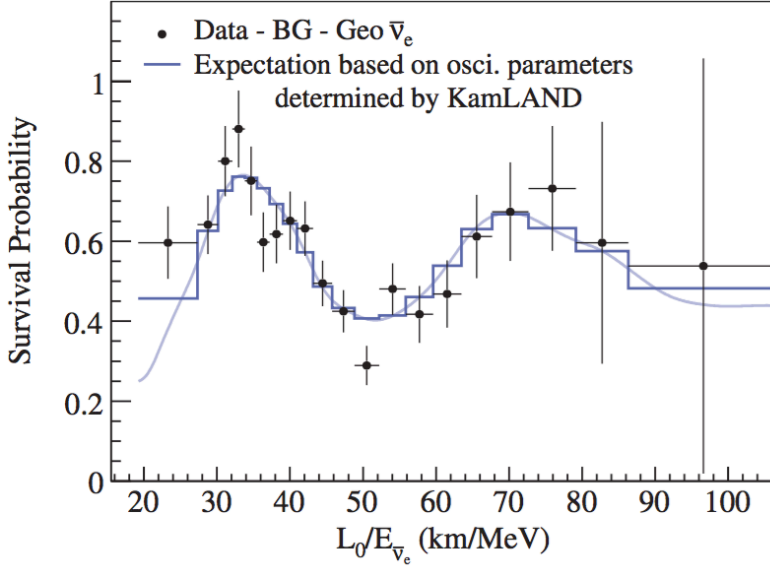


Figure 1: The neutrino oscillation signal as function of distance traveled divided by the neutrino energy from the KamLAND experiment [1].

plotted as a function of distance traveled divided by the energy of neutrino (see Fig. 1). If the energy is not precisely known, than the oscillation signal will be washed-out, and obtained oscillation parameters will have an error.

Neutrino initial energy can't be measured directly because neutrino beams are not monoenergetic. They are made by scattering protons on nuclei to create mesons (pions, kaons) that decay to a neutrino (anti-neutrino) with corresponding anti lepton (lepton). For example π^+ decays into μ^+ and ν_μ , while π^- decays into μ^- and $\bar{\nu}_\mu$. The mixed beam then passes through a thick absorber until the charged particles stop leaving a pure neutrino plus anti-neutrino beams.

The initial neutrino energy in the above mentioned reactions can be determined from the total energy of all the final state particles.

On the other hand if we assume that the neutrino scatters from a free nucleon at rest then the initial energy can be calculated using the scattered angle and the energy of the outgoing charged lepton. However this is not the case in real experiments, where nuclei such as argon, iron, carbon or other heavy nuclei are used to have higher interaction rates.

The energy sum method is complicated as the detectors have limited acceptances, and are not sensitive to certain types of particles. While calorimetric-detector based neutrino experiments rely on this method, neutrino experiments that use water Cherenkov-detectors are not capable to detect both the outgoing lepton and nucleon, instead they only detect the outgoing lepton and try to reconstruct the kinematics by looking at quasi-elastic scattering samples.

Also both methods might contain an error as the outgoing hadrons might re-interact within the target, Final State Interaction might occur (FSI), modifying the kinematics and the number of final state particles.

Based on the second method, if we ignore the recoil momentum and approximate the energy of the residual nuclear system by a constant, we can obtain the following expression for the neutrino energy:

$$E_\nu = \frac{2M\epsilon - m_l^2 + 2ME_l}{2(M - E_l + |k_l| \cos \theta)} \quad (1)$$

where M is the nucleon mass, ϵ is the single-nucleon separation energy, m_l is the mass of the outgoing lepton, k_l is its momentum, E_l is its energy and θ is the angle between the outgoing lepton and the direction

of the neutrino beam.

Both neutrino energy reconstruction techniques have never been tested with a beam of known energy. They are usually tested using simulations, which use neutrino “event generators” to simulate neutrino interactions. These event generators include information on various neutrino interaction processes for different targets and beam energies and themselves need to be tested against real data.

Based on the fact that electrons and neutrinos are both leptons and thus interact with matter in similar ways, in the following analysis we use electron-nucleon scattering data to study neutrino beam energy reconstruction. As the electron beam energy is known, we can test energy reconstruction in selective kinematics and identify regions of phase space where simulation and data agree well. This will allow to test and improve the existing neutrino event generators that are used in neutrino experiments and can decrease the systematic uncertainties in current and future neutrino experiments.

2 Particle detection

We have analyzed JLab (Thomas Jefferson Nation Accelerator Facility) Hall-B e2a experiment data collected at 4.461 GeV and 2.261 GeV beam energies with ^3He , ^4He , ^{12}C and ^{56}Fe targets. This was done to test how well do the above mentioned neutrino beam energy reconstruction techniques describe the electron beam energy.

This data has already been published in .

This analysis note briefly reviews the cuts and corrections used in approved analysis [2], [3]. These include electron, proton and pion identification cuts, electron momentum correction analysis, proton energy loss correction analysis, fiducial cuts and vertex corrections.

2.1 Electron identification

4.4 GeV analysis

The triggering particle used in the event reconstruction in CLAS electro-production data analysis is the electron, so it is crucial to have an accurate electron identification. This identification is done in few steps, by suppressing mainly the charged pion contribution.

In the current analysis we are using the algorithm from [3] for electron identification that was already reviewed and approved.

In order to record the event in the initial data processing it was required that the event has at least one negatively charged track with a corresponding shower in the EC (Electromagnetic Calorimeter) and a hit in the SC (Scintillator Counter) that geometrically matched the one in the EC. The CC was not used at 4.4 GeV to not limit the geometrical acceptance.

This initial electron selection is very loose and further electron selection cuts need to be applied for proper identification.

We take the advantage of the fact that the electron deposits its entire energy in the EC and that we are able to detect a certain fraction of it by means of scintillation light, giving a rise to sampling fraction. This sampling fraction depends on the relative amount of scintillator and lead in the EC, as the scintillation light is collected only in scintillator regions. The sampling fraction is about 0.27 for electron momenta above 0.2 GeV and drops below that. We cut 3σ around the electron band of the ratio of total energy deposited in the EC divided by momentum plotted as a function of momentum, to select events with E_{tot}/p about the sampling fraction, and to suppress the contribution of the accidental background. The

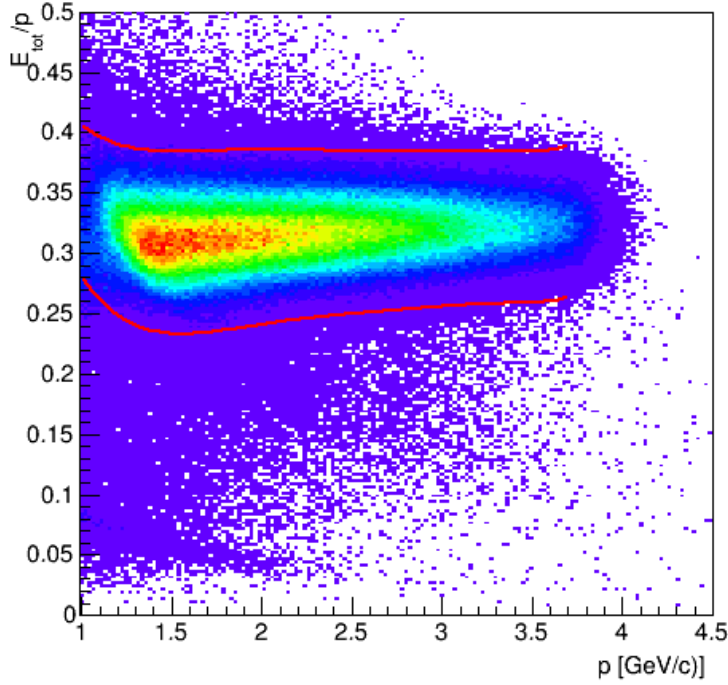


Figure 2: The ratio of the total energy deposited in the calorimeter over the momentum for the electron candidates. The two lines show the 3σ cut around the electron band. The plot is made for the ^3He target at 4.4 GeV after fiducial cuts were applied.

corresponding plot is shown in Fig. 2. We take the total energy deposit in the entire EC or the sum of the total energies deposited in the inner and outer layers of the EC, whichever is the largest.

The parameters of the fit to the sampling fraction band were stored as a function of electron momentum, and for each electron candidate the corresponding lower and upper limits of E_{tot}/p ratio were obtained which determined the acceptable region.

Another cut is made on the energy deposited in the inner layer of the EC for the electron candidate to be greater than 55 MeV. This cut helps to separate electrons from minimum ionizing particles such as pions. Unlike the electrons, which make a shower inside the EC and thus deposit all their energy, the energy that pions deposit in each scintillator layer of the EC is constant and depends only on the thickness and the material of the scintillator and is smaller compared to the energy deposited by electrons. The distribution of the energy deposited in the inner layer of the EC is shown in Fig. 3. The vertical line shows the applied cut. The pion peak at $E_{\text{inner}} \sim 0.03$ GeV was fit with a Gaussian and it was found that the applied cut is about 3.5σ away from the pion peak.

We also cut on the total energy deposited by an electron candidate, because the EC trigger threshold was set high. The EC threshold is set to reject pions that leave little energy in the calorimeter compared to electrons. However, some pions still pass the threshold and get detected. We applied a cut on $E_{\text{tot}} > 0.33$ GeV and the electron candidate momentum $p > 1.1$ GeV identical to those in the previous CLAS approved analysis [3]. The corresponding distribution is shown for E_{tot} in Fig. 4.

We did not apply cuts on any parameters measured by Cerenkov Counters (CC) in the 4 GeV analysis [3] however we required the electron candidate to have an associated signal in CC.

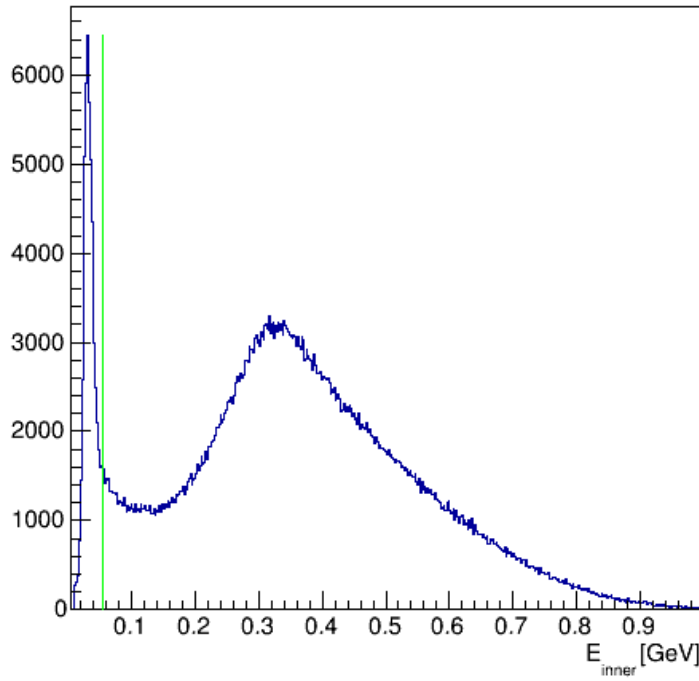


Figure 3: The energy deposited in the inner layer of the calorimeter with a cut (green line) for the electron candidates. The results are shown for the ^3He target at 4.4 GeV after fiducial cuts were applied.

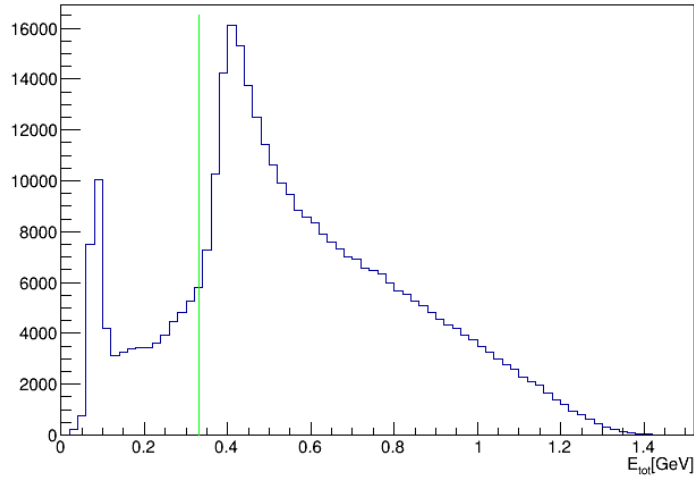


Figure 4: The total energy deposited in the calorimeter for the electron candidates. The results are shown for the ^3He target at 4.4 GeV after fiducial cuts were applied.

2.2 GeV analysis

For the 2.2 GeV analysis we have applied electron PID cuts similar to those at 4.4 GeV. However, unlike to the 4.461 GeV analysis, here we apply also a cut on CC. This is very helpful in separating electrons from pions, as at this energy all of the charged pions have their momentum below the 2.2 GeV CC detection threshold.

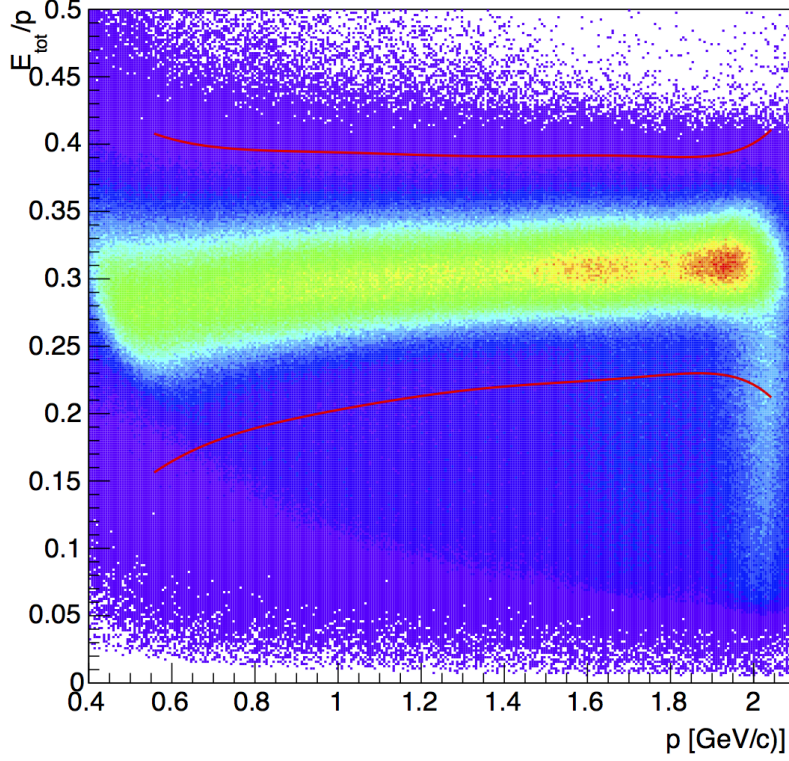


Figure 5: The ratio of the total energy deposited in the calorimeter over the momentum for the electron candidates. The two lines show the 3σ cut around the electron band. The results are shown for the ^3He target at 2.2 GeV, by looking at negative particles with EC, CC and SC status, after fiducial cuts were applied.

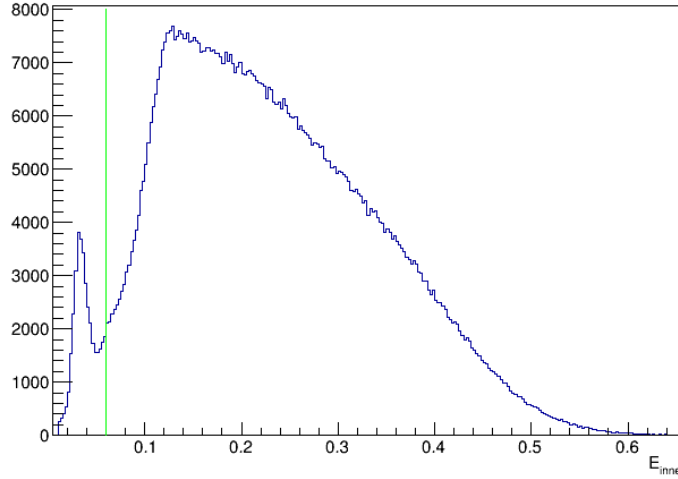


Figure 6: The energy deposited in the inner layer of calorimeter with the cut (green line) for the electron candidates. The results are shown for the ^3He target at 2.2 GeV, by looking at negative particles with EC and SC status, after fiducial cuts were applied.

For the calorimeter, similar to the 4.461 GeV analysis, we have applied a 3σ cut around the electron band in the plot of the ratio of total energy deposited in the EC divided by momentum plotted as a

function of momentum. The distribution with the corresponding cut is shown in Fig. 5.

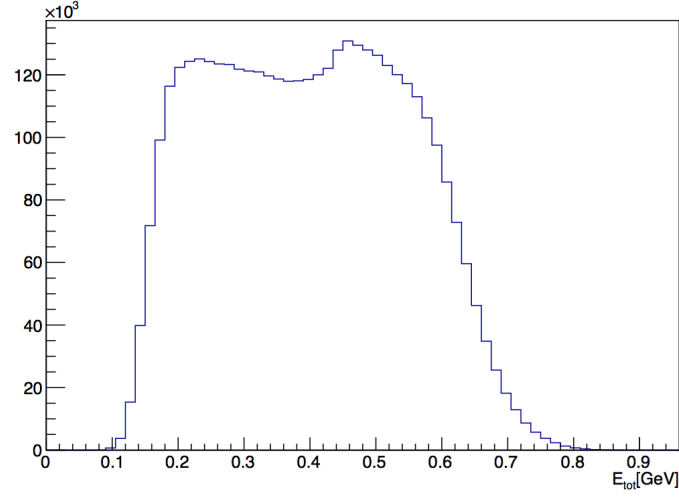


Figure 7: The total energy deposited in the calorimeter for the electron candidates after all electron PID cuts. The results are shown for the ^3He target at 2.2 GeV.

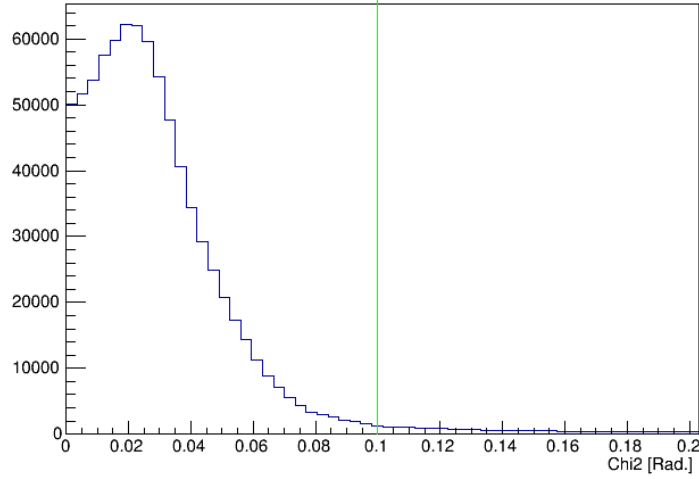
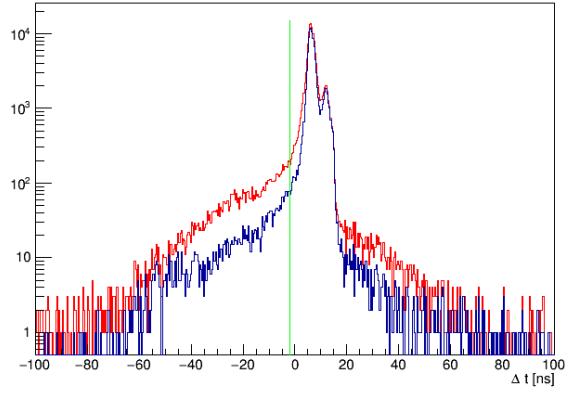
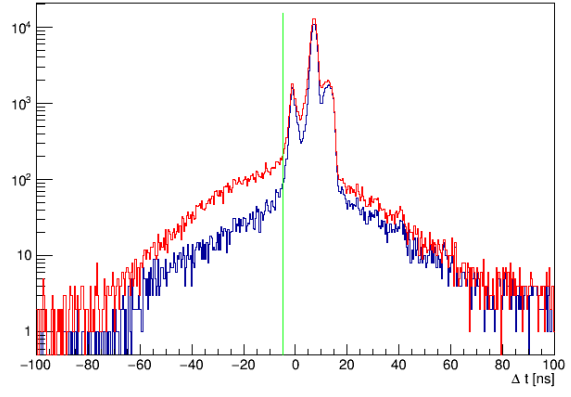


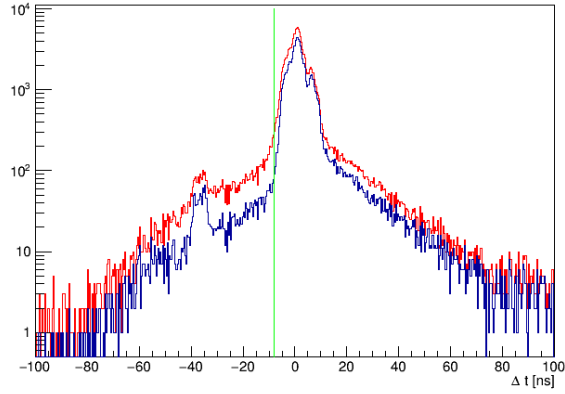
Figure 8: The distribution of the angle between a CC hit and the nearest SC hit. The green line corresponds to the applied cut value. The results are shown for the ^3He target at 2.2 GeV after fiducial cuts were applied.



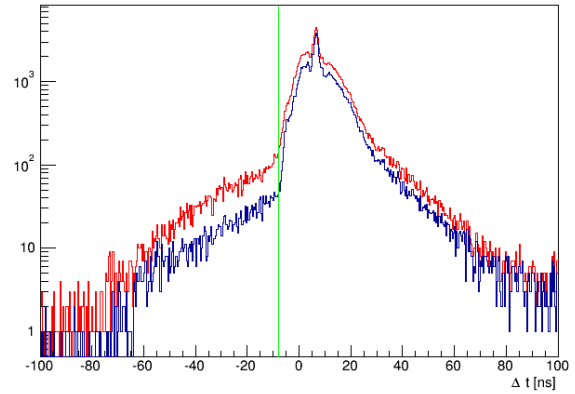
(a) Sector one.



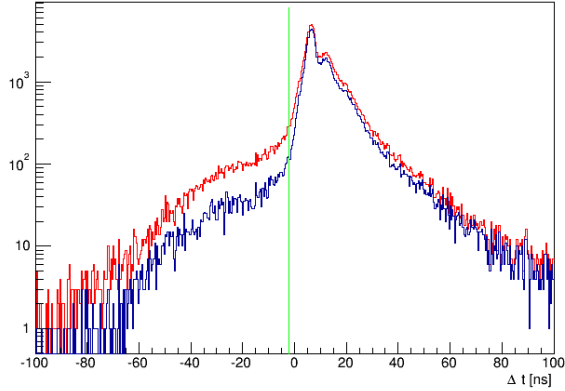
(b) Sector two.



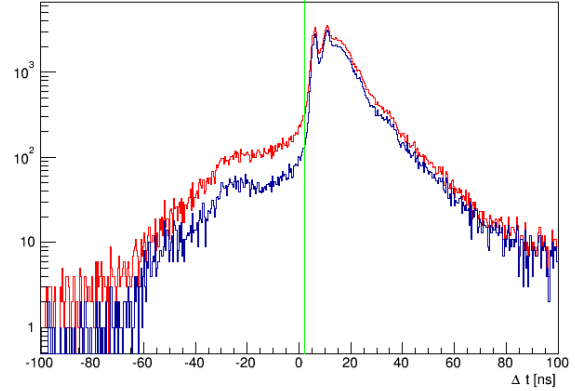
(c) Sector three.



(d) Sector four.



(e) Sector five.



(f) Sector six.

Figure 9: The time difference between hits of the electron candidate in CC and SC, corrected for the distance traveled from CC to SC before (red) and after (blue) a **pion rejection cut ($N_{p\pi} > 2.5$ at the CC)**. The green lines show the applied cut values. The results are shown for the ^3He target at 2.2 GeV after fiducial cuts were applied.

We also **cut on the energy deposited in the inner layer of the EC to be greater than 0.06 GeV**. We have fit the pion peak with a Gaussian and found that the applied cut is nearly 3.5σ away from the pion

peak position, and the contamination of the pions in the cut regions is 0.0005%. The distribution of the energy deposited in the inner layer of the EC with the corresponding cut is shown in Fig. 6.

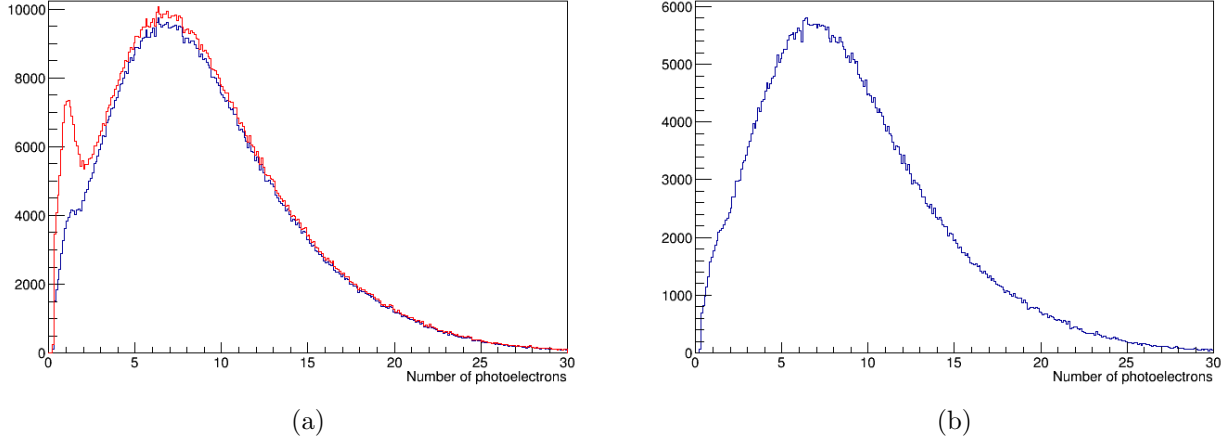


Figure 10: The distribution of the number of photo-electrons detected in the CC before other CC cuts (red) and after other CC cuts (blue) (left plot). The plot on the right shows the same distribution after all electron PID cuts. The results are shown for the ^3He target at 2.2 GeV after fiducial cuts were applied.

We did not apply a cut on the total energy deposited in the calorimeter, however, we cut on the momentum of the electron candidate to be greater than 0.55 GeV/c. The distribution of the total deposited energy in the calorimeter for the electron candidates after all the above mentioned cuts is shown in Fig. 7. It is clear from the plot that there is no need to apply an additional cut on E_{tot} . We also require the electron candidate momentum to be less than the beam energy to eliminate few events that show up at higher momenta.

Sector	Δt_{CC}
1	-2 ns
2	-5 ns
3	-8 ns
4	-8 ns
5	-2 ns
6	2 ns

Table 1: Cut values on the time difference between hits of the electron candidate in CC and SC, corrected for the distance traveled from CC to SC for different sectors of CLAS.

In addition to the above mentioned cuts, we have applied matching cuts between the hits of an electron candidate in the SC and CC following the electron identification procedure done in [4]. These cuts are new for e2a. We have required that the time difference between hits of the electron candidate in the CC and SC, corrected for the distance traveled from CC to SC (Δt_{CC}) was greater than a certain value, which is individual for each sector and was determined by looking at the Δt_{CC} distributions in each sector separately Fig. 9. The corresponding cut values are shown in Table 1. We have also applied a cut on the angle between a CC hit and the nearest SC hit to be ≥ 0.1 Rad. Fig. 8. The plot of the number of photo-electrons detected by the CC for a given electron candidate after the above mentioned two CC cuts

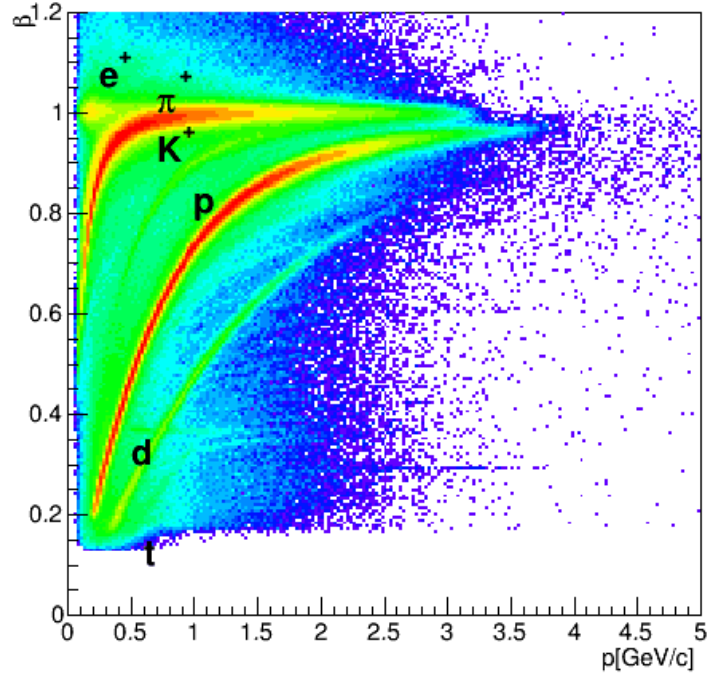


Figure 11: The logarithmic scale plot of beta from the SC vs momentum from the DC for positively charged particles. The results are shown for the ^3He target at 4.4 GeV.

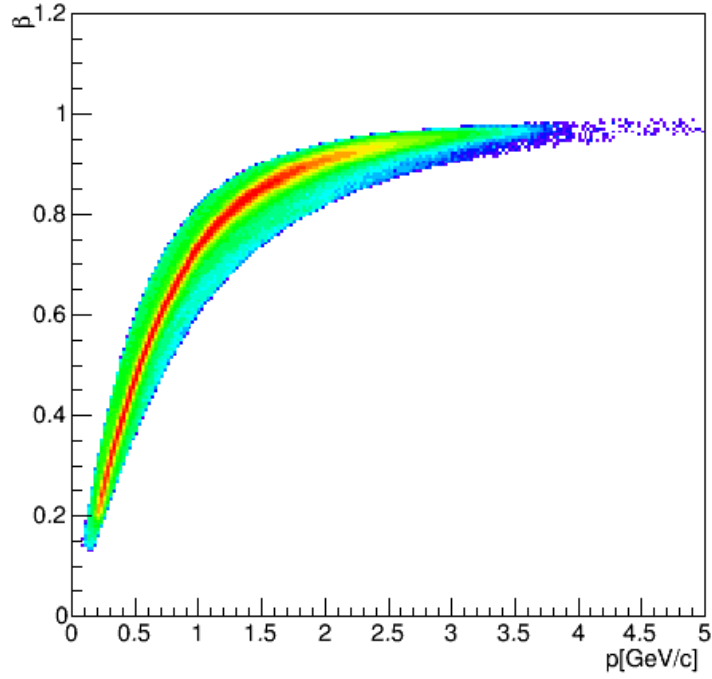


Figure 12: The logarithmic scale plot of beta from the SC vs momentum from the DC for particles with proton ID. The results are shown for the ^3He target at 4.4 GeV.

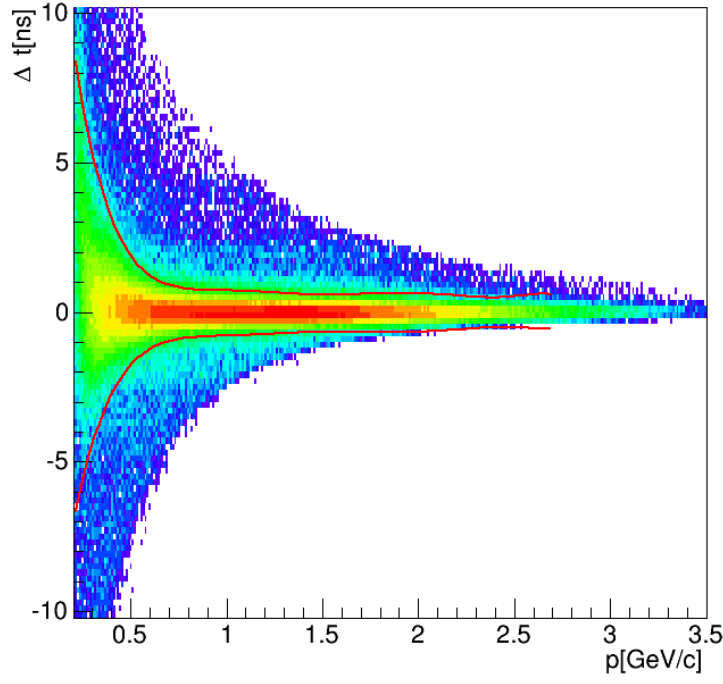


Figure 13: The logarithmic scale plot of the difference between the time of flight measured by the SC and the time of flight calculated using the path length and the velocity obtained from the momentum measured by the DC as a function of momentum from DC for positive particles with proton ID. The red line shows the 3σ PID cut. The results are shown for the ^3He target at 4.4 GeV.

is shown in Fig. 10a. The plot of the number of photo-electrons detected by the CC after all electron PID cuts is shown in Fig. 10b. It has the expected Poisson distribution form. It is clear that this cuts suppress the pion contribution at $N_{\text{phe}} < 2.5$, and there is no need for an additional pion rejection cut $N_{\text{phe}} > 2.5$.

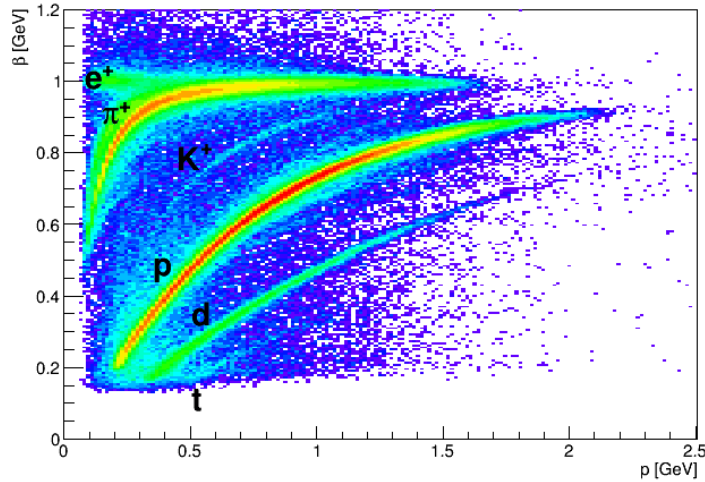


Figure 14: The logarithmic scale plot of beta from the SC vs momentum from the DC for positively charged particles. The results are shown for the ^3He target at 2.2 GeV.

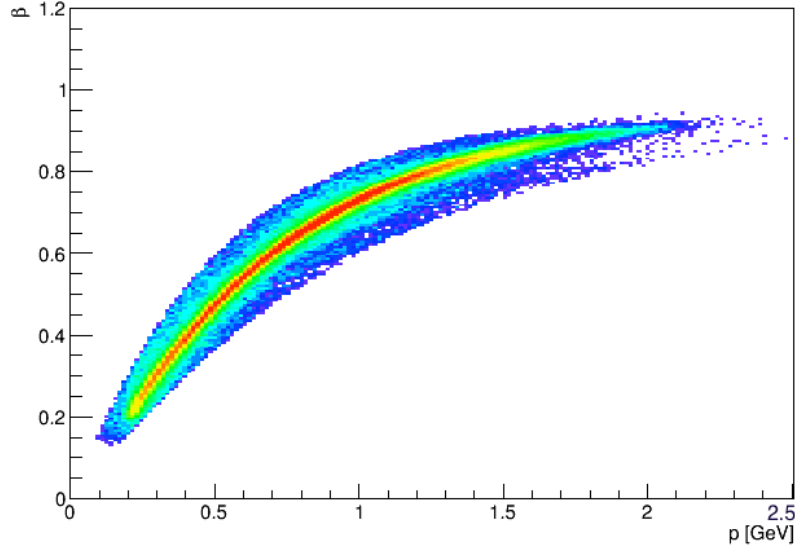


Figure 15: The logarithmic scale plot of beta from the SC vs momentum from the DC for particles with proton ID. The results are shown for the ^3He target at 2.2 GeV.

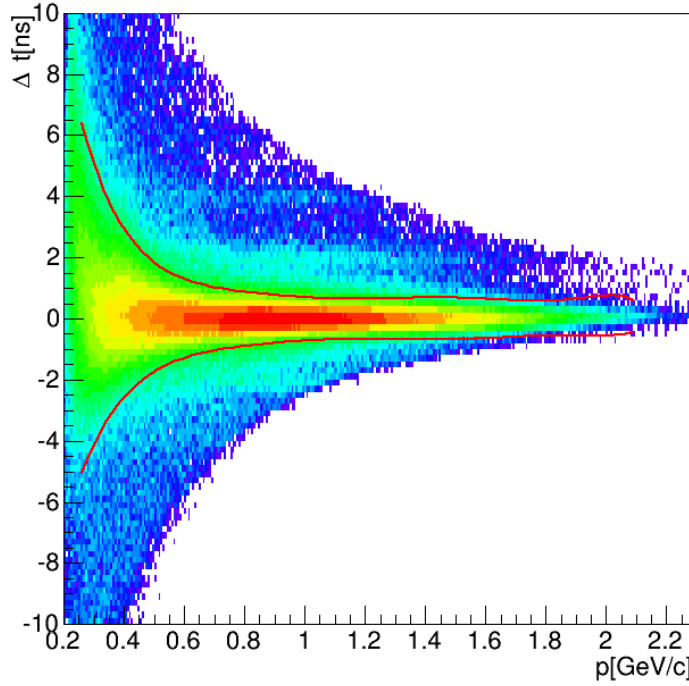


Figure 16: The logarithmic scale plot of the difference between the time of flight measured by the SC and the time of flight calculated using the path length and the velocity obtained from the momentum measured by the DC as a function of momentum from DC for positive particles with proton ID. The red line shows the 3σ PID cut. The results are shown for the ^3He target at the 2.2 GeV.

2.2 Proton identification

After selecting the electron, other charged particles in the event are identified by using the time of flight

information from the SC and the momentum obtained from the Drift Chambers together and the toroidal magnet field. Neutral particles are identified as the ones with a hit in the electromagnetic calorimeter and no associated charged track. For them the time information is being used to separate between neutrons and photons.

4.4 GeV analysis

For hadron identification in CLAS the time of flight information from the SC is used together with the momentum obtained using the DC with toroidal magnet. From both informations one can obtain the mass of the particle. Each particle is assigned a certain ID, by requiring that the difference $|\beta_{\text{measured}} - \beta_{\text{calculated}}|$ was minimal. This difference is between the particles' velocity obtained from the path length and the time information from the SC, β_{measured} , and the velocity obtained from the momentum using DC and the mass of the assigned type, $\beta_{\text{calculated}}$. The plots of the velocity measured by time of flight as a function of particle momentum for positive particles and for particles with proton ID is shown in Fig. 11 and Fig. 12, respectively. Different bands in the plot for positive particles correspond to positrons, pions, kaons, protons, deuterons and tritons.

We also checked the difference between the time of flight measured by the SC and the time of flight obtained from dividing the path length over the velocity obtained from the momentum measured by the DC for positive particles with proton ID. The difference Δt is expressed by

$$\Delta t = t_{\text{SC}} - \frac{r_{\text{SC}}}{\beta_{\text{DC}} * c} - t_{\text{trigger}} \quad (2)$$

where

$$\beta_{\text{DC}} = \frac{p}{\sqrt{p^2 + m_p^2}} \quad (3)$$

with c being the speed of light, t_{SC} and r_{SC} are the time and path length information from the SC, p is the momentum from the DC, t_{trigger} is the trigger time and m_p^2 is the proton mass. We have then applied a 3σ cut around the Δt (Eq. 2) band to select protons and eliminate particles coming from different beam bunches. The Δt distribution as a function of momentum for particles with the proton ID is shown in Fig. 13.

2.2 GeV analysis

An analysis similar to the one at 4.4 GeV was done to determine the proton PID cuts for the 2.2 GeV analysis. The plots of the velocity measured by the time of flight as a function of particle momentum for positive particles and for particles with proton ID are shown in Fig. 14 and Fig. 15, respectively. Again it was concluded that using the proton ID to select proton candidates provides a good pion separation and a 3σ cut needs to be applied around the proton band in the Δt vs momentum distribution that is centered around 0, to eliminate particles coming from different beam bunches, appearing as horizontal lines in Fig. 16.

2.3 Pion identification

4.4 GeV analysis

In the CLAS event reconstruction particles are assigned a preliminary ID by RECSIS/SEB (Simple Event builder in the framework of the CLAS reconstruction code) based on the comparison of the velocity

obtained from the Time Of Flight and the velocity from the DC used together with the toroidal magnet as a magnetic spectrometer.

In the current analysis we have used particle IDs assigned by SEB to select π^- and π^+ . Negative particles with ID = -211 that had a positive status and an associated information in DC and SC were chosen as π^- . In the same way positively charged particles with ID = 211 that had a positive status and an associated signal in DC and SC were chosen as π^+ .

We did not bother developing more sophisticated pion selection cuts as overestimation of pions is not an issue and would not affect the outcome of the current analysis.

2.2 GeV analysis

The pion selection at 2.2 GeV was done in the same way as for the 4.4 GeV analysis.

2.4 Photon identification

4.4 GeV analysis

Photons were selected by choosing the neutral particles with positive status, that had been detected in the EC or LAC (Large Angle Calorimeter), did not have associated signals in the DS or SC and had a velocity $\beta > 0.95$.

2.2 GeV analysis

The photon identification at 2.2 GeV is done in the same way as for the 4.4 GeV.

2.5 Electron momentum corrections

4.4 GeV analysis

The procedure for the momentum corrections in the 4.4 GeV analysis was derived in [5] and copied here. This correction is the one used in the CLAS approved analysis [2].

The electron momentum measurement has an error in it due to different factors, among which the largest contributions are inaccuracies in the precise knowledge of the torus magnetic field and the location of the drift chambers. This can shift the measured electron momentum from its correct value by typically 1 – 2%.

To study this shift and obtain a correction function, one can look at the electron elastic scattering of a H-target, where the momentum of the scattered electron can be reconstructed from the scattering angle and the known initial energy, under the assumption that the scattering angle is known precisely. Unfortunately, there was not a H-target run in the E2a experiment, so the hydrogen data taken during the previous E1 experiment was used.

For elastic scattering of hydrogen, the W invariant mass is expected to be equal to the proton mass ($W = 0.938$ GeV). Any shift from this value is a result of incorrect electron momentum reconstruction. The correct electron momentum was extracted by looking at the elastic scattering events and the ratio to the incorrect (measured) momentum was stored as a function of electron angles (θ_e) and (ϕ_e), momentum and magnetic field (coil current). The obtained correction function was then used to correct the electron

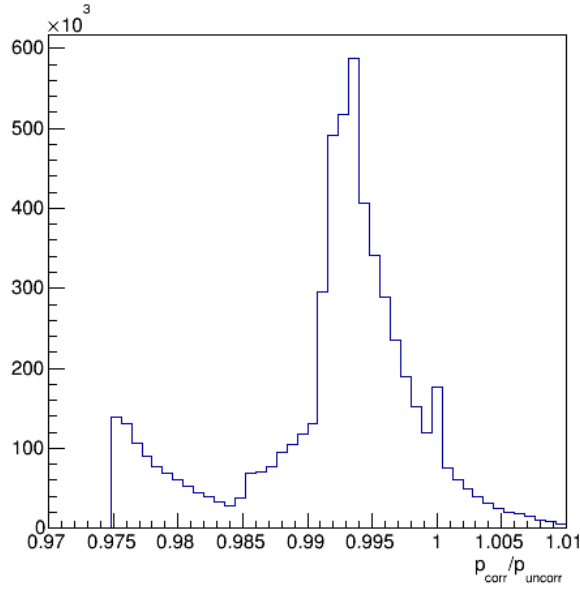


Figure 17: The ratio of the corrected and uncorrected electron momentum. There is a peak at 1 because the correction function works only for $\theta_e > 16$ Deg.. The results are shown for the ^3He target at 4.4 GeV.

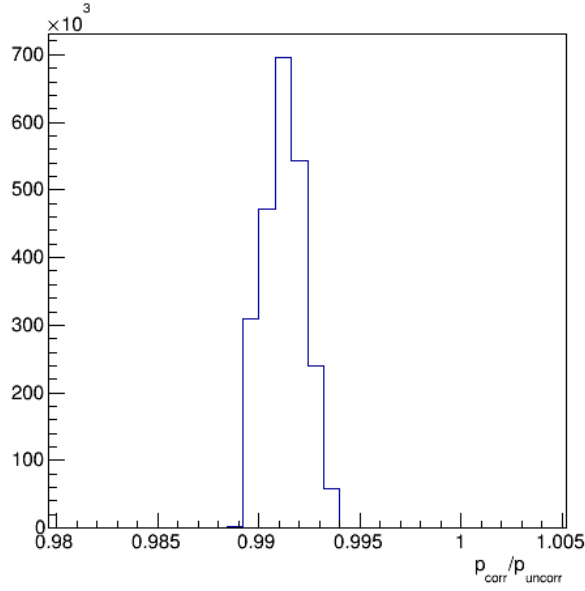


Figure 18: The ratio of the corrected and uncorrected electron momentum. The results are shown for the ^3He target at 2.2 GeV.

momentum, and an improvement was observed in the position and the resolution of the W invariant mass peak of the elastic scattering of a H-target [3], [6].

To make sure that the H data taken during the E1 experiment, works fine for the E2a data, studies were done, where the contribution of scattering of ^{12}C was subtracted from CH_2 scattering data to obtain data, similar to that of the scattering of hydrogen for the current experiment. Then the corresponding momentum correction function was obtained, which resulted in electron momentum corrections consistent to the ones obtained with actual H data.

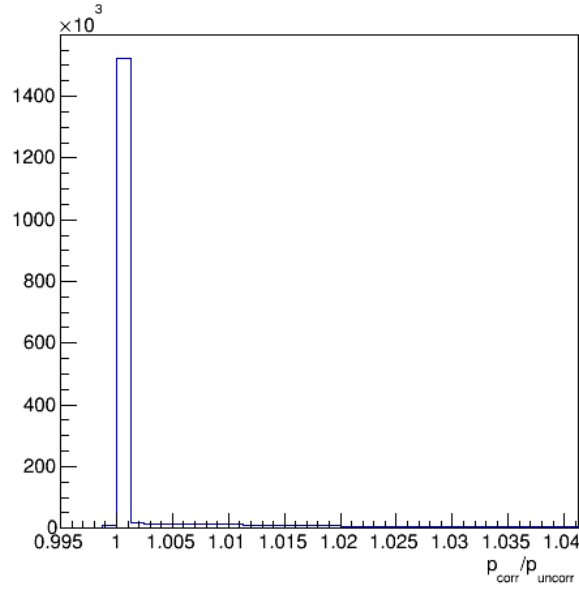


Figure 19: The ratio of proton momentum after the energy loss correction over the one before the correction. The results are shown for the ^3He target at 4.4 GeV.

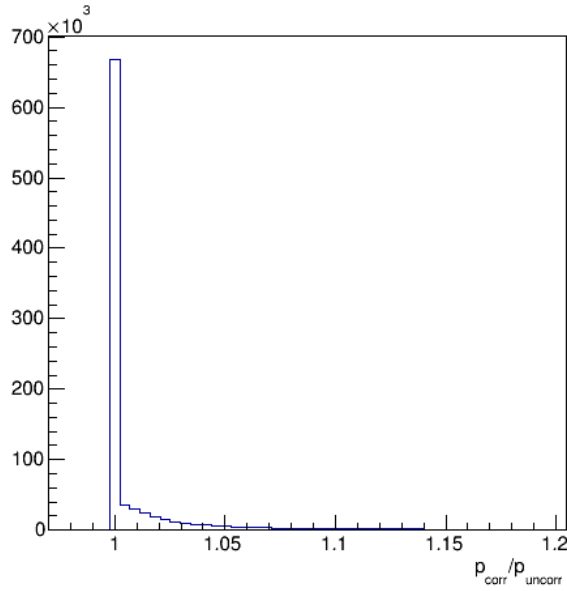


Figure 20: The ratio of proton momentum after the energy loss correction over the one before the correction. The results are shown for the ^3He target at 2.2 GeV.

Furthermore, the correction was applied to different kinematic regions to make sure that it works equivalently fine for other scattering regions (Δ etc.).

The ratio of the corrected electron momentum to the uncorrected one is shown in Fig. 17.

There is no need to apply a similar correction on the proton momentum, as protons have smaller momentum compared to electrons, and the error in the determination of their momentum is negligible.

The more detailed explanation of the procedure of obtaining electron momentum corrections at different beam settings can be found in [5].

2.2 GeV analysis

The procedure for the momentum corrections for the 2.2 GeV analysis was derived in [7] and again copied here. It is also the one used in CLAS approved analysis [3].

The electron momentum correction for the 2.2 GeV analysis is done in a similar way as for the 4.4 GeV analysis. The ratio of the corrected electron momentum to that of the uncorrected one for the 2.2 GeV analysis is shown in Fig. 18.

2.6 Proton Energy Loss Correction

4.4 GeV analysis

The proton energy loss correction function for the 4.4 GeV analysis is the same as the one used in the CLAS approved analysis [3].

Protons lose part of their energy in the target and detector materials they pass through before being detected. While this energy loss is small for high momentum protons, it becomes significant at lower momenta and can be up to 50 MeV.

The best way to study the proton energy loss is using real data and looking at some reaction, where the proton is the missing particle such as $H(e, e')p$ or ${}^3\text{He}(e, e'pn)p$. In these reactions the proton energy could be reconstructed using final state particles, and a comparison with the detected proton energy can be used to obtain the momentum correction function. However, there was no H-target in the E2a experiment, and the statistics for ${}^3\text{He}(e, e'pn)p$ is low.

The other method to obtain the proton energy loss correction function is by simulation. This has been done using the Geant based simulation for CLAS, GSIM. Protons with uniformly distributed momenta within the momentum range (200–1000 MeV) were generated, and passed through GSIM simulated target and detector materials with corresponding energy losses. Then the simulated data has been analyzed under the same conditions as real data (smear simulated data according to detector resolution, remove dead wire and photo-tube channels corresponding to real data etc.). The difference between the generated and reconstructed proton momenta as a function of reconstructed momentum was fitted by a polynomial and the corresponding proton energy loss correction function was obtained for the ${}^3\text{He}$ target (4th target cell).

The plot of the proton momentum ratio before and after energy loss corrections is shown in Fig. 19.

2.2 GeV analysis

The method for the proton energy loss study and the obtained correction function for the 2.2 GeV analysis are the same as at 4.4 GeV.

The plot that shows the effect of the energy loss corrections on the proton momentum is shown in Fig. 20.

2.7 Electron fiducial cuts

4.4 GeV analysis

Signals from different detectors are used for electron identification. Though the efficiencies of these detectors are close to 100% around the middle of the sector, they might vary in some regions causing some

Sector	u	v	w
1	> 60 cm	< 360 cm	< 400 cm
2	> 55 cm	< 360 cm	< 400 cm
3	> 50 cm	< 363 cm	< 400 cm
4	> 52 cm	< 365 cm	< 396 cm
5	> 60 cm	< 360 cm	< 398 cm
6	> 50 cm	< 362 cm	< 398 cm

Table 2: The table of cut values on the u , v , w EC local coordinates of an electron for different sectors of CLAS, used to select fiducial region used for the 2.2 GeV analysis.

systematic uncertainties in the physics analysis. This variations are due to the complicated structures of the detectors.

In order to select regions with uniform detector efficiencies (constant in ϕ) a set of fiducial cuts were developed, which are different for different type of particles and magnetic field settings.

The fiducial cuts used in the current 4.4 GeV analysis are based on the CLAS approved analysis note [3] and are described in details in [8].

The u , v , w cut regions for the 2 GeV analysis were chosen individually for each sector, to eliminate the parts where the rising trends toward the edges end. As a result two or three strips were cut off. The u , v , w cuts for different sectors are listed in Table 2. The plots for the u , v , w distributions with corresponding cuts for sector 1 are shown in Fig. 21.

The electron θ vs ϕ angular distributions corresponding to different CLAS sectors were studied in different 100 MeV momentum bins. Then the corresponding distributions were sliced in different θ bins, and the ϕ distributions for a given θ angle were fit with a trapezoidal function to determine the region, where the acceptance is uniform. The two ends of the flat region were parametrized as a function of momentum and scattering angle of the electron, to be later used to select electrons inside the plateau region.

There was a need to also eliminate regions of malfunctioning TOF counters. As a result the entire θ range corresponding to bad TOF scintillator was cut. Again the θ vs ϕ distribution of the electron detected in different sectors of CLAS was studied in different momentum bins and the lower and upper positions of the θ gaps were fit as a function of momentum.

The electron θ vs ϕ distributions before and after fiducial cuts are shown for sector 1 for two electron momentum bins in Fig. 22.

2.2 GeV analysis

The methods used to obtain the electron fiducial cuts for the 2.2 GeV analysis are similar to the ones used in the 4.4 GeV analysis and are again based on the CLAS approved analysis note [3]. The u , v , w cuts for different sectors are the same as the ones listed in Table 2. The plots of the u , v , w distributions with corresponding cuts for sector 5 are shown in Fig. 23.

The procedure of obtaining the fiducial cuts for 2.2 GeV is described in details in [9].

The plots of the electron θ vs ϕ distributions before and after fiducial cuts are shown for sector 5 and two different electron momentum bins in Fig. 24.

2.8 Proton fiducial cuts

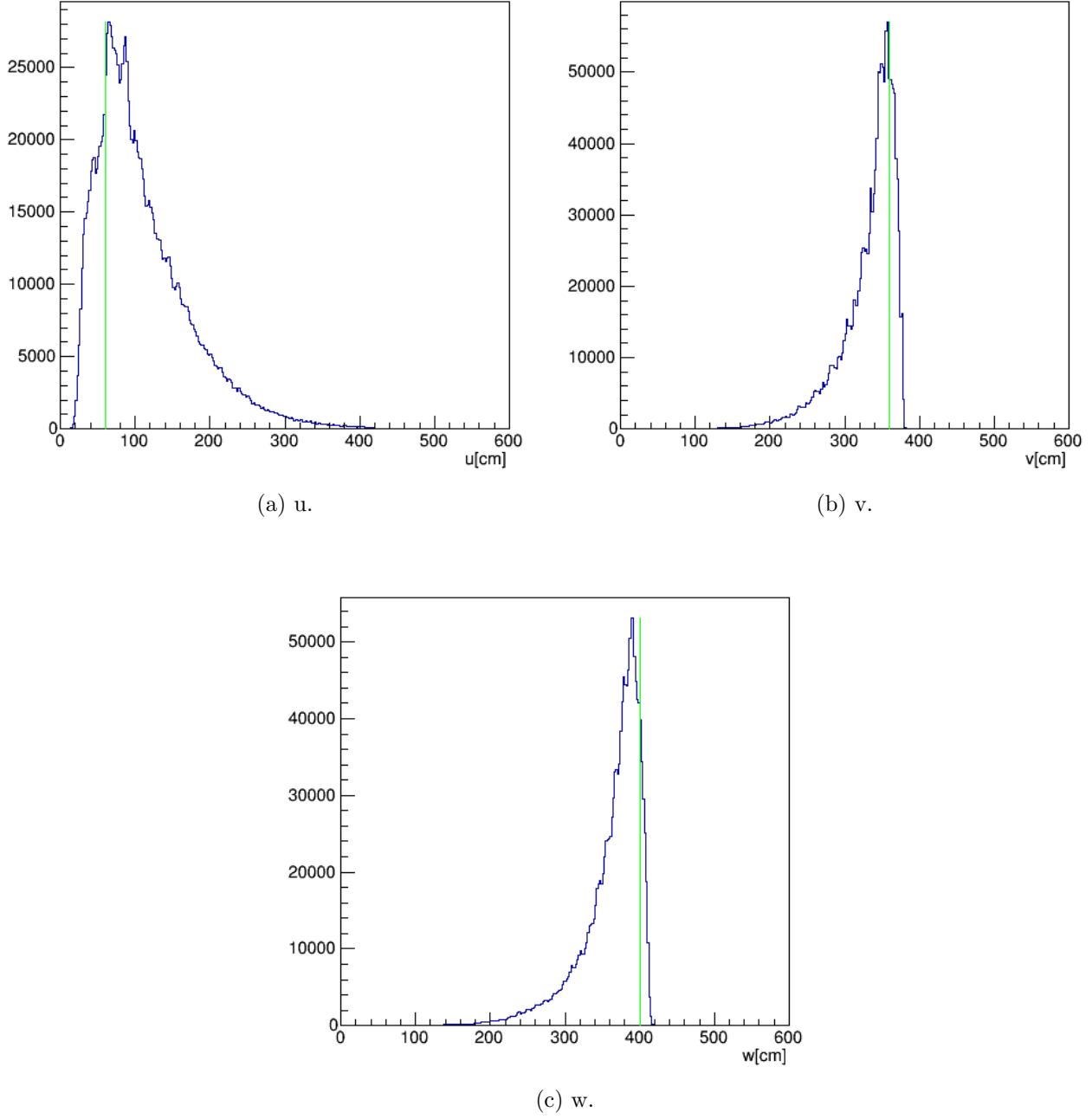


Figure 21: The distributions for the electron EC local coordinates for sector 1. The green lines show the positions of the EC edge cuts. The results are shown for the ^3He target at 4.4 GeV.

4.4 GeV analysis

The analysis procedure to obtain the fiducial cuts for the proton is similar to that of the electron. Again the θ vs ϕ angular distributions were studied in different momentum bins as well as the information on θ gaps caused by bad scintillators was stored to select regions with flat efficiencies. The proton fiducial cuts for the 4.4 GeV analysis are in the CLAS approved analysis note [3], and are described in details in [10].

The θ vs ϕ distributions of the proton before and after fiducial cuts are shown for sector 1 and mo-

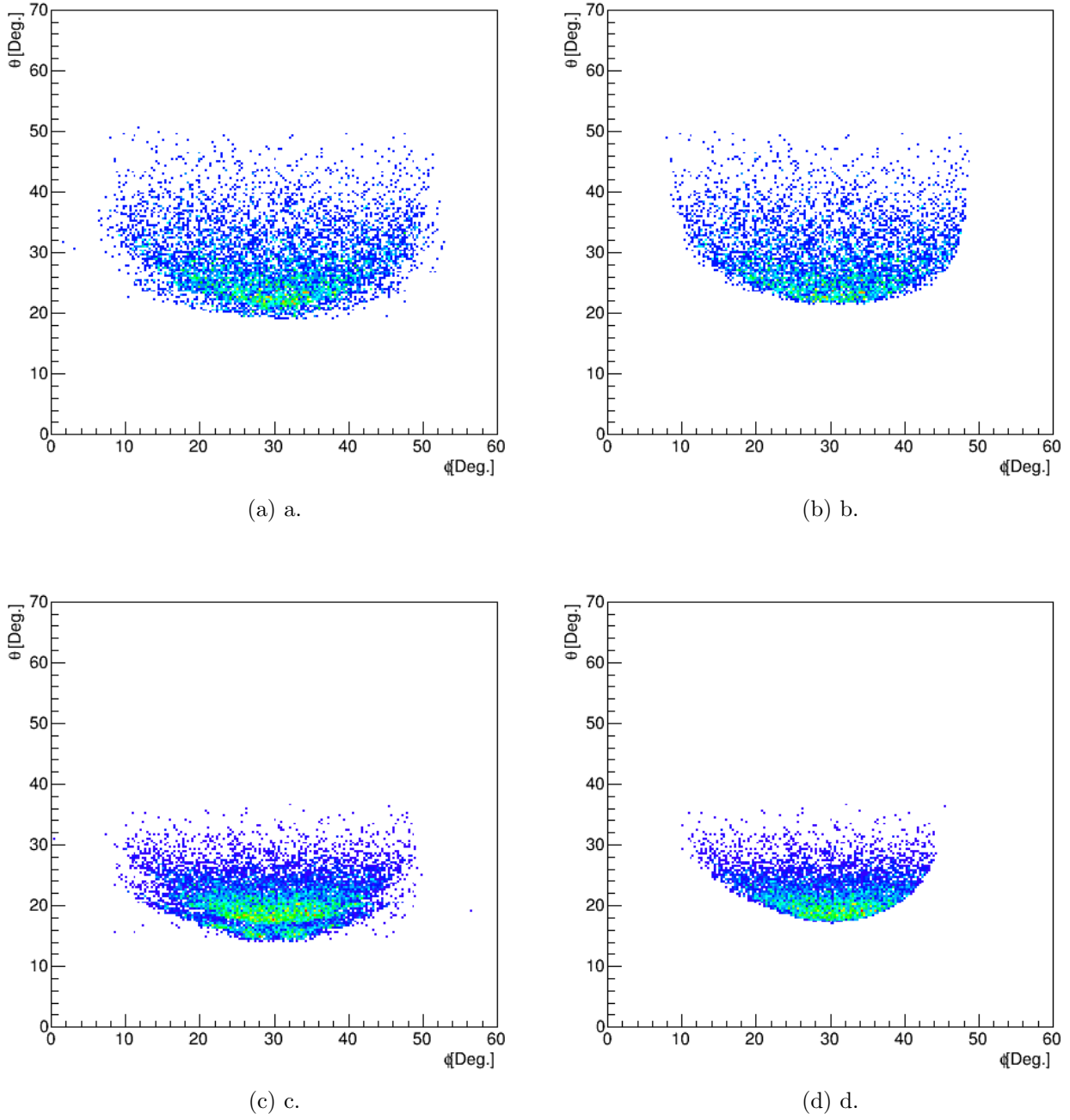


Figure 22: The θ vs ϕ distributions for electron for two momentum bins in sector 1, before and after fiducial cuts. a) and b) correspond to $p = 1.4$ GeV before and after fiducial cuts; c) and d) correspond to $p = 2.5$ GeV before and after fiducial cuts, respectively. The results are shown for the ^3He target at 4.4 GeV.

momentum $p_p = 1$ GeV in Fig. 25.

2.2 GeV analysis

The proton fiducial cuts for the 2.2 GeV analysis are similar to the one at 4.4 GeV and are the same

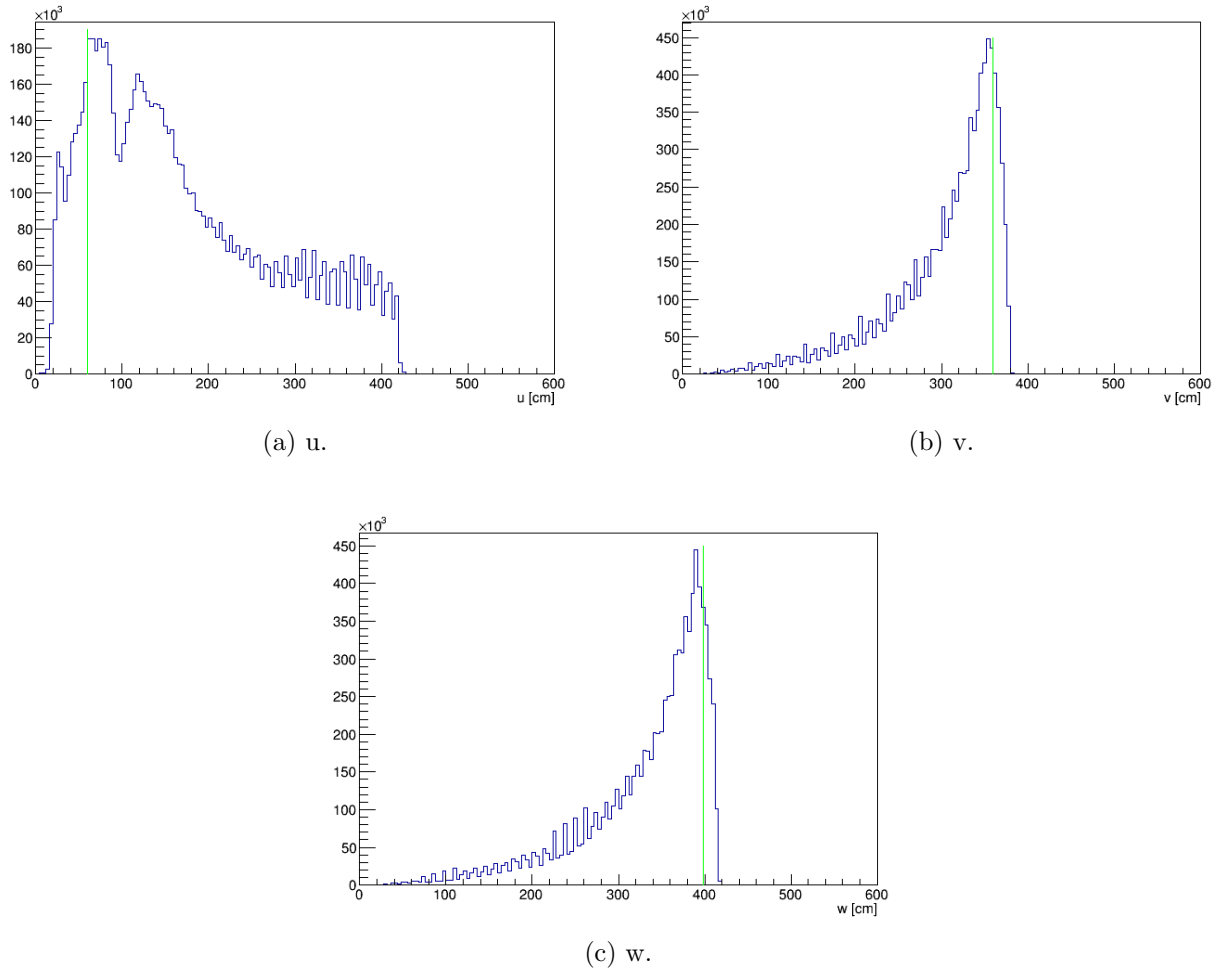


Figure 23: The distributions of the electron EC local coordinates for sector 1. The green lines show the positions of the EC edge cuts. The results are shown for the ^3He target at 2.2 GeV.

as in CLAS approved analysis note [3]. Again the detailed description on the analysis procedure and the used methods can be found in [11].

The θ vs ϕ distributions of the proton before and after fiducial cuts are shown for sector 5 and momentum $p_p = 1$ GeV in Fig. 26.

2.9 Z-vertex correction and cuts of protons and electrons

4.4 GeV analysis

There is an error in the determination of the Z-vertex position of the particles due to the vertex reconstruction technique of the CLAS tracking algorithm. We need to obtain a correct particle vertex since in our analysis we cut on the vertex to select particles originating from the same event.

The vertex correction for electrons and protons is the same for the same target.

The CLAS tracking algorithm extrapolates the track of the particles from the drift chambers to the plane that is perpendicular to the mid plane of each sector and that includes the CLAS z -axis. The point of intersection with this plane is assumed to be the particle vertex. The error comes from the fact that the

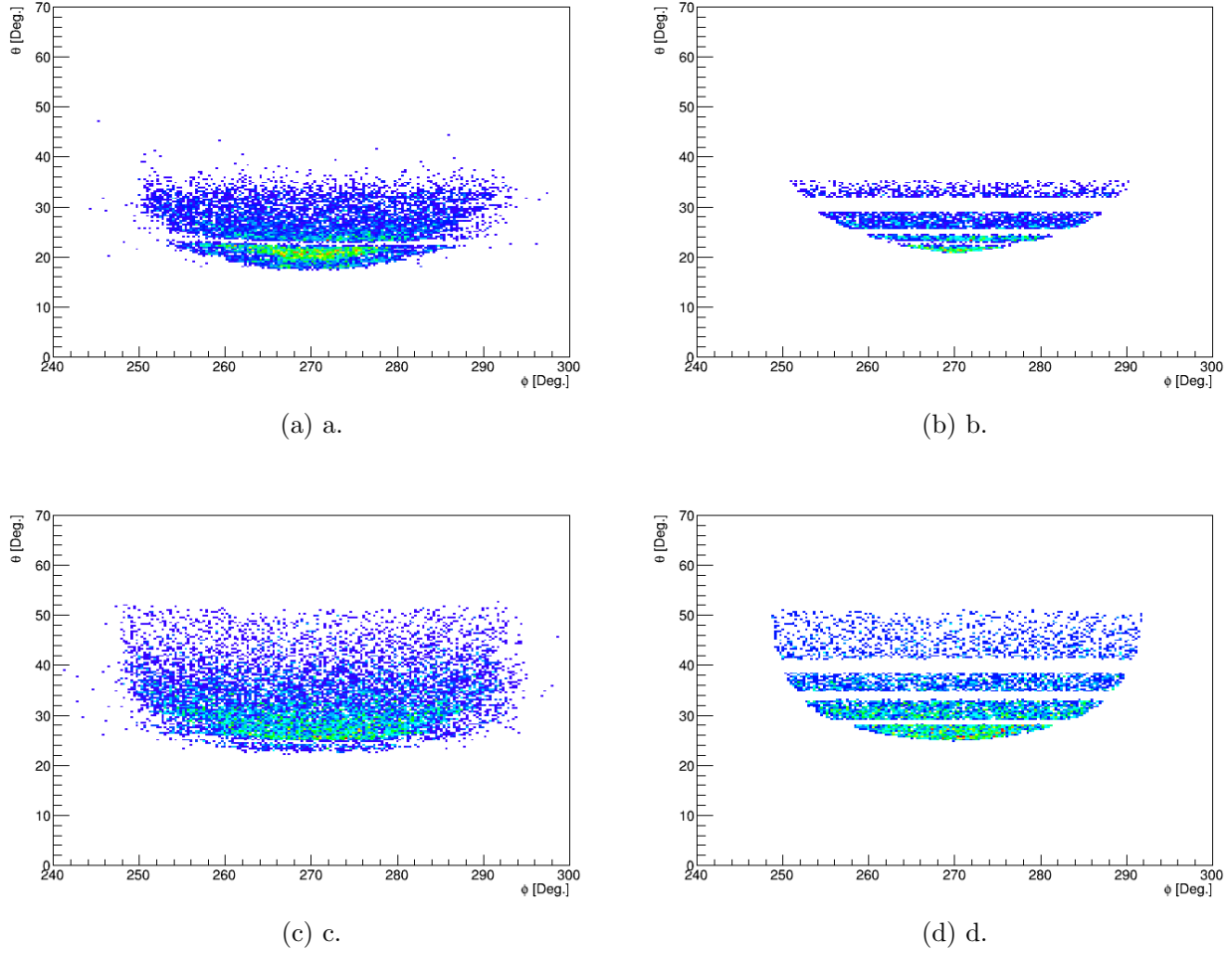


Figure 24: The θ vs ϕ distributions of the electron for two momentum bins in sector 5, before and after fiducial cuts. a) and b) correspond to $p = 1.65$ GeV before and after fiducial cuts; c) and d) correspond to $p = 1$ GeV before and after fiducial cuts, respectively. The results are shown for the ^3He target at 2.2 GeV.

beam does not always pass through the $(0, 0)$ point in the (X, Y) plane as it is assumed. If for example the beam passes through the $(x_{\text{Beam}}, y_{\text{Beam}})$ point in the (X, Y) plane, described by a angle ϕ_{Beam} and a distance $d = \sqrt{x_{\text{Beam}}^2 + y_{\text{Beam}}^2}$ which is the distance between the actual beam passing through $(x_{\text{Beam}}, y_{\text{Beam}})$ on the (X, Y) plane and the $(0, 0)$ point. The particles with $\phi = \phi_{\text{Beam}}$ will have their vertex reconstructed upstream of the actual vertex and their z vertex is equal to $z_{\text{up}} = z_{\text{true}} + \frac{d}{\tan \theta}$ where z_{true} is the true vertex of the particle. Particles with $\phi = \phi_{\text{Beam}} + \pi$ will have their vertex reconstructed downstream of the actual vertex and equal to $z_{\text{down}} = z_{\text{true}} - \frac{d}{\tan \theta}$. The ϕ dependent expression for the reconstructed vertex of the particle is the following

$$z = z_{\text{true}} + \frac{d}{\tan \theta} \times \cos(\phi - \phi_{\text{Beam}}) \quad (4)$$

The true vertex of the particle can be obtained using Eq. 4, by determining the parameters d , z_{true} and ϕ_{Beam} . To determine the parameters electrons originating from the same place in the target (target window etc., different for different targets) with the same θ scattering angle values are taking into account.

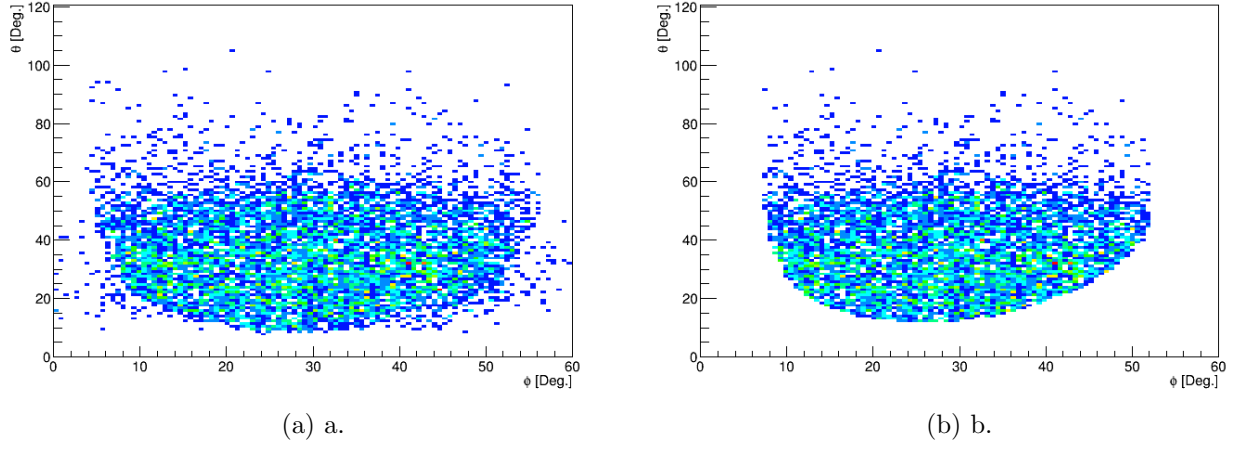


Figure 25: The θ vs ϕ distributions for the proton in sector 1, before and after fiducial cuts. a) and b) are the distributions before and after fiducial cuts for proton momentum $p = 1$ GeV, respectively. The results are shown for the ^3He target at 4.4 GeV.

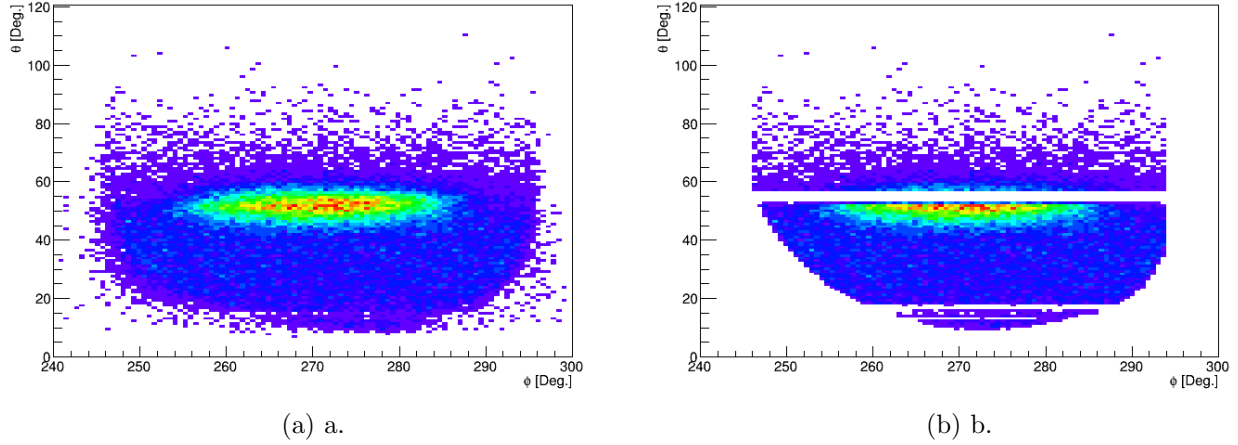


Figure 26: The θ vs ϕ distributions for the proton in sector 5, before and after fiducial cuts. a) and b) are the distributions before and after fiducial cuts for proton momentum $p = 1$ GeV, respectively. The results are shown for the ^3He target at 2.2 GeV.

For these electrons we studied the dependence of the reconstructed z vertex on the ϕ angle of the electron. The fit to this dependence has been used as a correction function for the vertex. The plot for the z vertex as a function of the ϕ angle with the corresponding fit for ^3He at 4.4 GeV is shown in Fig. 27. The ϕ angle vs the z vertex distributions before and after vertex correction are shown in Fig. 28. We can see the target region on the left, which is a cryotarget cell full of liquid ^3He , and there is small peak to the right of the target corresponding to the heat shield.

In order to select electrons coming from the target region we cut on the corrected electron vertex. The electron vertex distribution before and after the vertex correction with the corresponding cut is shown in Fig. 29.

We also cut on the difference of electron and proton vertexes to make sure that they are coming from the same event. The plot of electron and proton vertex difference with a corresponding cut is shown in

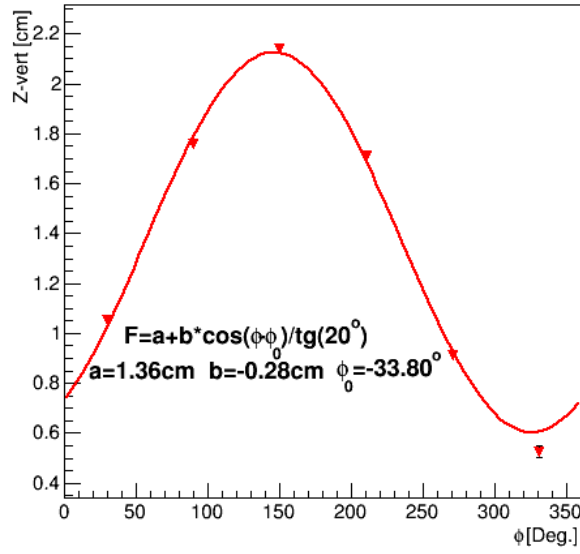
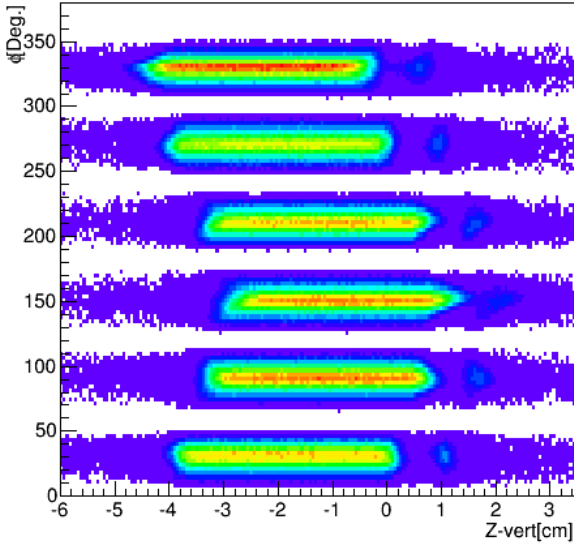
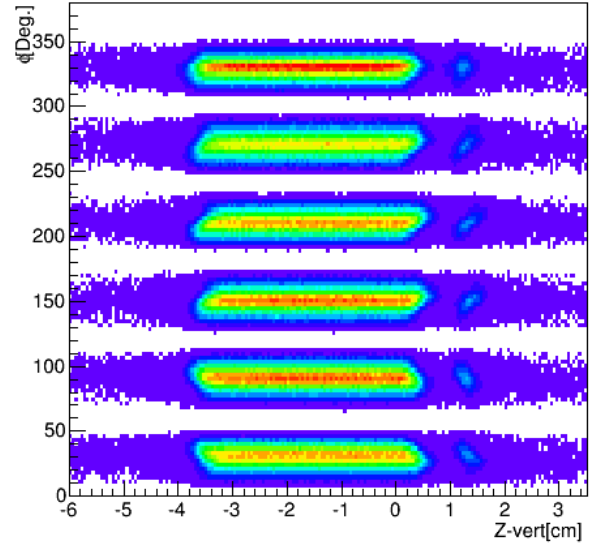


Figure 27: The plot of the z vertex as a function of the ϕ angle with the corresponding fit for the ^3He target at 4.4 GeV.



(a) Before correction.



(b) After correction.

Figure 28: The ϕ angle of the electrons plotted vs the z component of the vertex in logarithmic scale. The results are shown for the ^3He target at 4.4 GeV.

Fig. 30.

A more detailed description of the vertex correction procedure can be found in [12].

2.2 GeV analysis

The vertex corrections and cuts for the 2.2 GeV analysis have been developed in a similar way as the

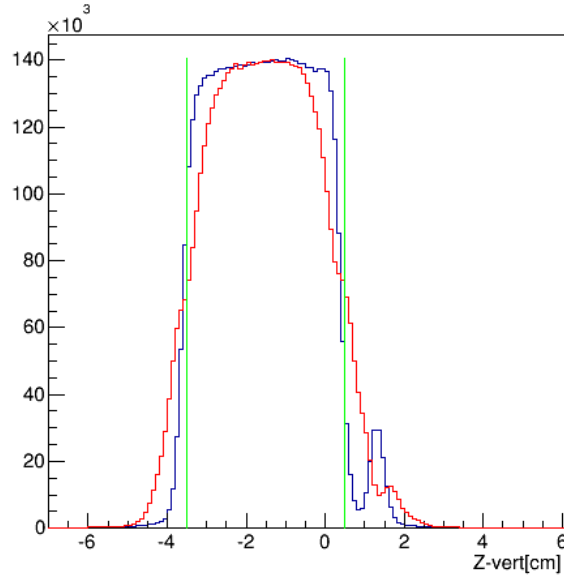


Figure 29: The distributions of the electron z vertex before (red) and after (blue) correction for ^3He at 4.4 GeV. The green lines correspond to the applied cut.

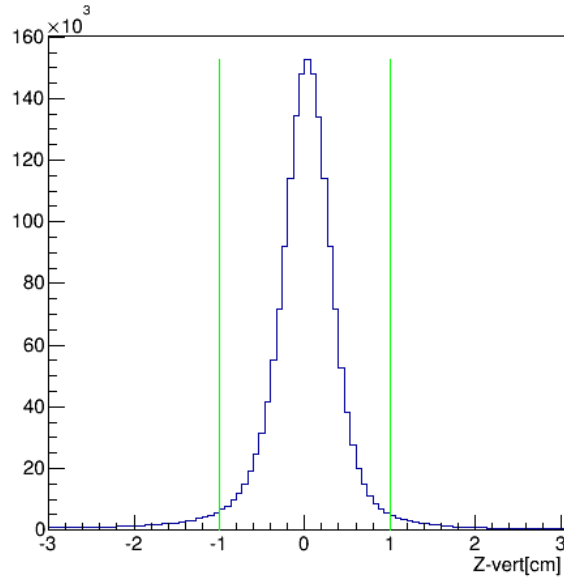


Figure 30: The electron and proton z vertex difference for ^3He at 4.4 GeV. The green lines correspond to the applied cut.

ones for 4.4 GeV. The plot of the vertex correction function for ^3He at 2.2 GeV is shown in Fig. 31.

The ϕ angle vs z vertex distributions before and after the vertex correction are shown in Fig. 32 for ^3He at 2.2 GeV.

The electron vertex distribution before and after the vertex correction with the corresponding cut is shown in Fig. 33.

The electron and proton vertex difference with a corresponding cut is shown in Fig. 34.

The vertex cuts for different targets and beam energies analysis are listed in Table. 3.

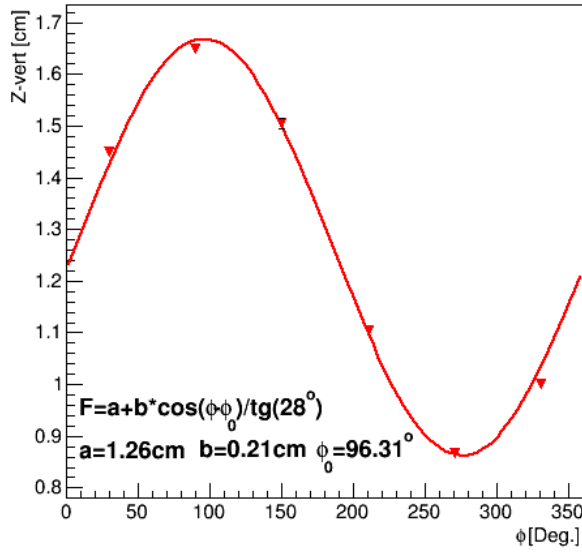
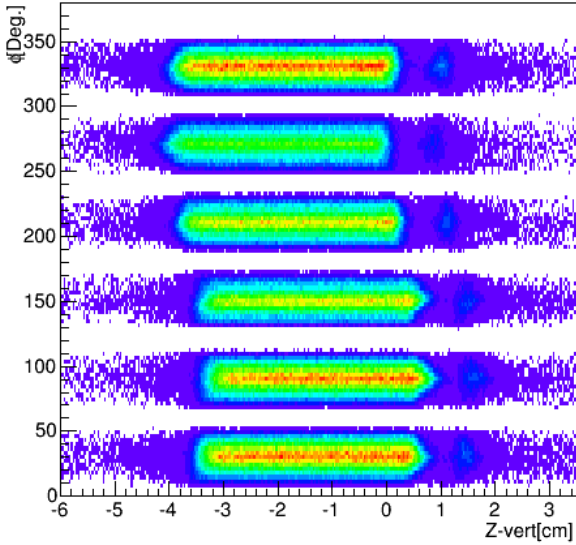
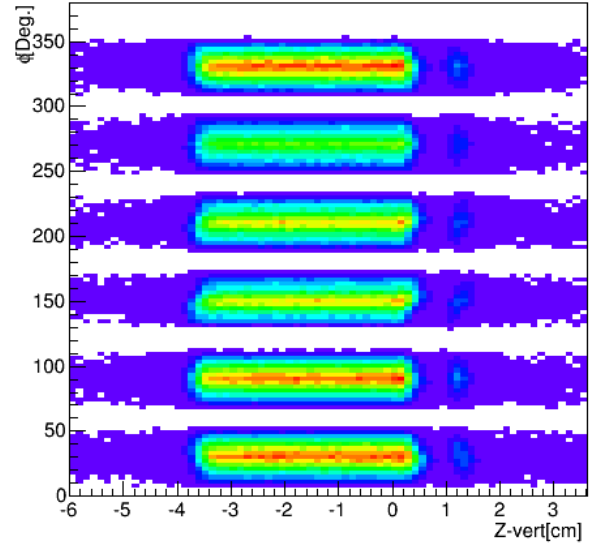


Figure 31: The plot of the z vertex as a function of the ϕ angle with corresponding fit for the ^3He target at 2.2 GeV.



(a) Before correction.



(b) After correction.

Figure 32: The ϕ angle of the electrons plotted vs the z component of the vertex. The results are shown for the ^3He target at 2.2 GeV.

The vertex cuts and corrections for other targets at both energies are described in A.1.

3 Physics analysis

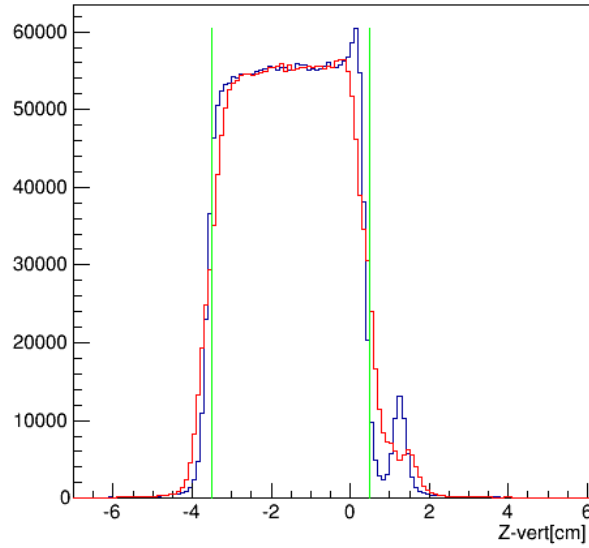


Figure 33: The distributions of the electron z vertex before (red) and after (blue) correction for ^3He at 2.2 GeV. The green lines correspond to the applied cut.

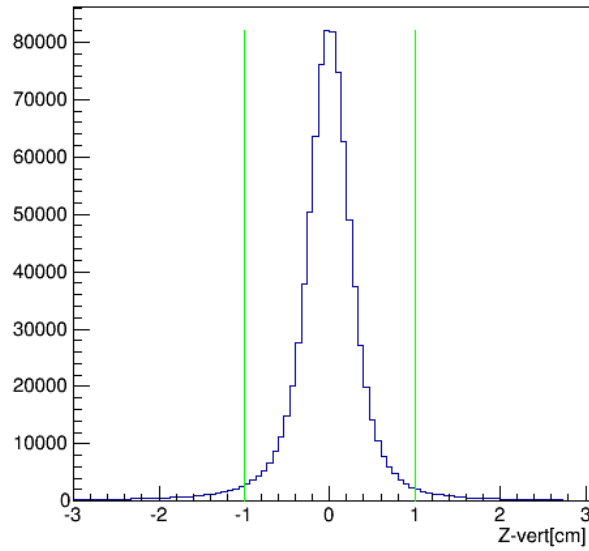


Figure 34: The electron and proton z vertex difference for ^3He at 2.2 GeV. The green lines correspond to the applied cut.

3.1 Electron and neutrino scattering from nuclei

Electron and neutrino interactions with matter have many similarities. They are similar especially in their nuclear response (FSI, Resonance production, Multinucleon effects, etc.). Electrons interact via the Electromagnetic interaction by exchanging virtual photons (interact via vector currents), and neutrinos interact via the Weak force mediated by W and Z bosons (interact via vector and axial currents). Of a particular interest to neutrino physics is the CC Weak interaction of a neutrino with a nucleon inside the nucleus and a charged lepton in the final state. The analogy of the later in electron scattering would be the

Target	2.2 GeV/c		4.4 GeV/c	
	z vertex	e^- , p z vertex diff.	z vertex	e^- , p z vertex diff.
^3He	$> -3.5 \text{ cm}, < 0.25 \text{ cm}$	$> -1 \text{ cm}, < 1 \text{ cm}$	$> -3.5 \text{ cm}, < 0.5 \text{ cm}$	$> -1 \text{ cm}, < 1 \text{ cm}$
^4He	$> -3 \text{ cm}, < 2 \text{ cm}$	$> -1 \text{ cm}, < 1 \text{ cm}$	$> -3 \text{ cm}, < 2 \text{ cm}$	$> -1 \text{ cm}, < 1 \text{ cm}$
^{12}C	$> 4.8 \text{ cm}, < 5.5 \text{ cm}$	$> -1 \text{ cm}, < 1 \text{ cm}$	$> 4.7 \text{ cm}, < 5.3 \text{ cm}$	$> -1 \text{ cm}, < 1 \text{ cm}$
^{56}Fe 1nd run group	$> 4.6 \text{ cm}, < 5.4 \text{ cm}$	$> -1 \text{ cm}, < 1 \text{ cm}$	$> 4.6 \text{ cm}, < 5.4 \text{ cm}$	$> -1 \text{ cm}, < 1 \text{ cm}$
^{56}Fe 2nd run group	$> 5.2 \text{ cm}, < 6 \text{ cm}$	$> -1 \text{ cm}, < 1 \text{ cm}$		

Table 3: The cut values on the electron z vertex, and the difference between the vertexes of the electron and the proton for different targets and beam energies. These cut values are used to select particles that are coming from the target region and correspond to the same event.

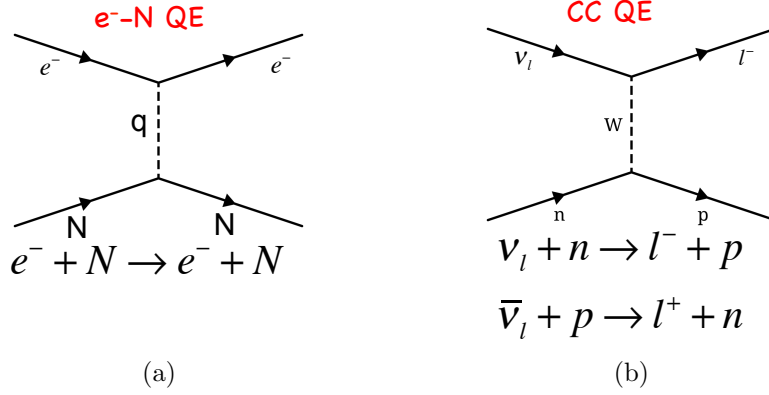


Figure 35: The diagrams of (a) quasi-elastic scattering of an electron on a nucleon and (b) CC QE scattering of a neutrino on a nucleon.

quasi-elastic scattering of an electron on a nucleon inside the nucleus, where the final state consists of the scattered electron and the knockout nucleon (see Fig. 35). The current of the electromagnetic interaction is given by Eq. 5, and the current for the CC Weak interaction is given by Eq. 6.

There are also few competing reaction mechanisms of electron scattering from nuclei that lead to same final states as QE scattering (see Fig. 36). These include (1) excitation of the nucleon into an intermediate Δ resonant state (Isobar Configuration (IC)), which is followed by de-excitation and pion emission that is absorbed by another nucleon, (2) the virtual photon can be absorbed on an exchanged meson between two nucleons (Meson exchange currents (MEC)), (3) the electron can be scattered on a nucleon in a Short Range Correlation (SRC) pair, where the nucleon knock out is followed by the ejection of the partner in the correlation, (4) the electron knocks out a nucleon that re-scatter from other nucleons in the nucleus, so called Final State Interactions (FSI).

$$j_\mu^{\text{em}} = \bar{u}\gamma_\mu u \quad (5)$$

$$j_\mu^\pm = \bar{u} \frac{-ig_W}{2\sqrt{2}} (\gamma^\mu - \gamma^\mu \gamma^5) u \quad (6)$$

where u and \bar{u} are Dirac spinors, γ^μ are Dirac matrices, $\gamma^5 = i\gamma^0\gamma^1\gamma^2\gamma^3$ and g_W is the coupling strength.

We need to use different QE event selection algorithms to suppress the contribution of two-body interactions of electrons in the nucleus and to enhance the QE scattering spectrum.

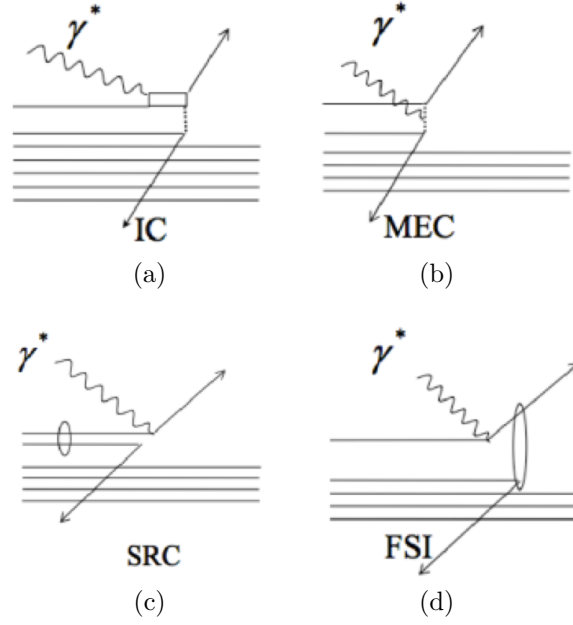


Figure 36: The diagrams of different two-body interactions of electrons in a nucleus. (a) IC: excitation of the nucleon into an intermediate Δ resonant state (Isobar Configuration (IC)), which de-excites via $\Delta N \rightarrow NN$; (b) MEC: the virtual photon is absorbed on an exchanged meson between two nucleons; (c) SRC: the electron scatters on a nucleon of a Short Range Correlation (SRC) pair followed by the ejection of the correlated partner; (d) FSI: electron knocks out a nucleon which re-scatters from other nucleons in the nucleus.

The dependence of the cross section on the kinematics of the scattering is different for neutrinos than electrons. In both cases the propagator goes like $\frac{1}{Q^2 + M^2}$, where Q^2 is the four momentum transfer and M^2 is the mass of the exchanged boson (W^\pm and Z^0 bosons for the weak interaction and 0 (photon mass) for the electromagnetic interactions). Thus, the propagator for neutrino scattering goes as $\frac{1}{M^2}$ since $m_W, m_{Z^0} \gg Q^2$. This means that the cross section goes as $\frac{1}{M^4}$ and thus is not sensitive to the kinematics.

For electron scattering the photon mass is zero and the Mott cross section will go as $\frac{1}{Q^4}$. In the analysis we divide out the Mott cross section to test the validity of the energy reconstruction techniques mentioned in Section 1 with “pseudo data” similar to neutrino data.

3.2 Analysis of CLAS6 data

Eq. 1 was applied to JLab (Thomas Jefferson Nation Accelerator Facility) Hall-B E2a experiment electron scattering data collected at 4.461 GeV and 2.261 GeV beam energies with ^3He , ^4He , ^{12}C and ^{56}Fe targets. The beam energy reconstructed with this method (E_{rec}) was then compared to the reconstructed energy obtained by summing the energies of all the final state particles in quasi-elastic scattering of an electron from a nucleon.

E2a experiment data is perfect for this type of analysis as the beam energy is close to that of the ongoing neutrino experiments as it can be seen in Fig. 37, and the targets, especially ^{12}C (NO ν A) and

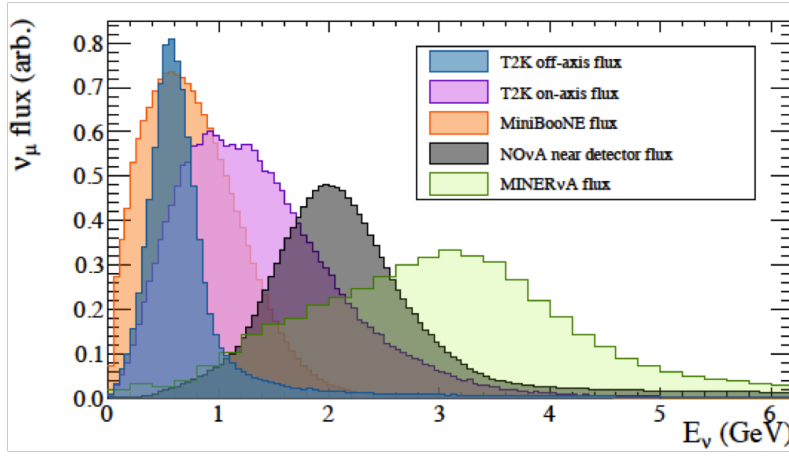


Figure 37: Current neutrino sources as a function of neutrino energy.

^{56}Fe (MINERvA) are close or identical to the ones used in these experiments.

If electron scatters quasi-elastically on a nucleon inside the nucleus that is at rest and knocks it out, the initial energy of the electron can be reconstructed using only the information of the scattered electron:

$$E_{\text{rec}} = \frac{2M\epsilon - m_e^2 + 2ME_e}{2(M - E_e + |k_e| \cos \theta)}, \quad (7)$$

where M is the nucleon mass, ϵ is the single-nucleon separation energy, m_e is the mass of the outgoing electron which is neglected, k_e is its momentum, E_e is its energy and θ is the angle between the outgoing electron and the direction of the electron beam. This is the method used in neutrino experiments with water Cherenkov-detectors, which are sensitive only to the outgoing lepton.

Suppose now an electron scatters quasi-elastically on a nucleon inside the nucleus and knocks it out and no other reaction mechanisms take place. If we detect both the scattered electron and the knocked out nucleon and assume that the target nucleus is at rest and the residual A-1 nucleus stays intact (in the Impulse Approximation (IA)), we will get the following relation from the energy conservation :

$$E_{\text{tot}} + M_A = E_e + E_p + E_{A-1} \quad (8)$$

where E_{tot} is the initial energy of the electron, M_A is the mass of the nucleus A, E_e is the energy of the electron after scattering, E_p is the energy of the nucleon after knock out and $E_{A-1} = \sqrt{M_{A-1}^2 + p_{A-1}^2}$ is the energy of the A-1 system, with M_{A-1} being its mass and p_{A-1} being its momentum which should be equal to the initial momentum of the knockout nucleon ($\vec{p}_{\text{init}} = -\vec{p}_{A-1}$). If we ignore the momentum of the recoil system which should be about the Fermi momentum for the knockout of a mean field nucleon and assume $E_{A-1} = M_{A-1}$ the relation from above can be modified to:

$$E_{\text{tot}} = E_e + T_p + \epsilon \quad (9)$$

where T_p is the kinetic energy of the knockout proton and ϵ is the binding energy per nucleon. Eq. 9 can be used to obtain the initial energy of the electron (E_{tot}) via the energy sum method. This is the method used in calorimetric-type detectors, such as the ones in the experiments NOvA, MINERvA and MicroBooNE.

The momentum conservation in the above mentioned reaction reads:

$$\vec{p} = \vec{p}_e + \vec{p}_p + \vec{p}_{A-1} \quad (10)$$

and can be used for the QE event selection. \vec{p}_e , \vec{p}_p and \vec{p}_{A-1} are the three momenta of the scattered electron, the knockout proton and the residual nucleus, respectively. If we now project the Eq. 10 on the directions parallel (denoted by z) and perpendicular (denoted by \perp) to the incoming beam we will have:

$$E_{\text{tot}} = p_e^z + p_p^z \quad (11)$$

$$p_{\text{perp}} = p_e^\perp + p_p^\perp = p_{\text{init}}^\perp \quad (12)$$

here we have neglected the electron mass and have used the fact that $\vec{p}_{A-1} = -\vec{p}_{\text{init}}$. In the IA the parallel component of the momentum of A-1 system should be small due to a knockout of mean field nucleon, and can be neglected in Eq. 11. The perpendicular component should also be small and be less or about the Fermi momentum. This means that Eq. 11 can also be used to obtain the initial energy of the scattered electron from the detected final state particles. This avoids uncertainties coming from the determination of the binding energy in Eq. 9. However, Eq. 11 provides a less accurate description of the beam energy because of the Fermi momentum of the nucleons.

Furthermore, Eq. 12 can be used to select QE events, by calculating p_{perp} and requiring that it was small p_{Fermi} .

We have applied the CLAS E2a standard cuts and corrections described in details in the previous sections and we have obtained $A(e, e')$ and $A(e, e'p)$ data samples for different targets and beam energies listed above. For QE scattering we selected events without detected charged pions and photons detected in the LAC (Large Angle Calorimeter), assuming that π^0 decays into two photons before getting detected. We also weighted each of the events with $1/\sigma_{\text{Mott}}$ to get rid of the dependence of the electron scattering cross section on kinematics and to be able to compare with neutrino data.

Target	2.2 GeV(e, e')	2.2 GeV($e, e'p$)	4.4 GeV(e, e')	4.4 GeV($e, e'p$)
^3He	$29 * 10^6$	$11.5 * 10^6$	$4 * 10^6$	$1.4 * 10^6$
^4He	$46.3 * 10^6$	$16.7 * 10^6$	$7.8 * 10^6$	$2.6 * 10^6$
^{12}C	$29 * 10^6$	$10.7 * 10^6$	$4.7 * 10^6$	$1.5 * 10^6$
^{56}Fe	$1.5 * 10^6$	$0.5 * 10^6$	$0.4 * 10^6$	$0.12 * 10^6$

Table 4: The number of good (e, e') and ($e, e'p$) events for different targets that satisfy e and p PID, vertex, fiducial and $W < 2$ GeV invariant mass cuts for the 2.2 GeV and 4.4 GeV analysis. The invariant mass cut is applied to eliminate deep inelastic scattering events.

The numbers of good (e, e') and ($e, e'p$) events for different targets that satisfy e and p PID, vertex, fiducial and $W < 2$ GeV invariant mass cuts for the 2.2 GeV and 4.4 GeV analysis are listed in Table 4. We cut on the invariant mass $W = \sqrt{(m_p + \nu)^2 - \vec{q}^2} < 2$ GeV, where m_p is the proton mass, ν is the energy transfer and \vec{q} is the three momentum transfer, to eliminate deep inelastic scattering events.

4.4 GeV $A(e, e')$ and $A(e, e'p)$ analysis

In CLAS the electron detection area is limited to a θ angle coverage ranging from 0 to 45 Deg.. The θ vs ϕ angular distribution of electrons is shown in top left of Fig. 38.

The CLAS angular coverage for charged pions is larger, however it is slightly different for negative pions compared to positively charged pions, since negative particles are being bend towards the beam line and they have a smaller θ passing through the center of the detector undetected. That is why the minimum θ detection limit for negative pions is larger than that for positive pions as it can be seen in the bottom two plots of Fig. 38. Because of the geometrical acceptance some of the charged pions are not detected

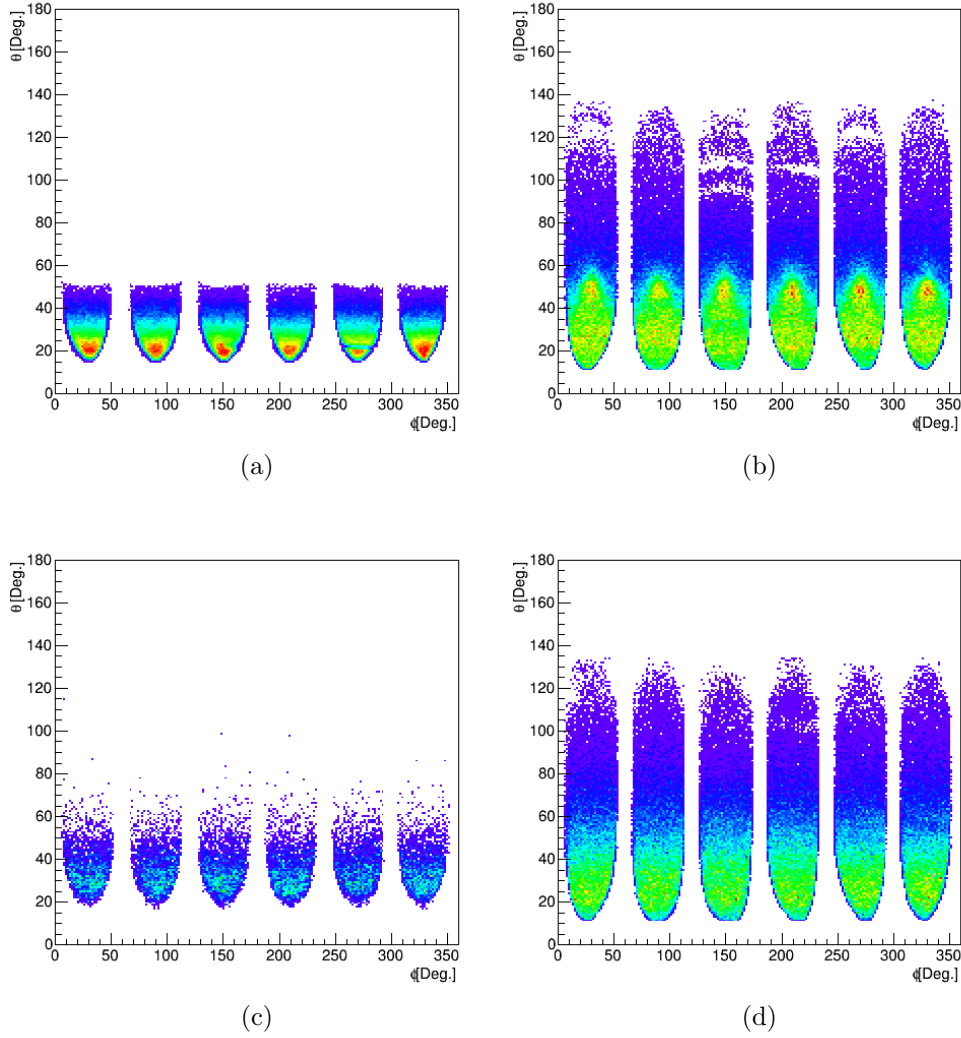


Figure 38: The θ vs ϕ angular distribution of different particles for ^3He at 4.4 GeV. (a) electrons; (b) protons; (c) π^- ; (d) π^+ .

in the CLAS detector. In our analysis we estimate the contribution of events with undetected charged pions and subtract this contribution from the event sample that has passed the no pions cut for the QE analysis. Based on the multiplicity plots for charged pions in Fig. 39, one can see that the zero or single π^\pm events dominate the event sample. Therefore, we ignore the contributions of two charged pion events to one detected charged pion events and higher number of π s.

To reject events with π^0 s for the QE event selection we require that there were no detected photons in the EC or LAC (with a θ angle coverage ranging from 45 to 75 Deg.) in the event. Because the EC has a limited detection area, and the LAC covers only two sectors of CLAS one might think that there is a need to subtract for events with undetected photons. However, the probability to detect at least one of the photons resulting from the π^0 decay is large, so we did not correct for undetected π^0 s.

The angular distribution for protons is similar to positive pions as it can be seen in top right of Fig. 38. When plotting $A(e, e'p)$ events with one detected proton, we have to estimate the contribution of events with two protons, where one of the protons has not been detected due to the geometrical acceptance of the protons and subtract for that. The proton multiplicity plots in Fig. 40 suggests that we can ignore

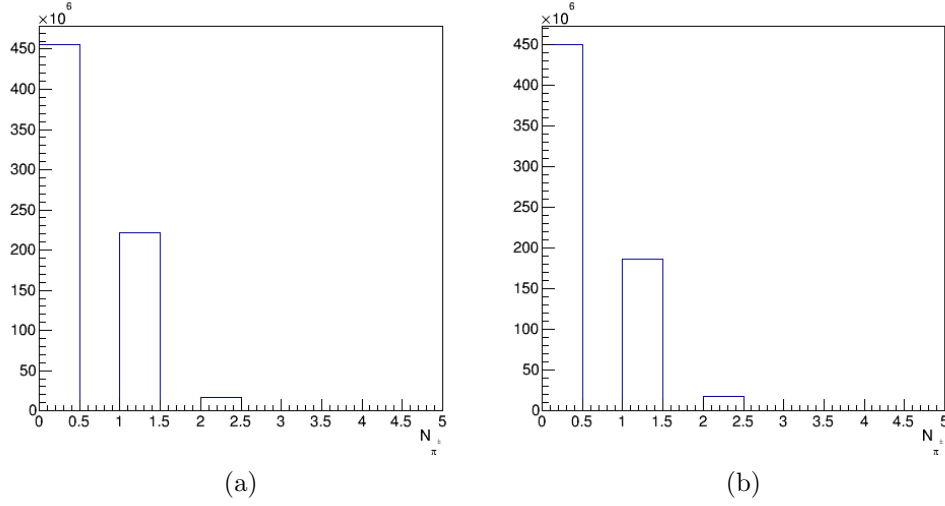


Figure 39: Multiplicity distributions of π^\pm for ^3He and ^{56}Fe targets at 4.4 GeV (a) ^3He ; (b) ^{56}Fe .

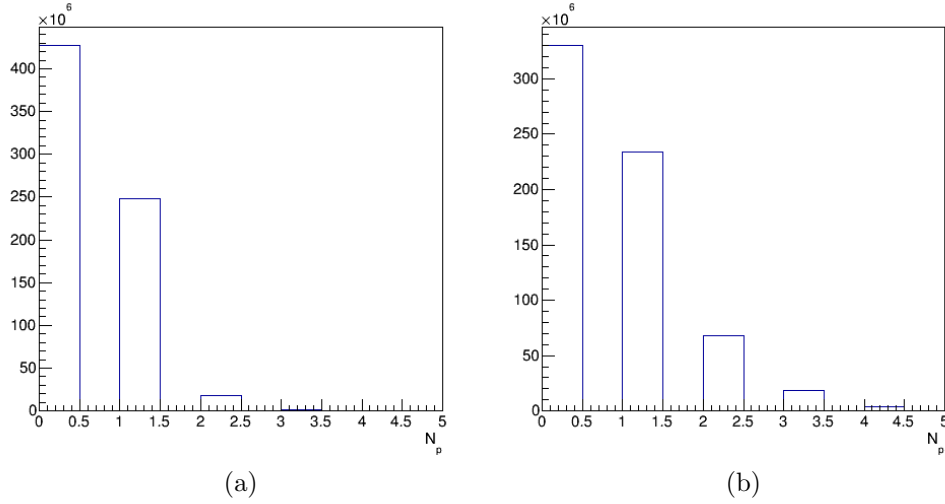


Figure 40: Multiplicity distributions of protons for ^3He and ^{56}Fe targets at 4.4 GeV (a) ^3He ; (b) ^{56}Fe .

contributions of three proton events to two detected proton events etc..

We have calculated E_{rec} of $A(e, e')$ using Eq. 7. In Fig.41 we can see E_{rec} as a function of p_{perp} given by 12. The quasi-elastic scattering events appear as a distinct peak in the distribution with small p_{perp} values and E_{rec} values close to the beam energy. The pion rejection cut reduces the non-QE background corresponding to higher values of p_\perp . We can see that most of the QE events are at $p_\perp < 200$ GeV as was expected for QE knock-out of mean field nucleon.

The E_{rec} distributions with no cuts, with pion rejection cuts and with pion rejection and $p_{\text{perp}} < 200$ GeV cuts are compared in Fig.42. As we apply the above mentioned cuts we see that the quasi-elastic scattering peak becomes more and more evident and is centered at the beam energy. This means that the reconstruction formula works. However, further analysis is required in order to understand what are the physics processes describing the events in the tail of the distribution to the left of the peak. It is evident that for heavier targets a smaller fraction of events is being reconstructed within the beam energy compared to light nuclei.

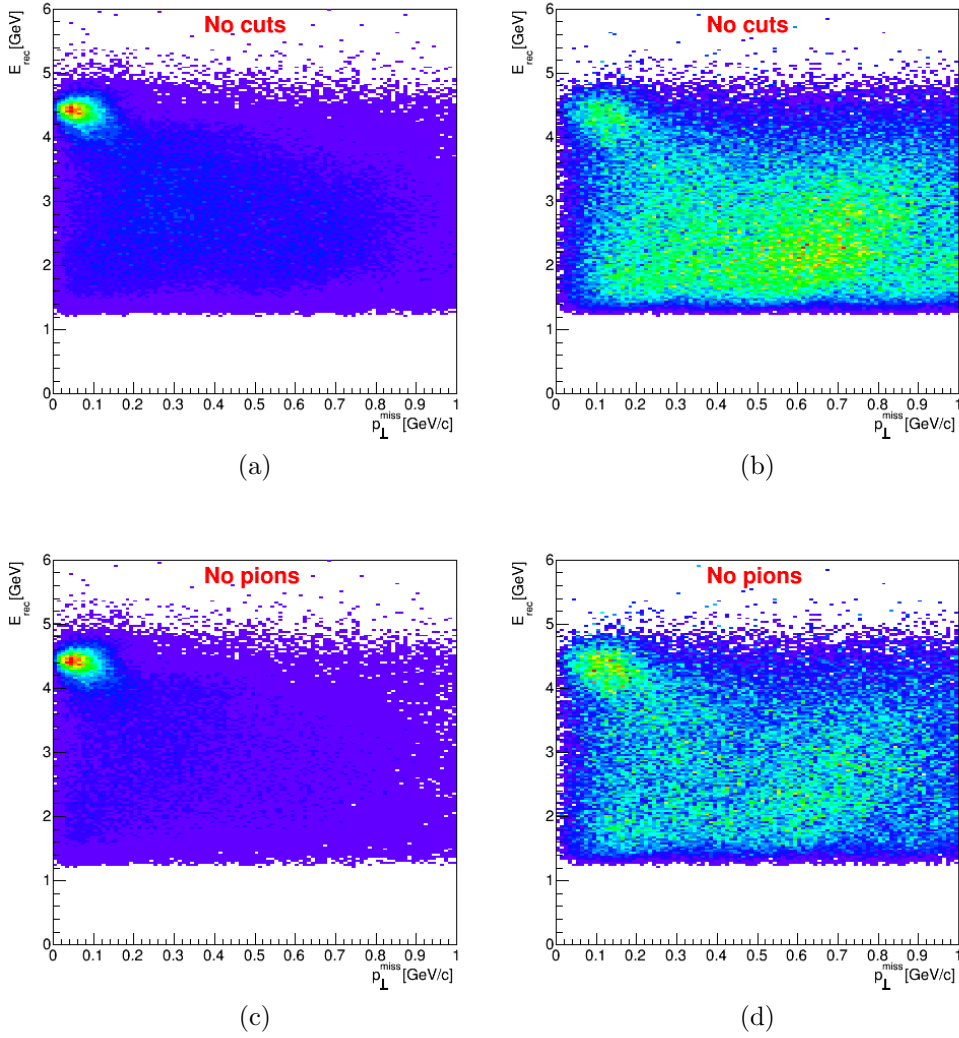


Figure 41: Reconstructed energy E_{rec} obtained using Eq. 7 as a function of the total perpendicular momentum of the scattered electron and the knockout nucleon system for ^3He and ^{56}Fe targets at 4.4 GeV before (top plots) and after (bottom plots) pion rejection cuts. (a),(c) ^3He ; (b),(d) ^{56}Fe .

To subtract the contribution of undetected charged pion events and to obtain a true no pion spectrum in the $A(e, e')$ ($A(e, e'p)$) analysis, for each $A(e, e'\pi^\pm)$ ($A(e, e'p\pi^\pm)$) one detected pion event we rotate the π^\pm (the proton and π^\pm) around the direction of the three momentum transfer \vec{q} for multiple times, and find the probability of the π^\pm being out of the acceptance region and not being detected. This is later used to estimated the corresponding number of undetected π^\pm events that contribute to $A(e, e')$ ($A(e, e'p)$) events, for each $A(e, e'\pi^\pm)$ ($A(e, e'p\pi^\pm)$) event with one detected π^\pm . We chose to rotate around the \vec{q} , as this shouldn't affect the cross section of the reaction.

The subtraction for undetected pions in $A(e, e')$ analysis is done the following way: For each event that has an electron and one detected charged pion, we rotate the pion around the direction of the three momentum transfer \vec{q} for $N_{\text{tot}} = 100$ times by a randomly generated angle phi (see Fig. 43) within 0 to 2π rad, and determined the total number of successes N_{det} , where the rotated pion is inside the geometrical acceptance for the type of charged pion. If we have one event with an electron and one detected charged pion, the corresponding number of events with an electron and an undetected charged

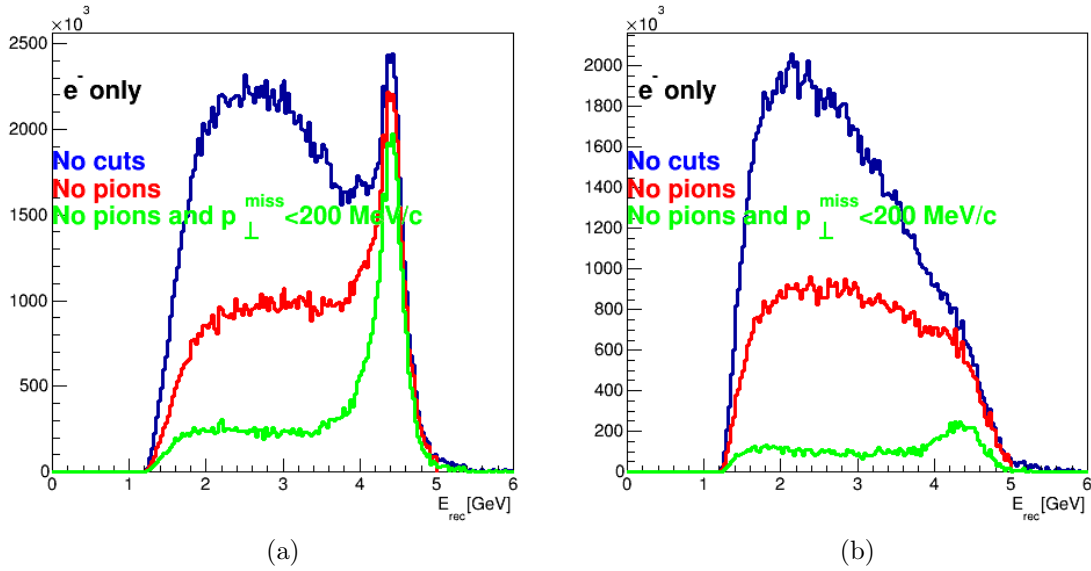


Figure 42: Reconstructed energy E_{rec} of $A(e, e')$ obtained using Eq. 7 with no cuts (blue), with pion rejection cut (red) and with cut on total perpendicular momentum of the scattered electron and the knockout nucleon system $p_{\text{perp}} < 200$ MeV/c in addition to pion rejection cut for ${}^3\text{He}$ and ${}^{56}\text{Fe}$ targets at 4.4 GeV (a) ${}^3\text{He}$; (b) ${}^{56}\text{Fe}$.

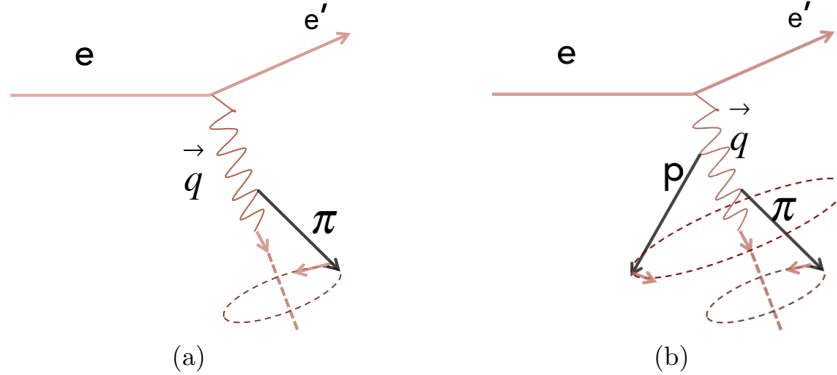


Figure 43: The diagrams for the (a) pion rotation and the (b) pion and proton rotation around the three momentum transfer (\vec{q}) for the estimation of events with undetected charged pions in $A(e, e')$ and $A(e, e'p)$ analysis.

pion will be $(N_{\text{tot}} - N_{\text{det}})/N_{\text{det}}$. This ratio is used as a correction factor for each event. The plots of E_{rec} for detected (blue) and undetected (red) 1 pion events are shown on the left side of Fig. 44. The plots on the top correspond to ${}^3\text{He}(e, e')$ and the ones on the bottom correspond to ${}^{56}\text{Fe}(e, e')$. These plots suggest that we have nearly the same amount of detected and undetected 1 pion events, which can be explained by the following rough estimation of CLAS detector geometrical acceptance for charged pions. If we assume that total θ , ϕ angular range to be covered is 360 Deg. in ϕ and 70 Deg. in θ and the CLAS detector coverage is 6×40 Deg. in ϕ and 50 Deg., where 6 represents the number of sectors, then we will obtain for geometrical acceptance of charged pions $\epsilon = (50 \times 40 \times 6)/(70 \times 360) \times 100\% \approx 48\%$.

The plots of E_{rec} for $A(e, e')$ events with no photons and charged pions, before (blue) and after (red) subtracting for undetected pions are shown in the right side of Fig. 44. We can see that the subtraction

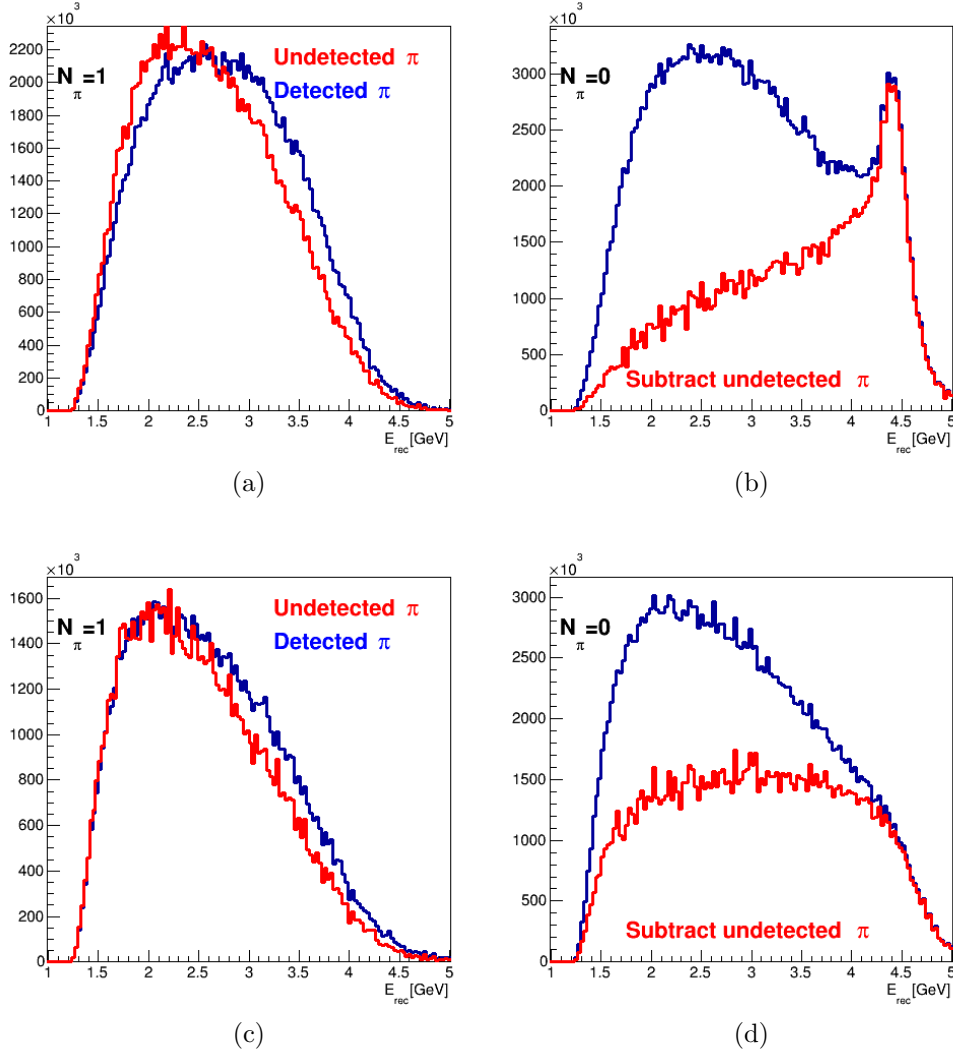


Figure 44: The E_{rec} obtained using Eq. 7, for detected (blue) and undetected (red) 1 pion events for (a) ${}^3\text{He}(e, e'\pi^\pm)$; (c) ${}^{56}\text{Fe}(e, e'\pi^\pm)$ at 4.4 GeV. Reconstructed energy E_{rec} of $\text{A}(e, e')$ no pion spectrum before (blue) and after (red) subtraction for undetected pions for (b) ${}^3\text{He}$ and (d) ${}^{56}\text{Fe}$ targets at 4.4 GeV.

reduces significantly the non-QE background. However, there are still a lot of events that correspond to reconstructed energy values off from the true beam energy and thus these events are not QE. It is also evident from plots that subtraction doesn't affect the peak but reduces the tail populated with non-QE events as we would expect.

To estimate the number of events with undetected pions in the $\text{A}(e, e'p)$ analysis, we rotate both the proton and the pion around the direction of \vec{q} for $N_{\text{tot}} = 100$ times by randomly generate angle phi within 0 to 2π rad for each event that has a detected electron, one detected proton and one detected charged pion. The number of simulated events where the rotated proton and pion were inside their acceptance regions is N_{both} , and the total number of simulated events where only the rotated proton was inside its acceptance region and the pion is undetected is N_{prot} , then the number of events with undetected pions corresponding to one event with an electron, one detected proton and one detected charged pion will be $N_{\text{prot}}/N_{\text{both}}$.

In the $\text{A}(e, e'p)$ analysis in addition to subtracting for undetected pions we also need to estimate the

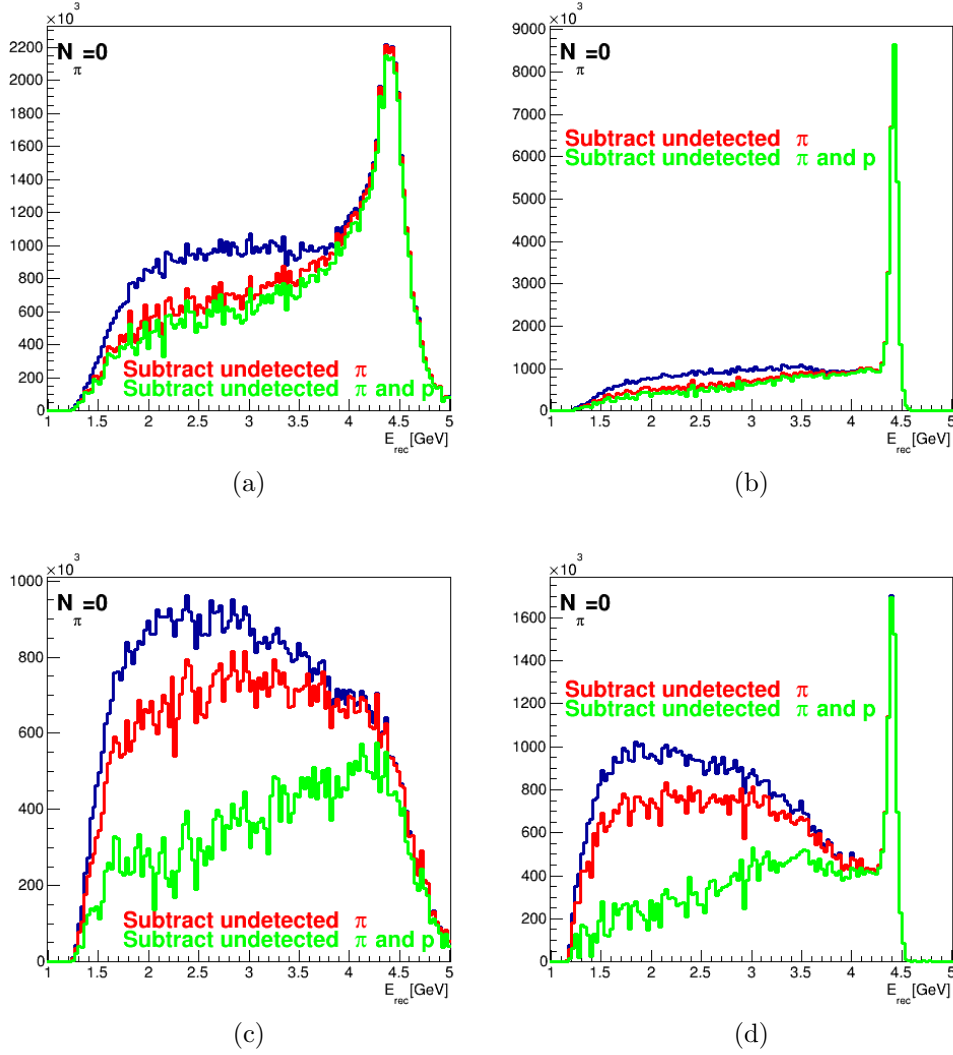


Figure 45: E_{rec} (plots on the left) and E_{tot} (plots on the right) distributions of $A(e, e'p)$ no pion spectrum before subtraction for undetected pions (blue), after subtraction for undetected pions (red) and after subtraction for undetected pions and undetected two proton events (green) for (a), (b) ${}^3\text{He}$ and (c), (d) ${}^{56}\text{Fe}$ targets at 4.4 GeV.

contribution of events with two protons, where one of the protons has not been detected and subtract it to obtain the true one electron and one detected proton spectrum.

To get rid off undetected two proton events in the $A(e, e'p)$ analysis, for each event that has a detected electron and two detected protons we again rotate each of the protons around the direction of \vec{q} for $N_{\text{tot}} = 100$ times by randomly generate an angle ϕ within 0 to 2π rad. The total number of simulated events, where only one of the protons is inside the proton geometrical acceptance is N_{prot} . If we have one event with an electron and two detected protons, the corresponding number of events where one of the protons has not been detected will be $N_{\text{prot}}/N_{\text{both}}$.

The plots of E_{rec} and E_{tot} for $A(e, e'p)$ with no pions (no photons and charged pions), before subtraction for undetected pions (blue), after subtraction for undetected pions (red) and after subtraction for undetected pions and undetected two proton events (green) for ${}^3\text{He}$ (top plots) and ${}^{56}\text{Fe}$ (bottom plots) targets are shown in Fig. 45. As we can see the subtraction has a small effect on QE peak, and mainly

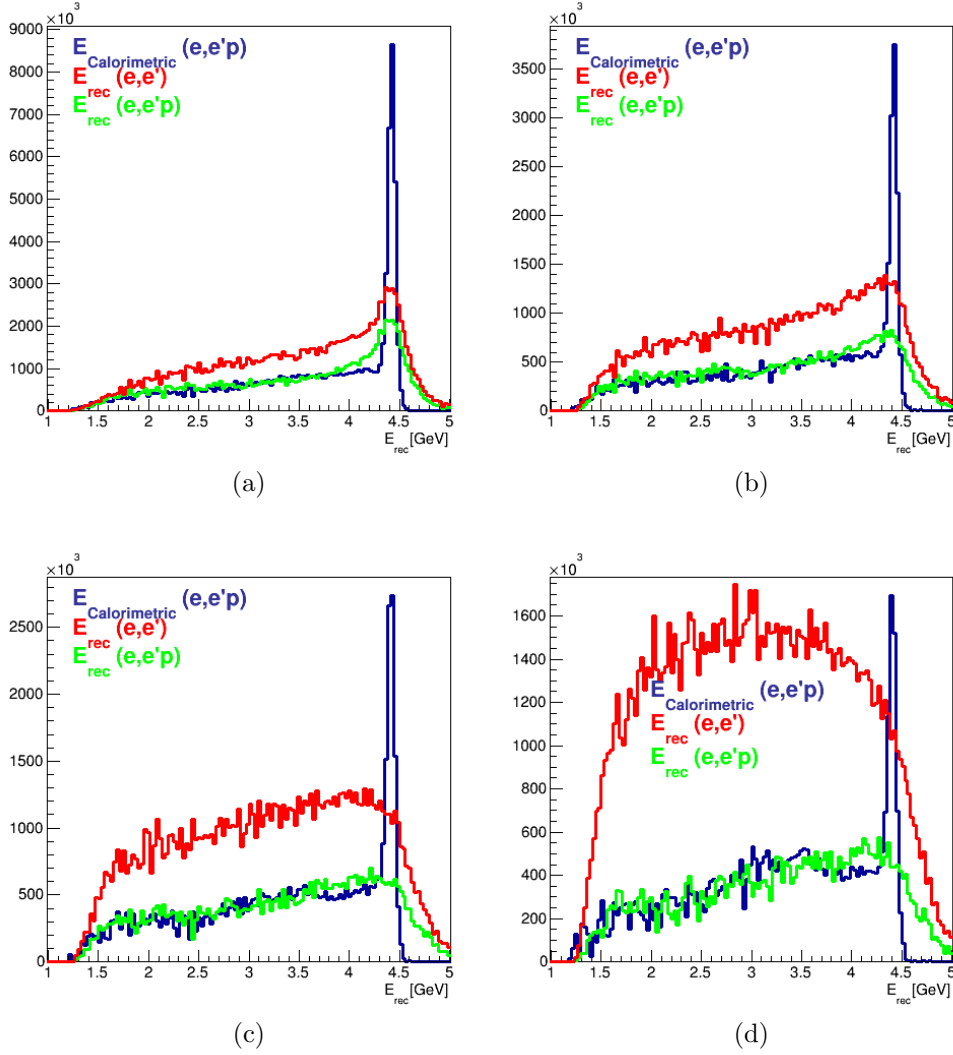


Figure 46: E_{rec} distributions of $A(e, e')$ (red) and $A(e, e'p)$ (green) no pion spectrum and E_{tot} distribution of $A(e, e'p)$ (blue) no pion spectrum after subtraction for undetected pions and undetected two proton events for (a) ${}^3\text{He}$, (b) ${}^4\text{He}$, (c) ${}^{12}\text{C}$ and (d) ${}^{56}\text{Fe}$ targets at 4.4 GeV.

reduces the non-QE tail as one would expected. The effect of the undetected pion subtraction is much larger, however even after subtraction we are left with a significant number of background events that don't describe the true beam energy.

In order to compare the results from the two energy reconstruction techniques, I have plot E_{rec} of $A(e, e')$ and $A(e, e'p)$ events and E_{tot} of $A(e, e'p)$ events (see Fig.46). It is clear that the resolution of reconstructed energy spectrum improves significantly when we use also use information about the detected proton. There is a sharp peak evident in the distribution of E_{tot} located nearly at the beam energy and populated with mainly QE events, and there is a tail populated with non-QE events extending to the left of the peak. The fact that we have neglected the kinetic energy of recoil $A - 1$ system, almost doesn't affect the E_{tot} distribution as its contribution should be about few MeV. The peak in E_{rec} is much broader and there is no clear separation between the peak and the background. The width of the peak is caused by the approximations made in the derivation of Eq. 7 (assumption that nucleon is at rest, uncertainty in the knowledge of binding energy, etc.). Also as we go to heavier nuclei the non-QE background increases.

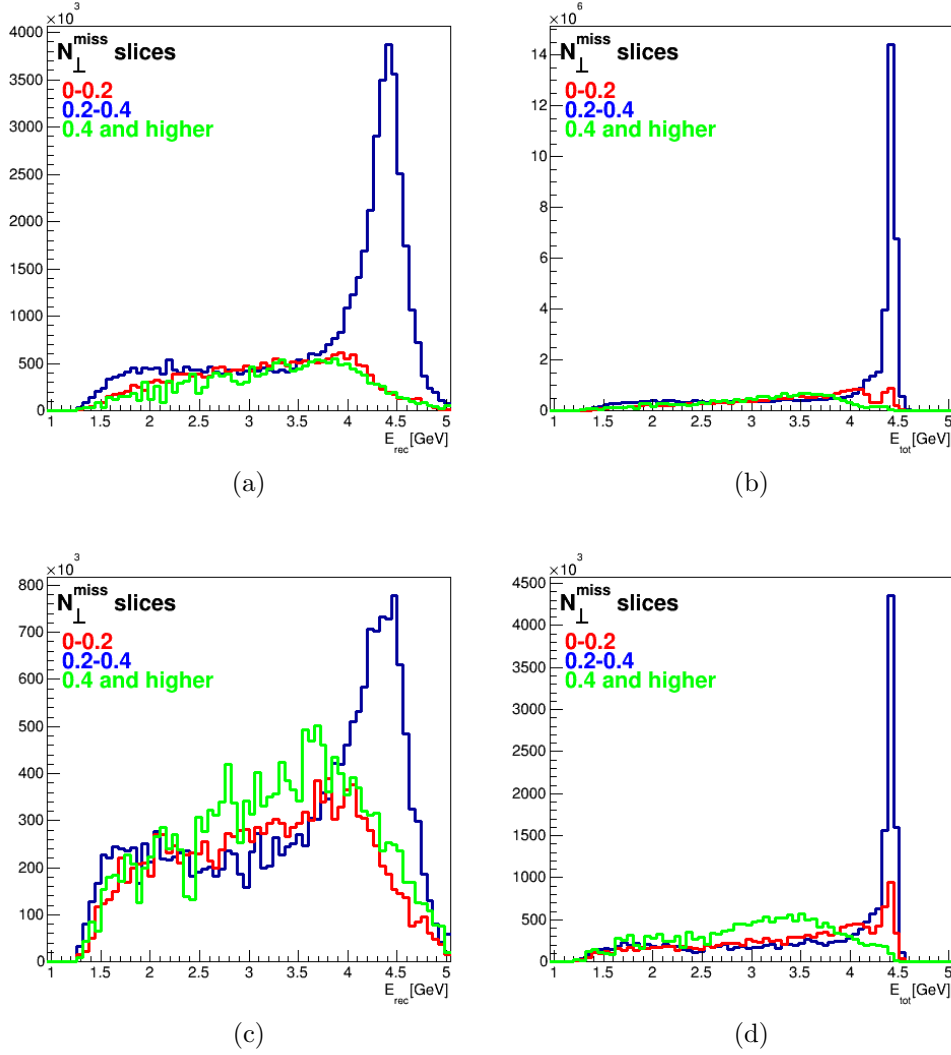


Figure 47: E_{tot} ((b) and (d)) and E_{rec} ((a) and (c)) distributions of $A(e, e'p)$ no pion spectrum after subtraction for undetected pions and undetected protons for three different regions of p_{perp} (0–200 MeV/c, 200 – 400 MeV/c and 400 MeV/c and higher) for (a), (b) ^3He and (c), (d) ^{56}Fe targets at 4.4 GeV.

We have also plot the E_{rec} and E_{tot} distributions for three different regions of p_{perp} (0 – 200 MeV/c (blue), 200 – 400 MeV/c (red) and 400 MeV/c and higher (green)) (see Fig.47). We expect the region corresponding to p_{perp} values from 0 – 200 MeV/c to be populated mainly with QE events on mean field nucleons. p_{perp} (200 – 400 MeV/c corresponds to a transition region between QE scattering of a mean filed nucleons and non-QE events, and the region corresponding to p_{perp} values of (400 MeV/c and higher) should be populated mainly with non-QE background events. We can see in the figure that as we go higher in p_{perp} the contribution of non-QE electron scattering events increases as expected. The tail to the left of the QE peak extending to lower beam energies in the distribution of E_{tot} corresponding to p_{perp} values from the range 0 – 200 MeV/c for different targets defines the highest limit for radiation tail, corresponding to the events where electron has radiated a photon either before or after QE scattering on a nucleon due to bremsstrahlung in the electromagnetic field of the nucleus, where interaction takes place (internal bremsstrahlung), or the electromagnetic field of other nuclei (external bremsstrahlung).

The QE peak in E_{rec} distribution corresponding to p_{perp} values from the range 0 – 200 MeV/c for

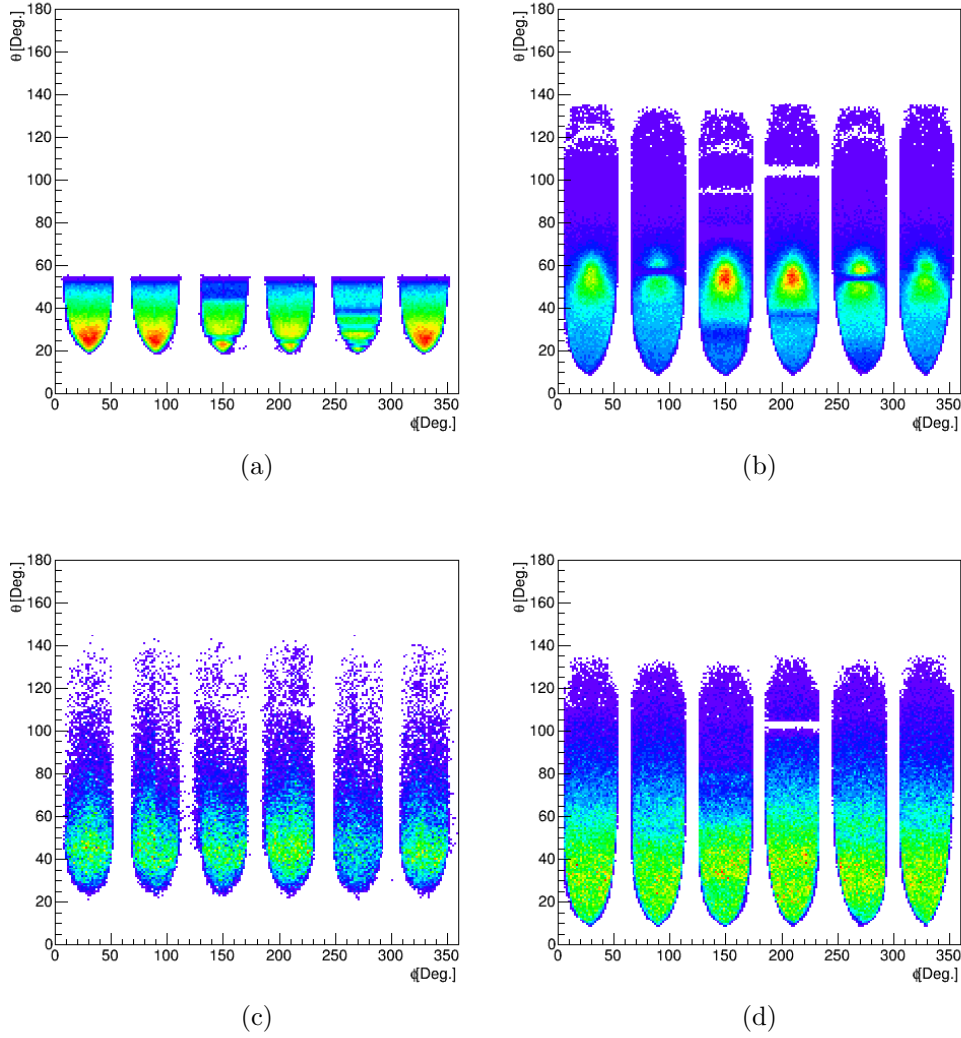


Figure 48: The θ vs ϕ angular distribution of different particles for ^3He at 2.2 GeV. (a) electrons; (b) protons; (c) π^- ; (d) π^+ .

different targets is significantly broader compared to the one in E_{tot} distribution corresponding to same p_{perp} values.

2.2 GeV $A(e, e')$ and $A(e, e'p)$ analysis

The analysis procedure at 2.2 GeV is similar to that for 4.4 GeV. We have again applied CLAS E2a standard cuts and corrections for corresponding energy described in details in the previous sections and have looked at the $A(e, e')$ and $A(e, e'p)$ data samples.

The θ vs ϕ angular distributions of different particles at 2.2 GeV are shown in Fig. 48. And the proton and charged pion multiplicity plots are shown in 50 and 49 correspondingly. We can see that as we go to heavier nuclei the ratio of 2 detected proton events to 1 detected proton events increases. This is expected as there are much more protons in heavier nuclei compared to light nuclei.

The E_{rec} distributions of $A(e, e')$ events obtained using Eq. 7 after different cuts are shown in 52. We have first followed the procedure used in neutrino experiments and have required that there were no charged pions and photons detected in the event, for QE event selection. In order to clean QE spectrum

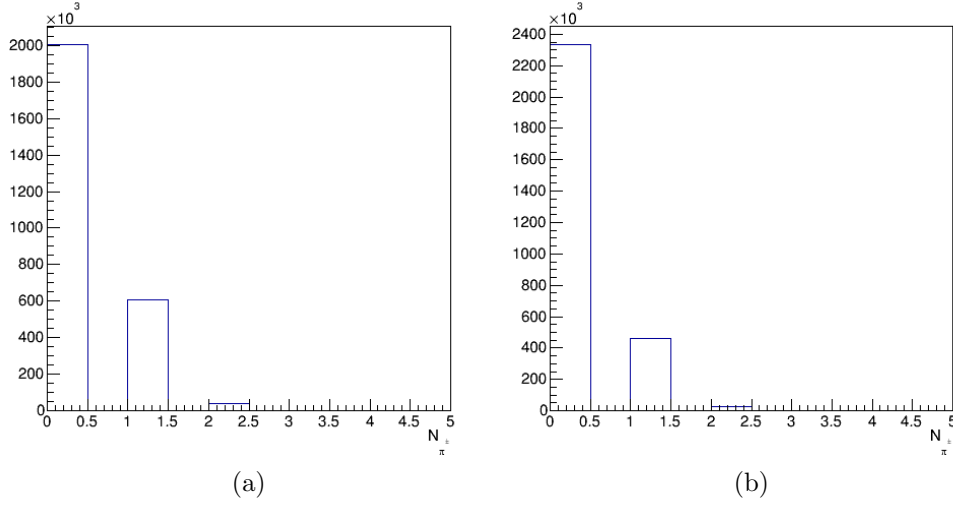


Figure 49: Multiplicity distributions of π^\pm for ^3He and ^{56}Fe targets at 2.2 GeV (a) ^3He ; (b) ^{56}Fe .

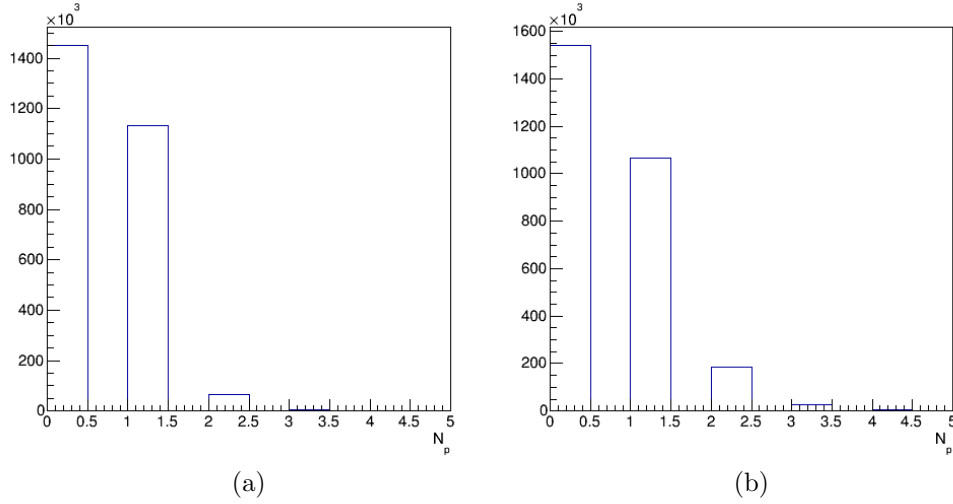


Figure 50: Multiplicity distributions of protons for ^3He and ^{56}Fe targets at 2.2 GeV (a) ^3He ; (b) ^{56}Fe .

further we have cut on $p_{\text{perp}} < 200$ MeV. This cut requires the detection of the proton in addition to the electron. We can see the plot of E_{rec} as a function of p_{perp} after these cuts in Fig.51. The plots are shown for ^3He (Fig. 51a, Fig. 51c) and ^{56}Fe (Fig. 51b, Fig. 51d) targets before (top plots) and after (bottom plots) pion rejection cuts.

We again had to subtracted for undetected charged pions in $A(e, e')$ analysis, to obtain true 0 pion spectrum. The distributions of E_{rec} for detected (blue) and undetected (red) 1 pion events for $^3\text{He}(e, e'\pi^\pm)$ are shown in Fig. 53a, and the ones for $^{56}\text{Fe}(e, e'\pi^\pm)$ in Fig. 53c. The E_{rec} distributions of 0 pion spectrum before (blue) and after (red) subtraction for undetected pions for $^3\text{He}(e, e')$ are shown in Fig. 53b and the ones for $^{56}\text{Fe}(e, e')$ are shown in Fig. 53d.

In in $A(e, e'p)$ analysis we have subtracted for both undetected 1 pion events and undetected 2 proton events. The E_{rec} (plots on the left) and E_{tot} (plots on the right) distributions of $A(e, e'p)$ no pion spectrum before subtraction for undetected pions (blue), after subtraction for undetected pions (red) and after subtraction for undetected pions and undetected two proton events (green) for ^3He (Fig. 54a, 54b) and

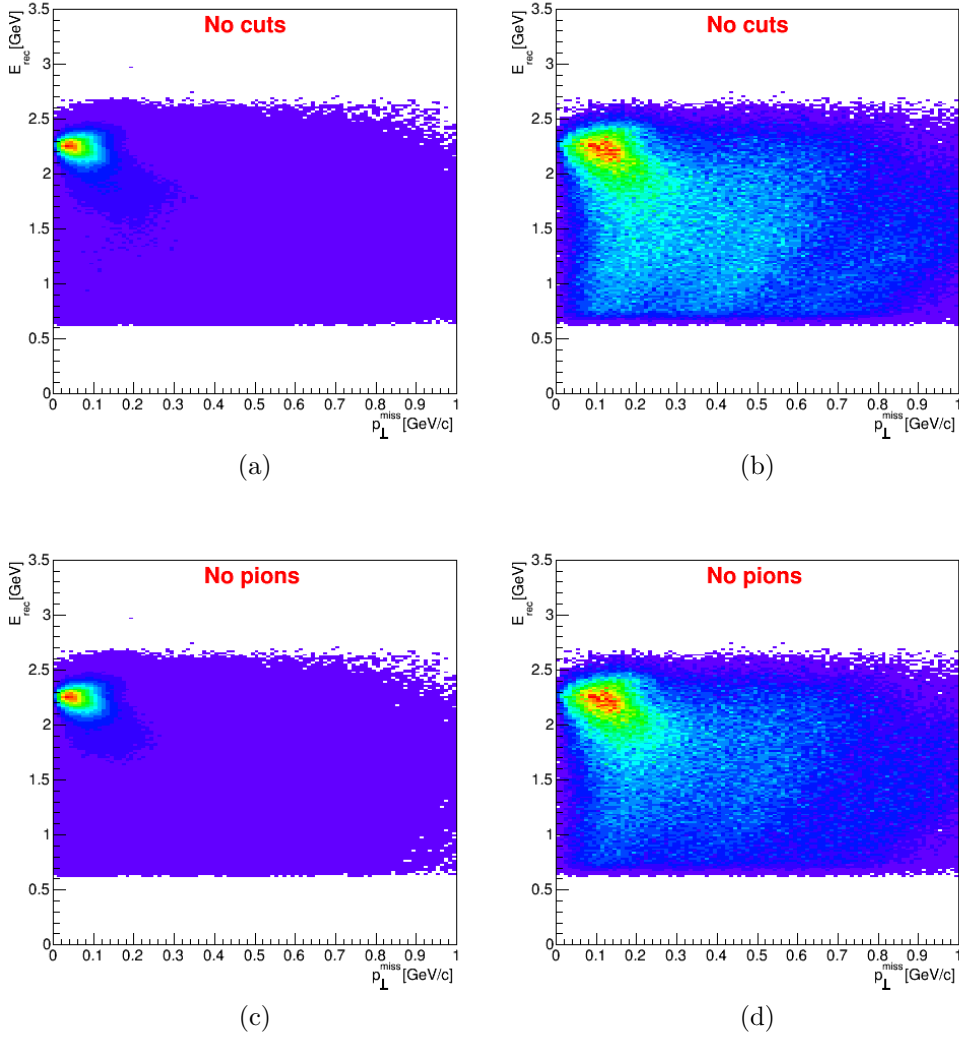


Figure 51: Reconstructed energy E_{rec} obtained using Eq. 7 as a function of the total perpendicular momentum of the scattered electron and the knockout nucleon system for ^3He and ^{56}Fe targets at 2.2 GeV before (top plots) and after (bottom plots) pion rejection cuts. (a),(c) ^3He ; (b),(d) ^{56}Fe .

^{56}Fe (Fig. 54c, 54d) targets are shown in Fig. 54.

I have combined the obtained results for different targets in one plot. The E_{rec} distributions of $A(e, e')$ (red) and $A(e, e'p)$ (green) no pion spectrum and E_{tot} distribution of $A(e, e'p)$ (blue) no pion spectrum after subtraction for undetected pions and undetected two proton events are shown in Fig. 55. The plots for ^3He can be found in 55a, for ^4He in 55b, for ^{12}C in 55c and the ones for ^{56}Fe in 55d.

We have then looked at E_{tot} (Fig. 56b, 56d) and E_{rec} (Fig. 56a, 56c) distributions of $A(e, e'p)$ no pion spectrum after subtraction for undetected pions and undetected protons for three different regions of p_{perp} (0 – 200 MeV/c, 200 – 400 MeV/c and 400 MeV/c and higher). The plots for ^3He are shown in Fig. 56a, 56b, and the ones for ^{56}Fe in Fig. 56c, 56d.

The plots for other targets (^4He and ^{12}C) for both beam energies are shown in A.2.

Comparison of 2.2 GeV and 4.4 GeV $A(e, e')$ and $A(e, e'p)$ analysis

We have combined the energy reconstruction results for different targets and beam energies in Fig. 57.

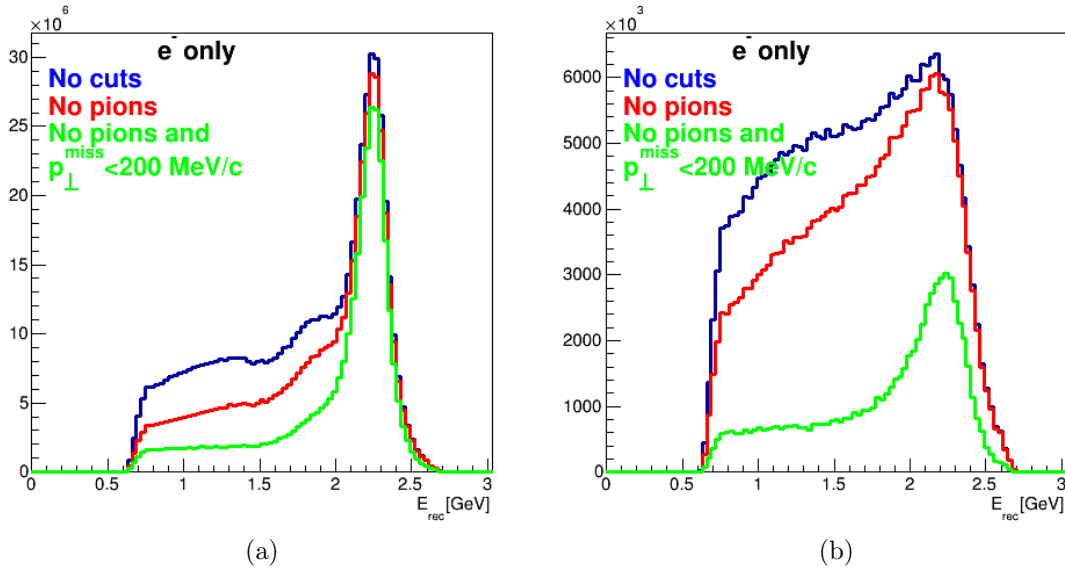


Figure 52: Reconstructed energy E_{rec} of $A(e, e')$ obtained using Eq. 7 with no cuts (blue), with pion rejection cut (red) and with cut on total perpendicular momentum of the scattered electron and the knockout nucleon system $p_{\text{perp}} < 200$ MeV/c in addition to pion rejection cut for ${}^3\text{He}$ and ${}^{56}\text{Fe}$ targets at 2.2 GeV (a) ${}^3\text{He}$; (b) ${}^{56}\text{Fe}$.

The plots on the left correspond to 2.2 GeV analysis, and the ones on the right correspond to 4.4 GeV. The plots on each of the rows correspond to different targets, and we go to heavier targets as we move from top the bottom.

It is evident from this figure that both energy reconstruction methods provide a better description of beam energy at lower beam energy (2.2 GeV). The peak in the corresponding distributions at the beam energy is narrower, and the background tail to the left of the peak is smaller with respect to the peak at lower beam energy. We can see that there isn't even an evident peak in the E_{rec} distributions of $A(e, e')$ and $A(e, e'p)$ events for ${}^{12}\text{C}$ and ${}^{56}\text{Fe}$ targets at 4.4 GeV.

We can also learn from the figures for the same beam energy but different targets that the non-QE background tail increases with respect to QE peak as we go to heavier nuclei.

We have estimated the fraction of the events that have their energy reconstructed within certain range (5%, 10% and 20%) around the true value of the beam energy for different energy reconstruction methods. The results for different targets and beam energies are shown in Tables 5, 6 and 5.

Target	2.2 GeV/c		4.4 GeV/c	
	$E_{\text{rec}}(e, e')$	$E_{\text{tot}}(e, e'p)$	$E_{\text{rec}}(e, e')$	$E_{\text{tot}}(e, e'p)$
${}^3\text{He}$	34%	54%	23%	36%
${}^4\text{He}$	25%	45%	17%	27%
${}^{12}\text{C}$	21%	38%	13%	24%
${}^{56}\text{Fe}$	17%	26%	9.7%	18%

Table 5: Fraction of events reconstructed within 5% of beam energy at 2.2 GeV and 4.4 GeV analysis. The invariant mass cut is applied to eliminate deep inelastic scattering events.

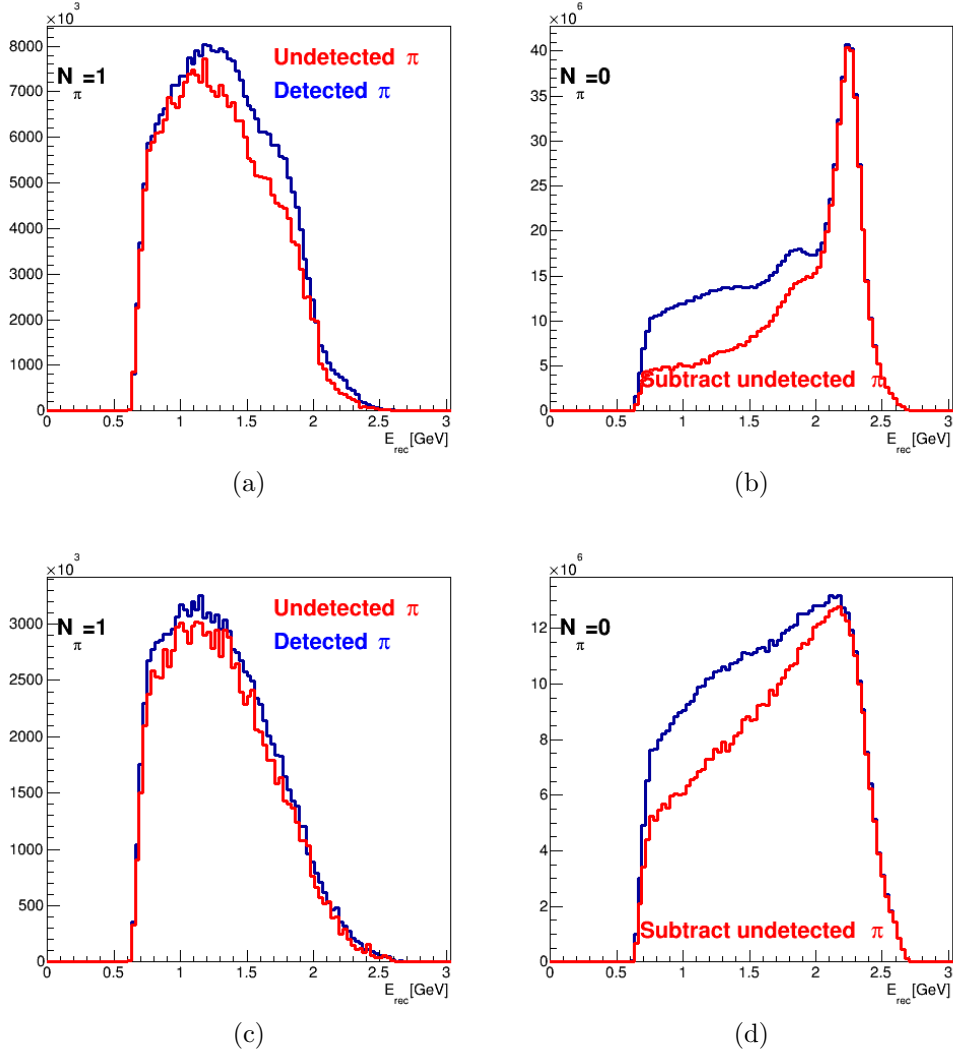


Figure 53: The E_{rec} obtained using Eq. 7, for detected (blue) and undetected (red) 1 pion events for (a) ${}^3\text{He}(e, e'\pi^\pm)$; (c) ${}^{56}\text{Fe}(e, e'\pi^\pm)$ at 2.2 GeV. Reconstructed energy E_{rec} of $\text{A}(e, e')$ no pion spectrum before (blue) and after (red) subtraction for undetected pions for (b) ${}^3\text{He}$ and (d) ${}^{56}\text{Fe}$ targets at 2.2 GeV.

4 To summarize

- This analysis demonstrates first use of electron data to test neutrino energy reconstruction algorithms. We have used zero-pion cuts to enhance QE event selection, as it is done in neutrino experiments. We have then reconstructed the beam energy using just the information of the scattered lepton (E_{rec}). This is the method used in Cherenkov-type neutrino detectors. We have also reconstructed the beam energy using the total energy of the electron and a proton system (E_{tot}). This method is used in calorimetric neutrino detectors. The results obtained using both energy reconstruction methods are improved by a transverse momentum cut to better select QE events.
- It is evident that E_{tot} method gives a better description of beam energy, however only 9.7 – 54% of events reconstruct to within 5% of the beam energy. The reconstruction works better for lighter nuclei and lower energies.

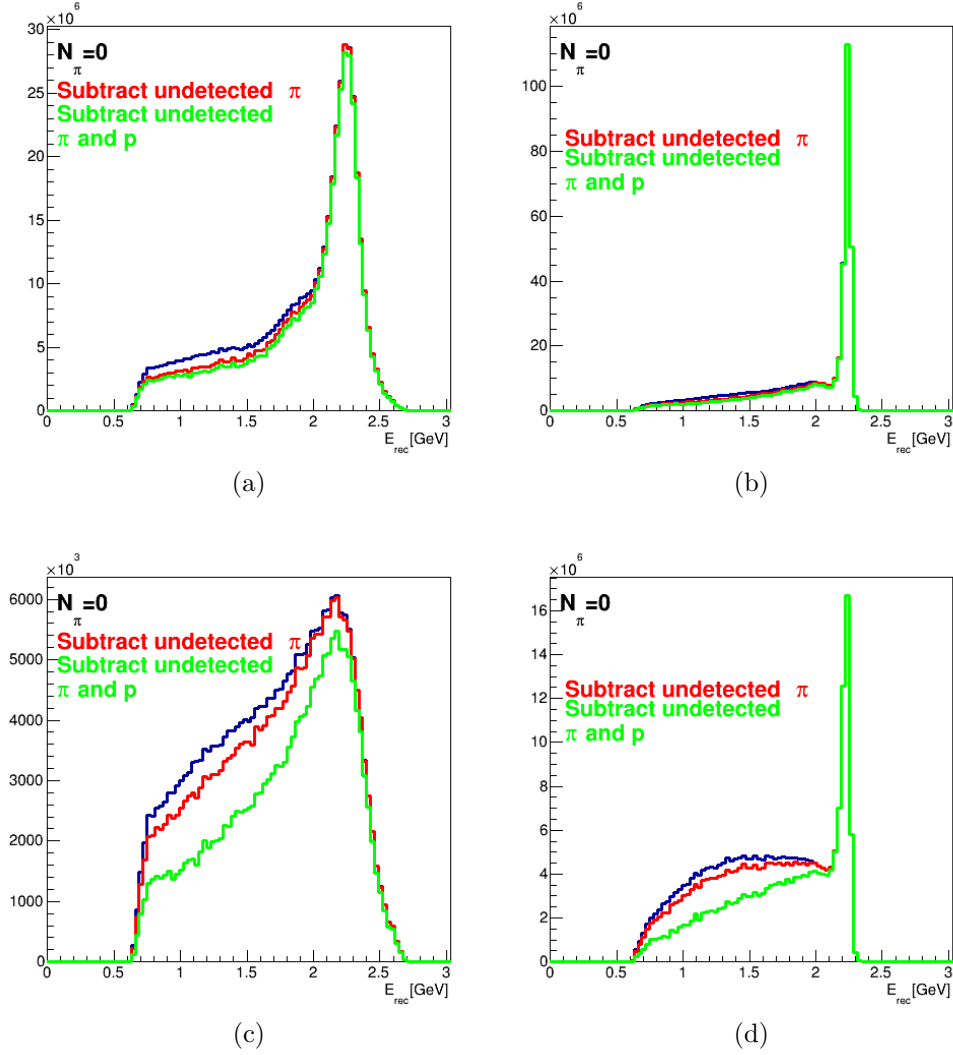


Figure 54: E_{rec} (plots on the left) and E_{tot} (plots on the right) distributions of $A(e, e'p)$ no pion spectrum before subtraction for undetected pions (blue), after subtraction for undetected pions (red) and after subtraction for undetected pions and undetected two proton events (green) for (a), (b) ^3He and (c), (d) ^{56}Fe targets at 2.2 GeV.

- This type of analysis have a tremendous interest in neutrino community and can have serious implications for neutrino oscillation measurements.
- We are planing to extend analysis to more targets and energies. Identify regions with good and bad energy reconstruction GENIE modeling. There is a proposal aimed to serve for these purposes with a title "Electrons for Neutrinos" and proposal number "PR12-17-006" that has been submitted to PAC 45 and was conditionally approved (with C2 PAC decision).

References

- [1] S. Abe and T. Abihara, "Comparing and contrasting nuclei and cold atomic gases," *Phys.Rev.Lett*, vol. 100, p. 221803, 2008.

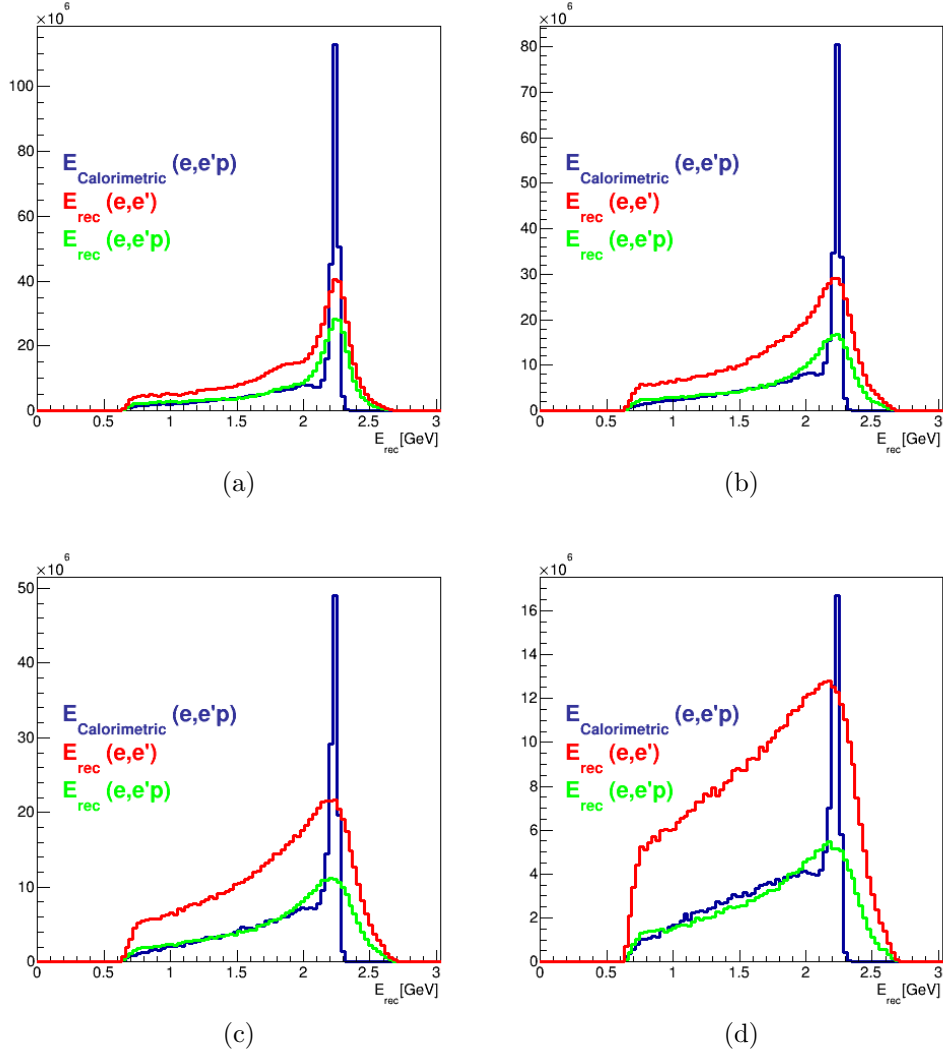


Figure 55: E_{rec} distributions of $A(e, e')$ (red) and $A(e, e'p)$ (green) no pion spectrum and E_{tot} distribution of $A(e, e'p)$ (blue) no pion spectrum after subtraction for undetected pions and undetected two proton events for (a) ${}^3\text{He}$, (b) ${}^4\text{He}$, (c) ${}^{12}\text{C}$ and (d) ${}^{56}\text{Fe}$ targets at 2.2 GeV.

- [2] D. Protopopescu, “Measurements of a'_{LT} asymmetries in $(e, e'p)$ reactions on ${}^4\text{He}$ and ${}^{12}\text{C}$,” *CLAS Analysis Paper*, 2003.
- [3] R. Niyazov, *Measurement of Correlated Pair Momentum Distributions on ${}^3\text{He}(e, e'pp)n$ with CLAS*. PhD thesis, Old Dominion University, 2003.
- [4] M. Osipenko *et al.*, “Measurement of deuteron structure function F_2 in the resonance region and evaluation of its moments,” *Phys.Rev.C*, vol. 73, p. 045205, 2006.
- [5] D. Protopopescu, “Electron momentum corrections for CLAS at 4.4 GeV,” *CLAS-NOTE 2001-008 JLAB*, 2001.
- [6] B. Zhang, *Searching for Short Range Correlations Using $(e, e'NN)$ Reactions*. PhD thesis, MIT, 2003.

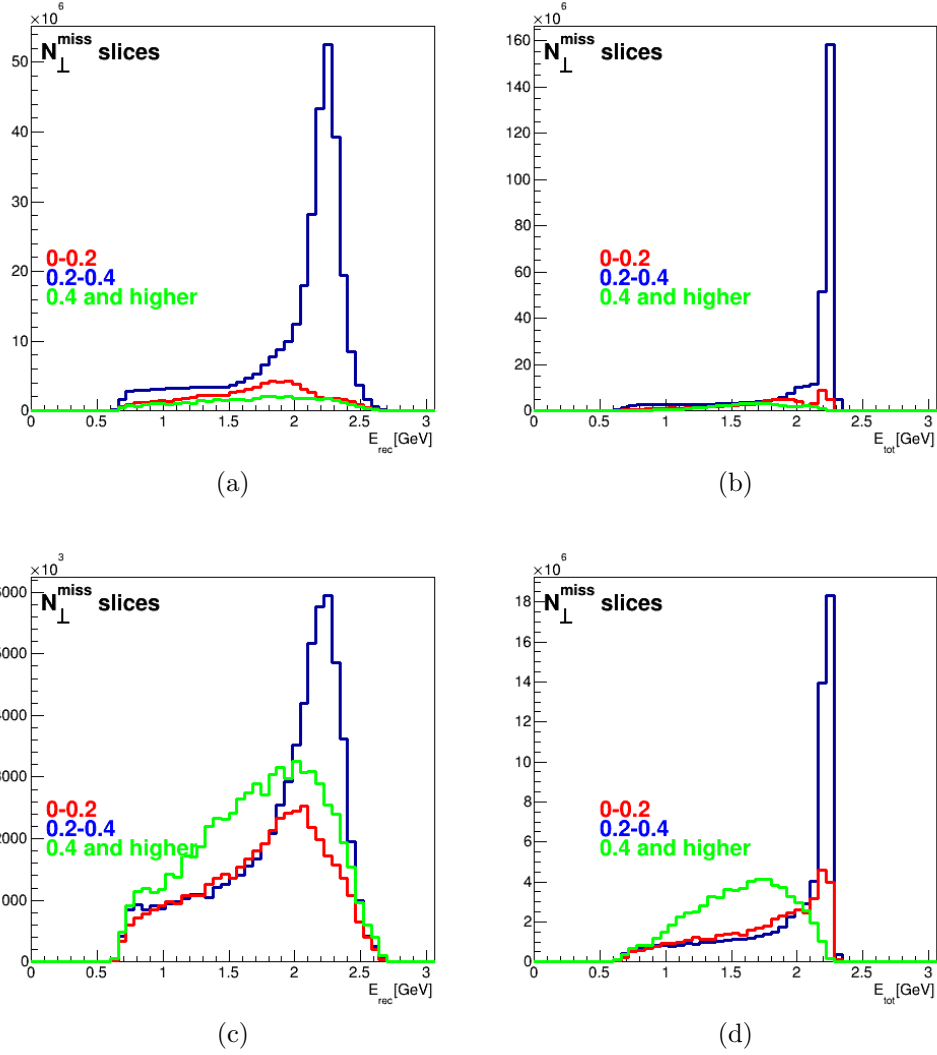


Figure 56: E_{tot} ((b) and (d)) and E_{rec} ((a) and (c)) distributions of $A(e, e'p)$ no pion spectrum after subtraction for undetected pions and undetected protons for three different regions of p_{perp} (0–200 MeV/c, 200 – 400 MeV/c and 400 MeV/c and higher) for (a), (b) ^3He and (c), (d) ^{56}Fe targets at 2.2 GeV.

- [7] B. Zhang, “Electron momentum correction.” <https://www.jlab.org/Hall-B/secure/e2/bzh/momcorrection.html>, 2003.
- [8] D. Protopopescu, “Fiducial cuts for electrons in the CLAS/E2 data at 4.4 GeV,” *CLAS-NOTE 2000-007 JLAB*, 2000.
- [9] B. Zhang, “Electron fiducial cuts.” <https://www.jlab.org/Hall-B/secure/e2/bzh/efiducialcut.html#edge>, 2003.
- [10] L. W. Rustam Niyazov, “Fiducial cut for positive hadrons in CLAS/E2 data at 4.4 GeV,” *CLAS-NOTE 2001-013 JLAB*, 2001.
- [11] B. Zhang, “Positive hadron fiducial cuts.” <https://www.jlab.org/Hall-B/secure/e2/bzh/pfiducialcut.html>, 2003.

Target	2.2 GeV/c		4.4 GeV/c	
	$E_{\text{rec}}(e, e')$	$E_{\text{tot}}(e, e'p)$	$E_{\text{rec}}(e, e')$	$E_{\text{tot}}(e, e'p)$
^3He	45%	61%	35%	44%
^4He	40%	54%	28%	35%
^{12}C	37%	48%	23%	32%
^{56}Fe	30%	35%	18%	26%

Table 6: Fraction of events reconstructed within 10% of beam energy at 2.2 GeV and 4.4 GeV analysis. The invariant mass cut is applied to eliminate deep inelastic scattering events.

Target	2.2 GeV/c		4.4 GeV/c	
	$E_{\text{rec}}(e, e')$	$E_{\text{tot}}(e, e'p)$	$E_{\text{rec}}(e, e')$	$E_{\text{tot}}(e, e'p)$
^3He	66%	73%	53%	58%
^4He	59%	68%	46%	51%
^{12}C	56%	64%	41%	47%
^{56}Fe	48%	52%	33%	41%

Table 7: Fraction of events reconstructed within 20% of beam energy at 2.2 GeV and 4.4 GeV analysis. The invariant mass cut is applied to eliminate deep inelastic scattering events.

- [12] S. S. Nathan Baltzell, “Beam XY-position at the target for clas/eg6,” *CLAS-NOTE 2013-007 JLAB*, 2013.

A Appendix

A.1 Z-vertex correction and cuts of protons and electrons for ^4He , ^{12}C and ^{56}Fe targets for 2.2 GeV and 4.4 GeV beam energies.

4.4 GeV analysis

We have obtained individual vertex correction functions for each of the targets. We have then used this correction function to correct the proton and electron vertexes. To get idea about the quality of applied corrections we have looked at the vertex distributions before and after vertex corrections explained in details in current analysis.

The vertex cuts for different target and beam energy analysis can be found in Table. 3.

The plots of electron ϕ azimuthal angle as a function of z vertex for ^4He at 4.4 GeV target before and after corrections are shown in Fig. 58. We can see that after applied correction the target region, which represents a cryotarget cell full of liquid ^4He , and the heat shield region to the right of it are nicely aligned for electrons detected in different CLAS sectors. We can also see an improvement in electron vertex distribution shown in the left of Fig. 59, by comparing the distributions before and after vertex corrections and looking at the difference between electron and proton vertexes on the right side of the figure.

In Fig. 60 we can see the plots of electron ϕ azimuthal angle as a function of z vertex for ^{12}C at 4.4 GeV target. The carbon target was placed in front of the empty cryotarget cell and that is the structure we see in the figure. Again it looks like the vertex correction works fine. The same can be seen in electron vertex distribution plots before and after correction shown in the left side of Fig. 61 and the plot of the difference of electron and proton vertexes in the right side of Fig. 61.

The second solid target used in this analysis is the iron. The plots of electron ϕ azimuthal angle as a function of z vertex for ^{56}Fe at 4.4 GeV target before and after corrections are shown in Fig. 62. The empty cryotarget cell was also present during the ^{56}Fe at 4.4 GeV and so the very left peak in the electron vertex distribution in right side of Fig. 63 corresponds to the front window of the liquid target cell, the small peak next to it corresponds to the heat shield and the large peak to the right of the heat shield region corresponds to the solid target region.

2.2 GeV analysis

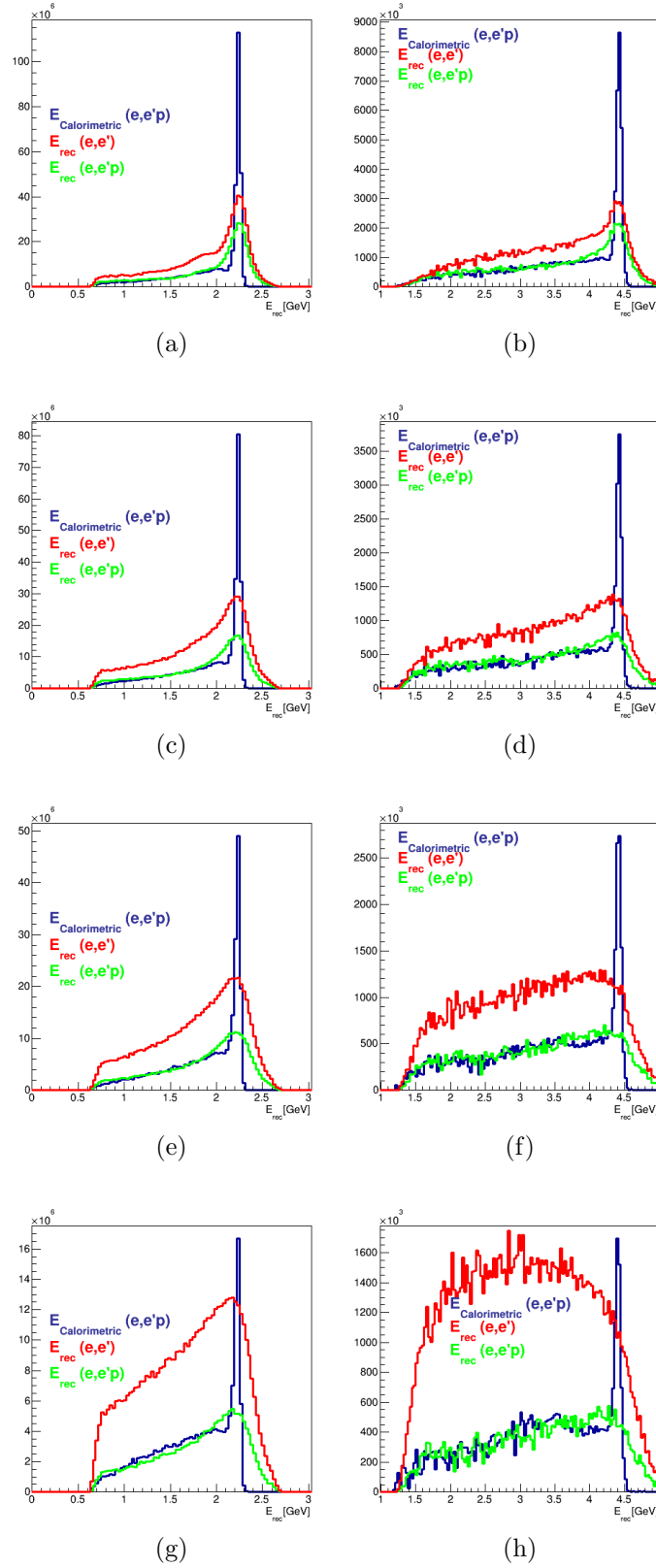
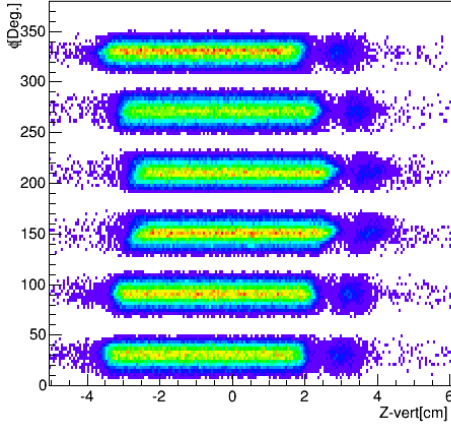
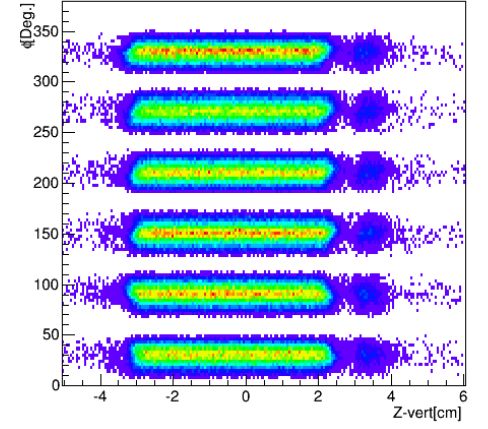


Figure 57: E_{rec} distributions of $A(e, e')$ (red) and $A(e, e'p)$ (green) no pion spectrum and E_{tot} distribution of $A(e, e'p)$ (blue) no pion spectrum after subtraction for undetected pions and undetected two proton events for (a), (b) ^3He , (c), (d) ^4He , (e), (f) ^{12}C and (g), (h) ^{56}Fe targets at 2.2 GeV (plots on the left) and at 4.4 GeV (plots on the right).

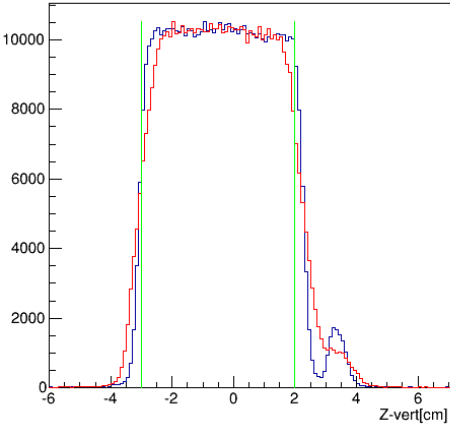


(a) Before correction.

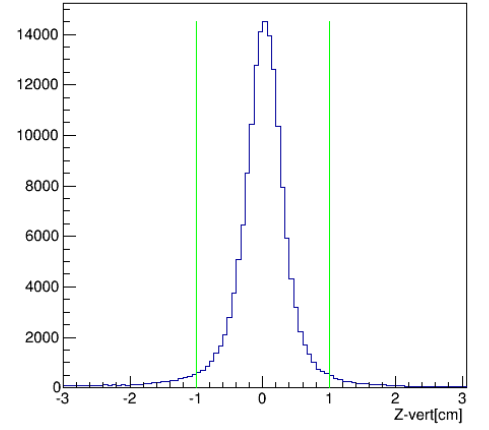


(b) After correction.

Figure 58: The ϕ angle of the electrons plotted vs z component of vertex in logarithmic scale. The results are shown for ^4He target at 4.4 GeV.

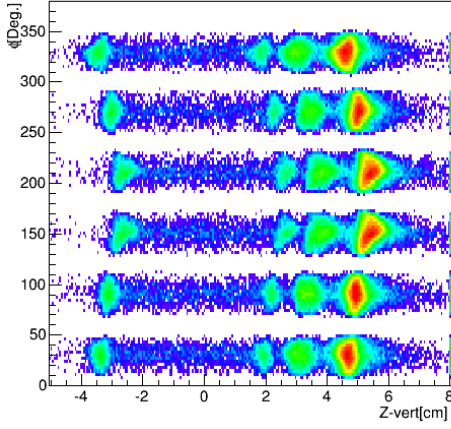


(a)

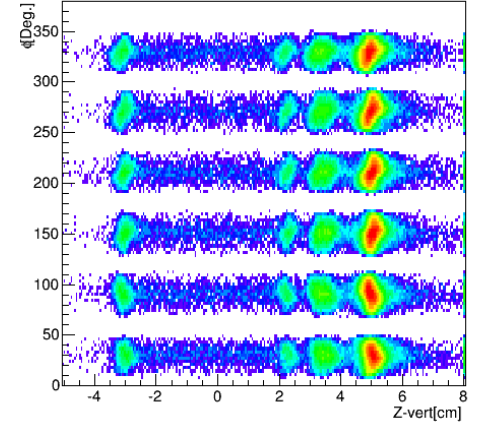


(b)

Figure 59: a) The distributions of electron z vertex before (red) and after (blue) correction. b) The distribution of electron and proton z vertex differences. The green lines correspond to the applied cut. Both plots are made for ^4He at 4.4 GeV.

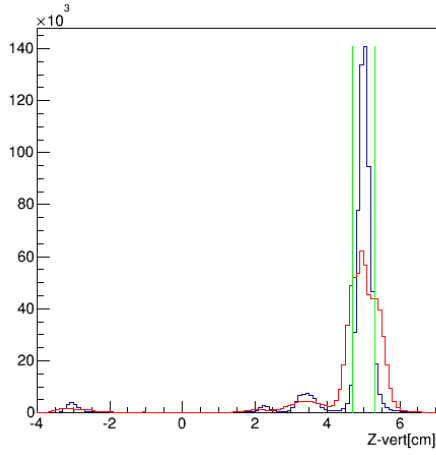


(a) Before correction.

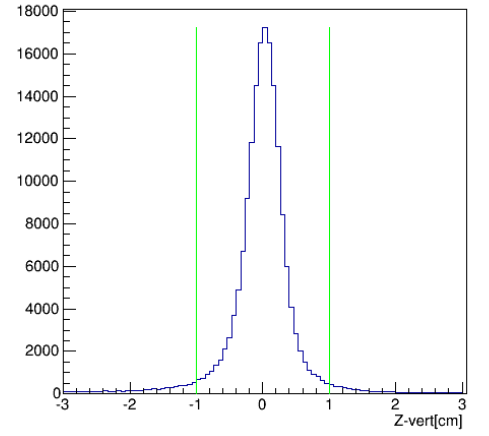


(b) After correction.

Figure 60: The ϕ angle of the electrons plotted vs z component of vertex in logarithmic scale. The results are shown for ^{12}C target at 4.4 GeV.

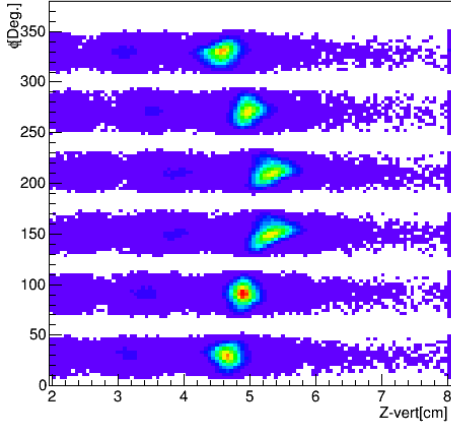


(a)

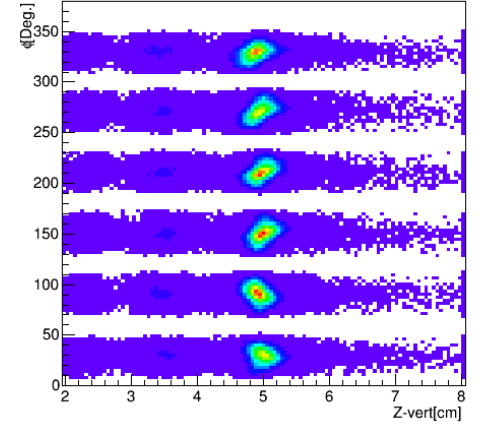


(b)

Figure 61: a) The distributions of electron z vertex before (red) and after (blue) correction. b) The distribution of electron and proton z vertex differences. The green lines correspond to the applied cut. Both plots are made for ^{12}C at 4.4 GeV.

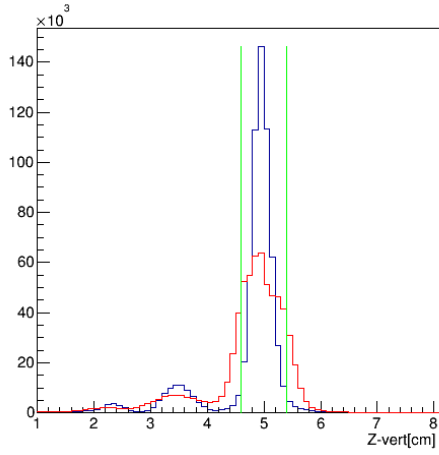


(a) Before correction.

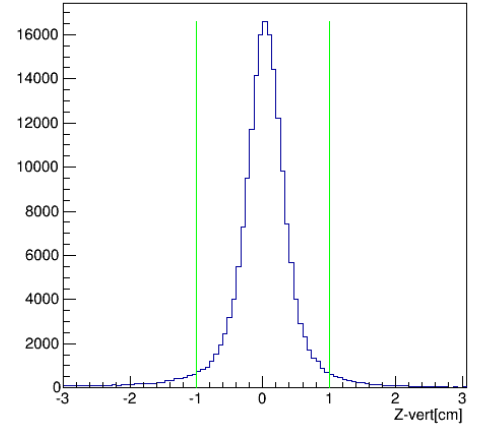


(b) After correction.

Figure 62: The ϕ angle of the electrons plotted vs z component of vertex in logarithmic scale. The results are shown for ^{56}Fe target at 4.4 GeV.



(a)



(b)

Figure 63: a) The distributions of electron z vertex before (red) and after (blue) correction. b) The distribution of electron and proton z vertex differences. The green lines correspond to the applied cut. Both plots are made for ^{56}Fe at 4.4 GeV.

We can again see the liquid target region and the heat shield region to the right for ^4He at 2.2 GeV in Fig. 64. The left plot represents electron ϕ azimuthal angle as a function of z vertex before vertex corrections and the one on the right shows the same distributions after vertex corrections. We can see in the left plot of Fig. 65 that the peak in vertex distribution corresponding to heat shield region becomes much more evident after applied correction.



Figure 64: The ϕ angle of the electrons plotted vs z component of vertex in logarithmic scale. The results are shown for ^4He target at 2.2 GeV.

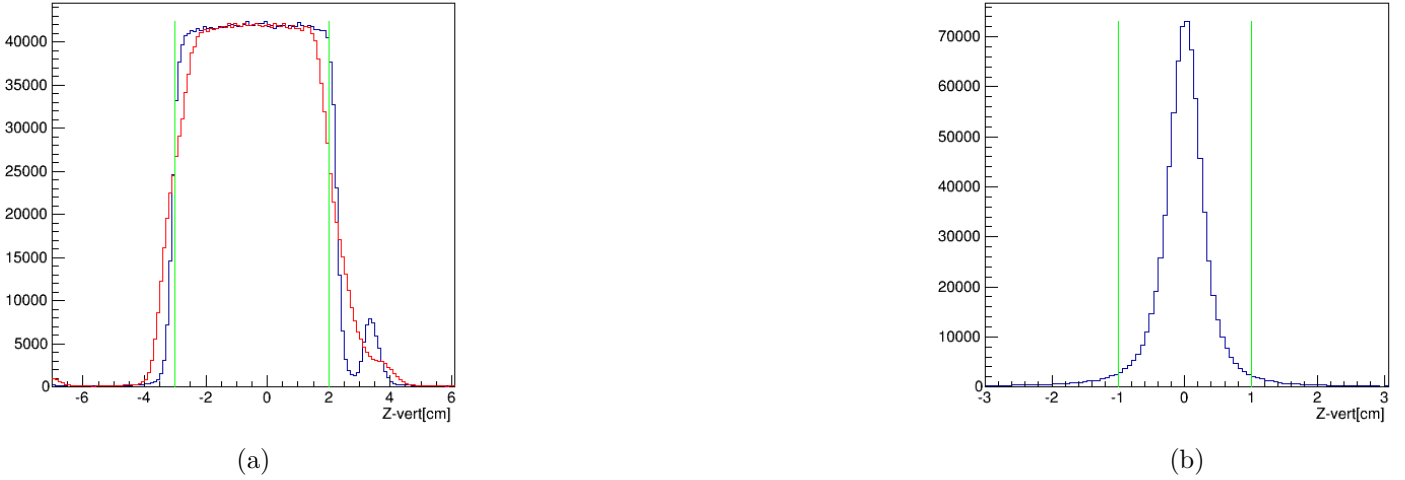
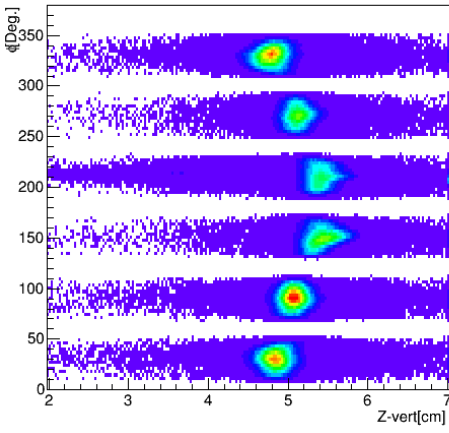


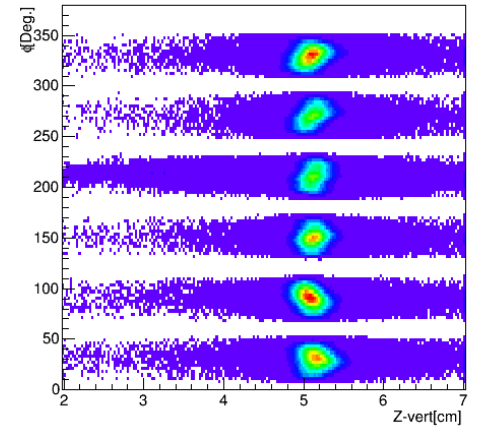
Figure 65: a)The distributions of electron z vertex before (red) and after (blue) correction.b)The distribution of electron and proton z vertex differences. The green lines correspond to the applied cut. Both plots are made for ^4He at 2.2 GeV.

The plots of ϕ azimuthal angle as a function of z vertex for ^{12}C analysis at 2.2 GeV can be found in Fig. 66. The left plot shows the distributions before vertex correction and the left one after correction.

The plots of electron z vertex distributions before and after correction and the difference between z vertexes of an electron and a proton are shown in the left and right sides of Fig. 67 respectively.

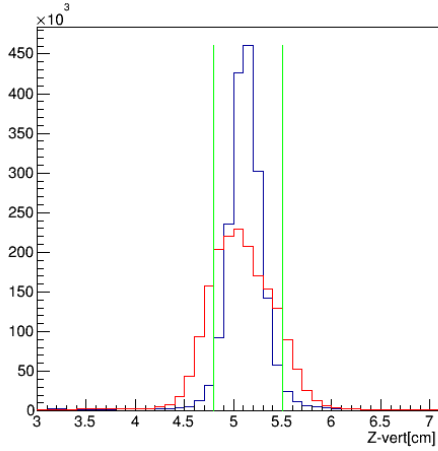


(a) Before correction.

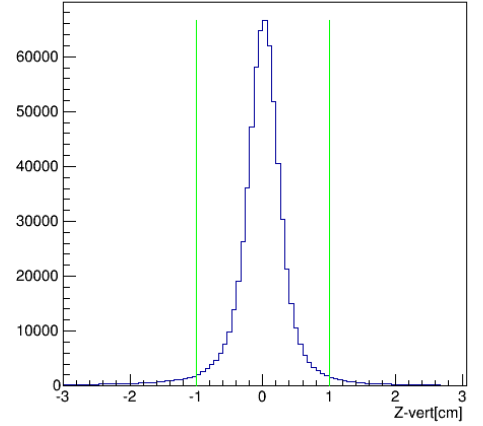


(b) After correction.

Figure 66: The ϕ angle of the electrons plotted vs z component of vertex in logarithmic scale. The results are shown for ^{12}C target at 2.2 GeV.



(a)



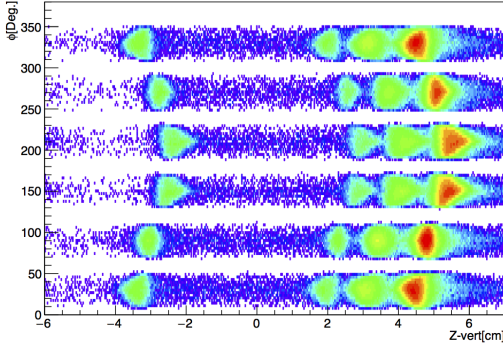
(b)

Figure 67: a) The distributions of electron z vertex before (red) and after (blue) correction. b) The distribution of electron and proton z vertex differences. The green lines correspond to the applied cut. Both plots are made for ^{12}C at 2.2 GeV.

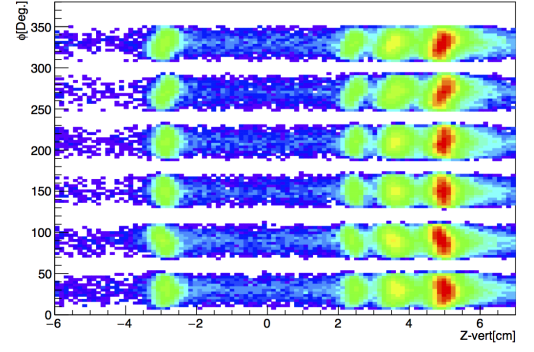
The ϕ azimuthal angle as a function of z vertex for ^{56}Fe analysis at 2.2 GeV is shown in Fig. 68. The left plot shows the distributions before vertex correction and the right one after correction.

The plots of electron z vertex distributions before and after correction and the difference between z vertexes of an electron and a proton are shown in the left and right sides of Fig. 69 respectively.

Nearly half of the data with ^{56}Fe target at 2.2 GeV was taken with presumably an exploded liquid target cell (referred in here as 2nd run group). The ϕ azimuthal angle as a function of z vertex for these runs is shown in Fig. 70. In the left plot corresponding to the distribution before vertex correction, we can see that the peak corresponding to solid target region (very right side) is isolated from the rest of the distribution good enough to be selected and used in the analysis. We then obtained separate correction function for this part of ^{56}Fe data and corrected the z vertexes of electrons and protons. The right plot

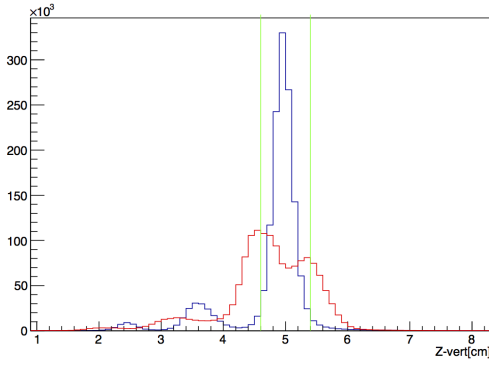


(a) Before correction.

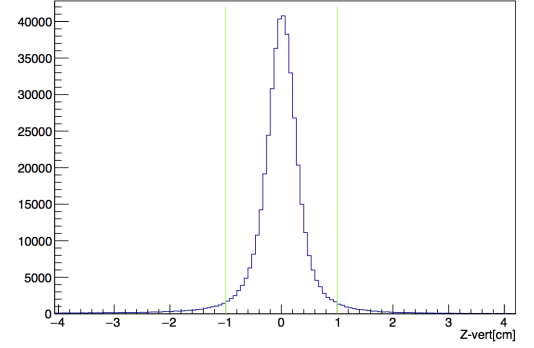


(b) After correction.

Figure 68: The ϕ angle of the electrons plotted vs z component of vertex in logarithmic scale. The results are shown for ^{56}Fe target at 2.2 GeV (1nd run group).



(a)



(b)

Figure 69: a) The distributions of electron z vertex before (red) and after (blue) correction. b) The distribution of electron and proton z vertex differences. The green lines correspond to the applied cut. Both plots are made for ^{56}Fe at 2.2 GeV (1nd run group).

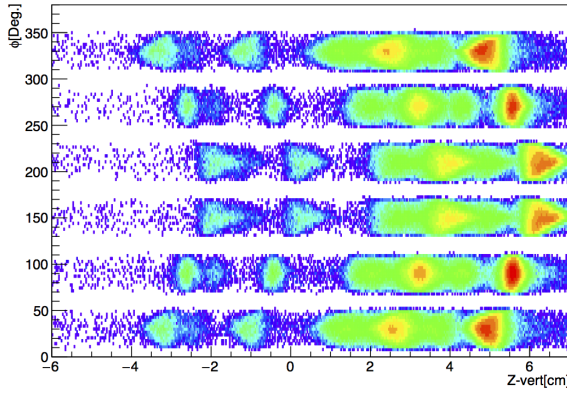
shows the distribution of ϕ azimuthal angle as a function of z vertex after vertex correction.

The plots of electron z vertex distributions for these runs, before and after correction and the difference between z vertexes of an electron and a proton are shown in the left and right sides of Fig. 71 respectively. The green lines correspond to the applied cuts.

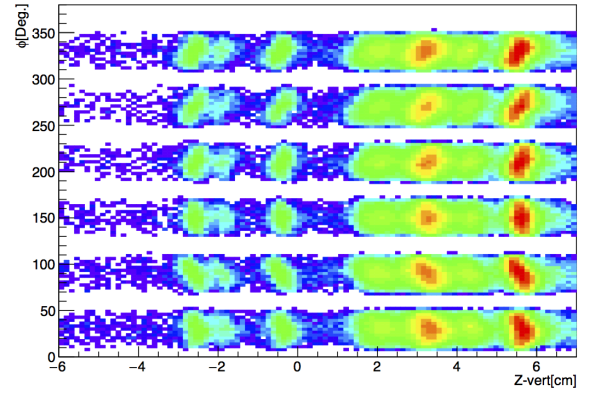
A.2 The $A(e, e')$ and $A(e, e'p)$ analysis plots for ^4He and ^{12}C targets for 2.2 GeV and 4.4 GeV beam energies.

4.4 GeV $A(e, e')$ and $A(e, e'p)$ analysis

The multiplicity plots of proton and charged pion for ^4He and ^{12}C targets are shown in 73 and 72 correspondingly.

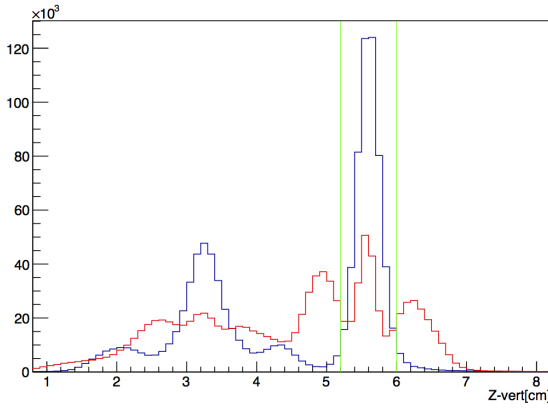


(a) Before correction.

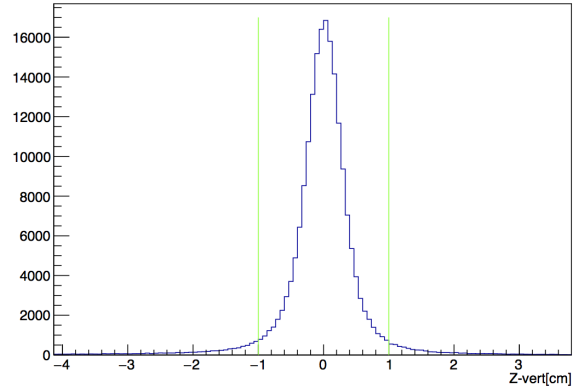


(b) After correction.

Figure 70: The ϕ angle of the electrons plotted vs z component of vertex in logarithmic scale. The results are shown for ^{56}Fe target at 2.2 GeV for runs with exploded liquid target cell (2nd run group).



(a)



(b)

Figure 71: a) The distributions of electron z vertex before (red) and after (blue) correction. b) The distribution of electron and proton z vertex differences. The green lines correspond to the applied cut. Both plots are made for ^{56}Fe at 2.2 GeV for runs with exploded liquid target cell (2nd run group).

The E_{rec} distributions of $A(e, e')$ events, after different cuts are shown in 75. We can see the plot of E_{rec} as a function of p_{perp} after $p_{\text{perp}} < 200$ MeV and pion rejection cuts in Fig. 74. The plots are shown for ^4He (Fig. 74a, Fig. 74c) and ^{12}C (Fig. 74b, Fig. 74d) targets before (top plots) and after (bottom plots) pion rejection cuts.

The distributions of E_{rec} for detected (blue) and undetected (red) 1 pion events for $^4\text{He}(e, e'\pi^\pm)$ are shown in Fig. 76a, and the ones for $^{12}\text{C}(e, e'\pi^\pm)$ in Fig. 76c. The E_{rec} distributions of 0 pion spectrum before (blue) and after (red) subtraction for undetected pions for $^4\text{He}(e, e')$ are shown in Fig. 76b and the ones for $^{12}\text{C}(e, e')$ are shown in Fig. 76d.

In Fig. 77 we can see E_{rec} (plots on the left) and E_{tot} (plots on the right) distributions of $A(e, e'p)$ no pion spectrum before subtraction for undetected pions (blue), after subtraction for undetected pions (red) and after subtraction for undetected pions and undetected two proton events (green) for ^4He (Fig. 77a, 77b) and ^{12}C (Fig. 77c, 77d) targets.

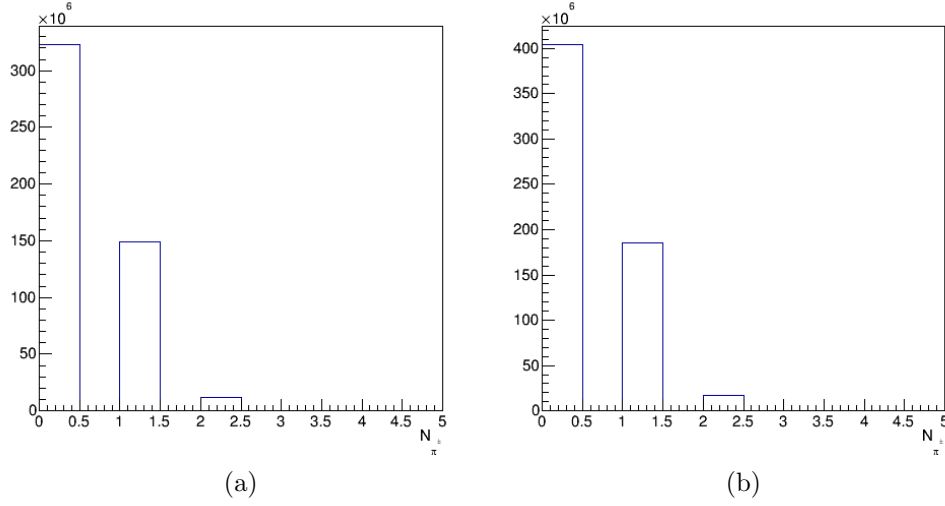


Figure 72: Multiplicity distributions of π^\pm for ^4He and ^{12}C targets at 4.4 GeV (a) ^4He ; (b) ^{12}C .

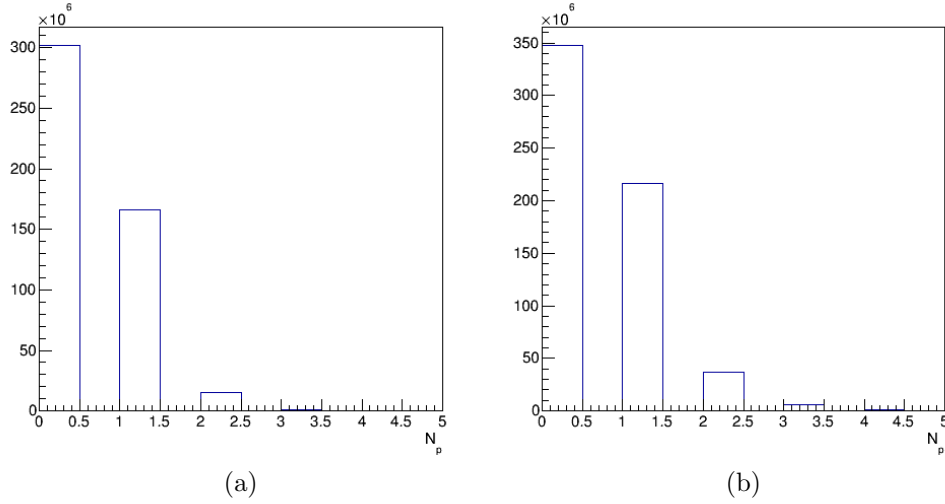


Figure 73: Multiplicity distributions of protons for ^4He and ^{12}C targets at 4.4 GeV (a) ^4He ; (b) ^{12}C .

We have also plot E_{tot} (Fig. 78b, 78d) and E_{rec} (Fig. 78a, 78c) distributions of $A(e, e'p)$ no pion spectrum after subtraction for undetected pions and undetected protons for three different regions of p_{perp} ($0 - 200$ MeV/c, $200 - 400$ MeV/c and 400 MeV/c and higher). The plots for ^4He are shown in Fig. 78a, 78b, and the ones for ^{12}C in Fig. 78c, 78d.

2.2 GeV $A(e, e')$ and $A(e, e'p)$ analysis

The proton and charged pion multiplicity plots are shown in 80 and 79 correspondingly.

The E_{rec} distributions of $A(e, e')$ events obtained using Eq. 7 after different cuts are shown in 82. We can see the plot of E_{rec} as a function of p_{perp} after $p_{\text{perp}} < 200$ MeV and pion rejection cuts in Fig.81. The plots are shown for ^4He (Fig. 81a, Fig. 81c) and ^{12}C (Fig. 81b, Fig. 81d) targets before (top plots) and after (bottom plots) pion rejection cuts.

The distributions of E_{rec} for detected (blue) and undetected (red) 1 pion events for $^4\text{He}(e, e'\pi^\pm)$ are

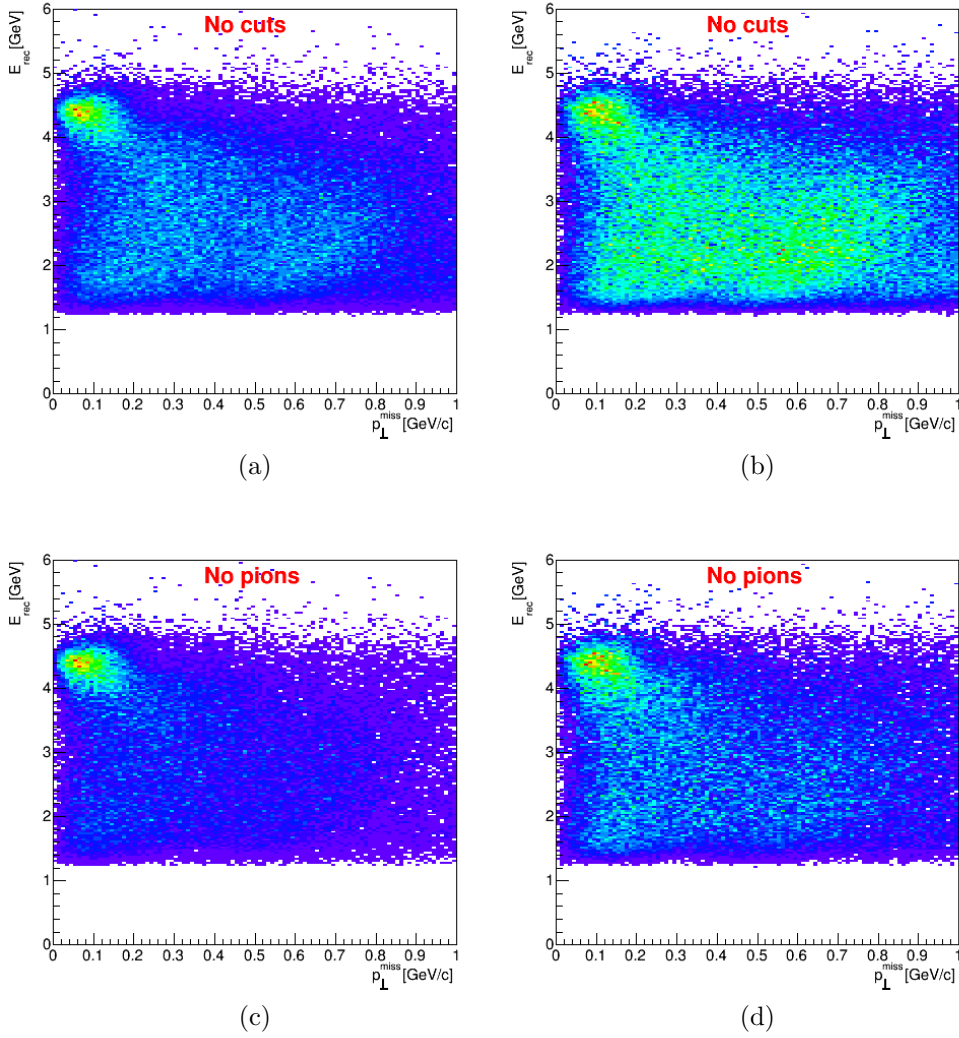


Figure 74: Reconstructed energy E_{rec} obtained using Eq. 7 as a function of the total perpendicular momentum of the scattered electron and the knockout nucleon system for ^4He and ^{12}C targets at 4.4 GeV before (top plots) and after (bottom plots) pion rejection cuts. (a),(c) ^4He ; (b),(d) ^{12}C .

shown in Fig. 83a, and the ones for $^{12}\text{C}(e, e'\pi^\pm)$ in Fig. 83c. The E_{rec} distributions of 0 pion spectrum before (blue) and after (red) subtraction for undetected pions for $^4\text{He}(e, e')$ are shown in Fig. 83b and the ones for $^{12}\text{C}(e, e')$ are shown in Fig. 83d.

In Fig. 84 we can see E_{rec} (plots on the left) and E_{tot} (plots on the right) distributions of $A(e, e'p)$ no pion spectrum before subtraction for undetected pions (blue), after subtraction for undetected pions (red) and after subtraction for undetected pions and undetected two proton events (green) for ^4He (Fig. 84a, 84b) and ^{12}C (Fig. 84c, 84d) targets.

We have then plot E_{tot} (Fig. 85b, 85d) and E_{rec} (Fig. 85a, 85c) distributions of $A(e, e'p)$ no pion spectrum after subtraction for undetected pions and undetected protons for three different regions of p_{perp} (0 – 200 MeV/c, 200 – 400 MeV/c and 400 MeV/c and higher). The plots for ^4He are shown in Fig. 85a, 85b, and the ones for ^{12}C in Fig. 85c, 85d.

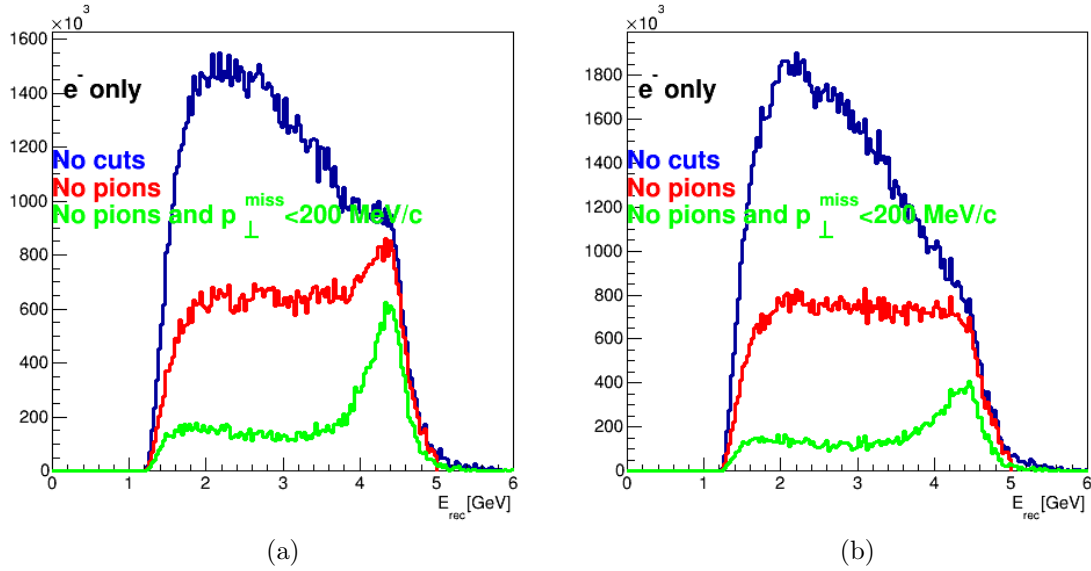
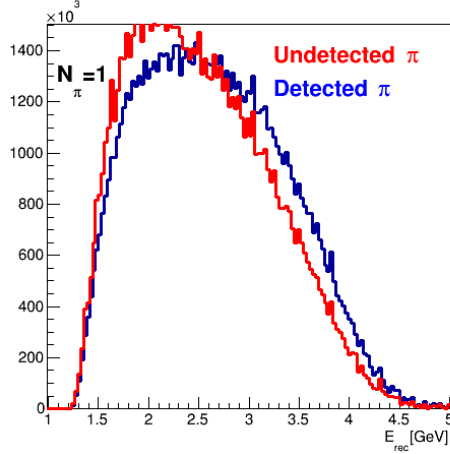
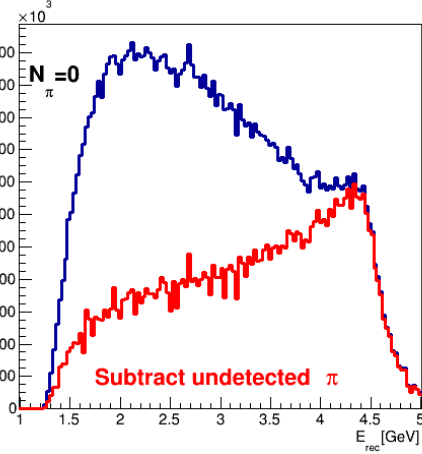


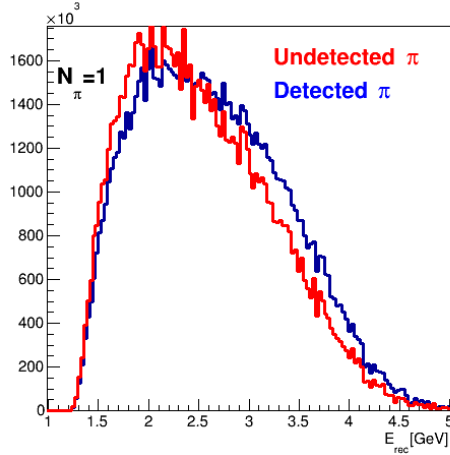
Figure 75: Reconstructed energy E_{rec} of $A(e, e')$ obtained using Eq. 7 with no cuts (blue), with pion rejection cut (red) and with cut on total perpendicular momentum of the scattered electron and the knockout nucleon system $p_{\text{perp}} < 200 \text{ MeV}$ in addition to pion rejection cut for ^4He and ^{12}C targets at 4.4 GeV (a) ^4He ; (b) ^{12}C .



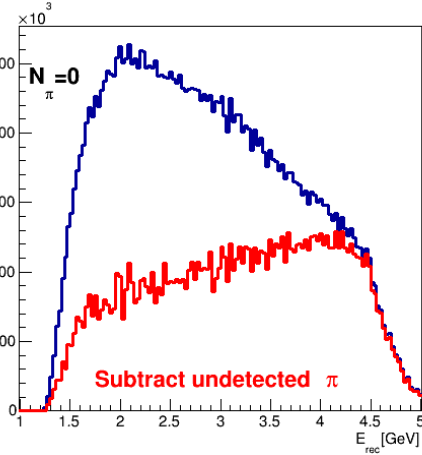
(a)



(b)

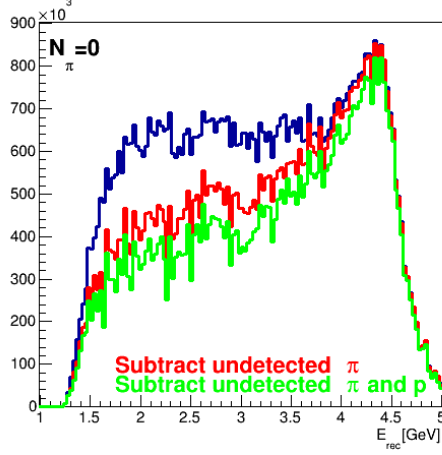


(c)

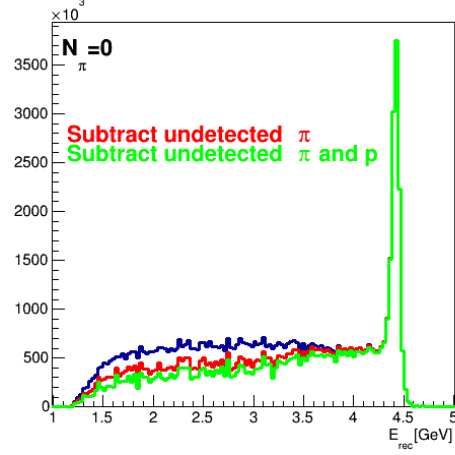


(d)

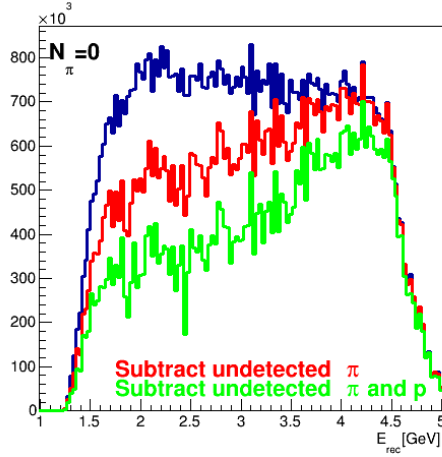
Figure 76: The E_{rec} obtained using Eq. 7, for detected (blue) and undetected (red) 1 pion events for (a) ${}^4\text{He}(e, e'\pi^\pm)$; (c) ${}^{12}\text{C}(e, e'\pi^\pm)$ at 4.4 GeV. Reconstructed energy E_{rec} of $A(e, e')$ no pion spectrum before (blue) and after (red) subtraction for undetected pions for (b) ${}^4\text{He}$ and (d) ${}^{12}\text{C}$ targets at 4.4 GeV.



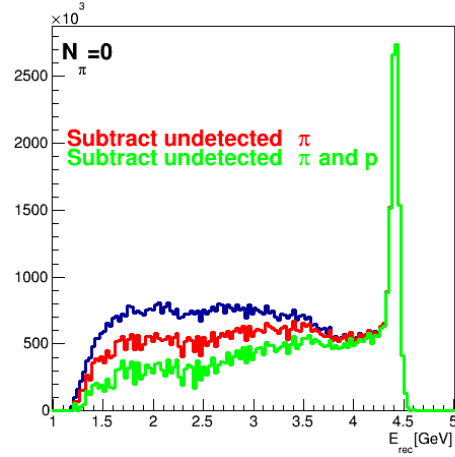
(a)



(b)

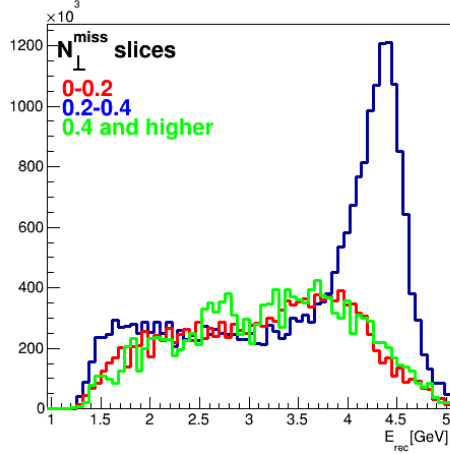


(c)

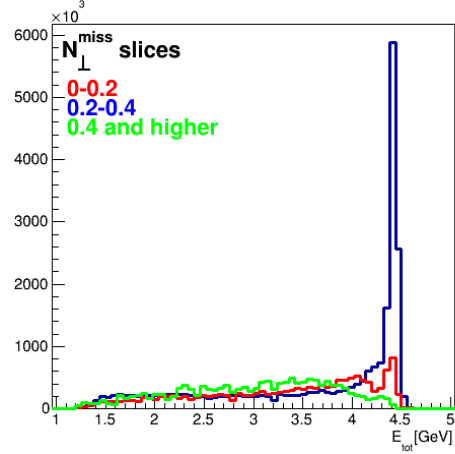


(d)

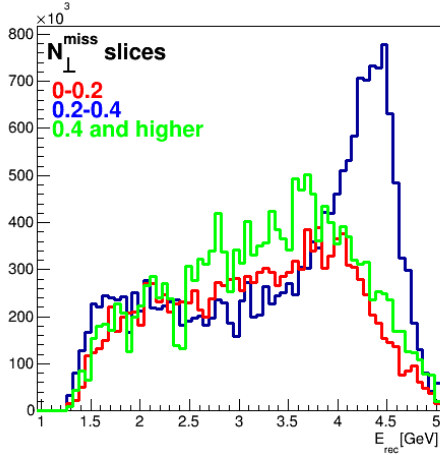
Figure 77: E_{rec} (plots on the left) and E_{tot} (plots on the right) distributions of $A(e, e'p)$ no pion spectrum before subtraction for undetected pions (blue), after subtraction for undetected pions (red) and after subtraction for undetected pions and undetected two proton events (green) for (a), (b) ^4He and (c),(d) ^{12}C targets at 4.4 GeV.



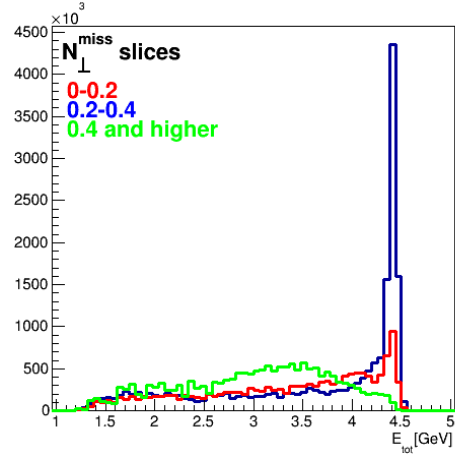
(a)



(b)

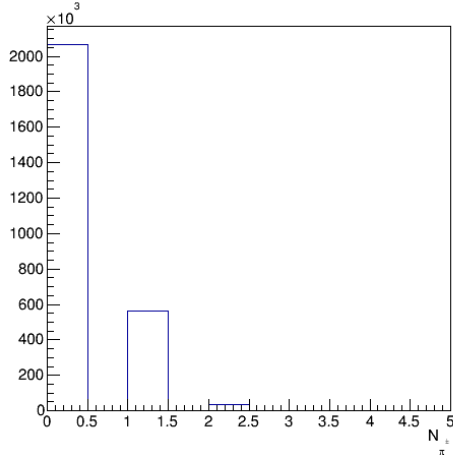


(c)

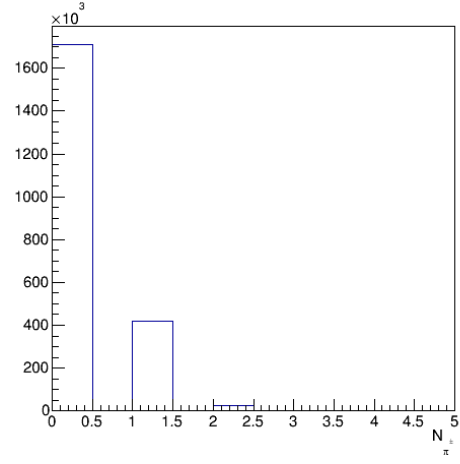


(d)

Figure 78: E_{tot} ((b) and (d)) and E_{rec} ((a) and (c)) distributions of $A(e, e'p)$ no pion spectrum after subtraction for undetected pions and undetected protons for three different regions of p_{perp} ($0-200$ MeV/c, $200-400$ MeV/c and 400 MeV/c and higher) for (a), (b) ^4He and (c), (d) ^{12}C targets at 4.4 GeV.

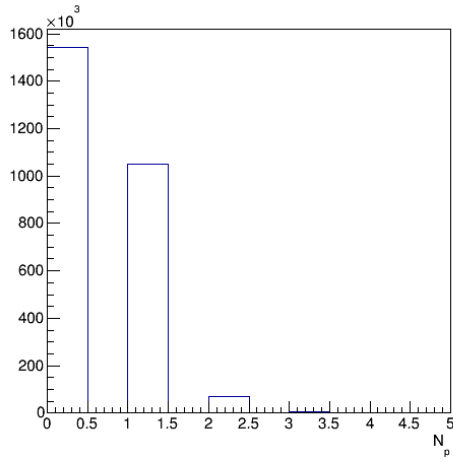


(a)

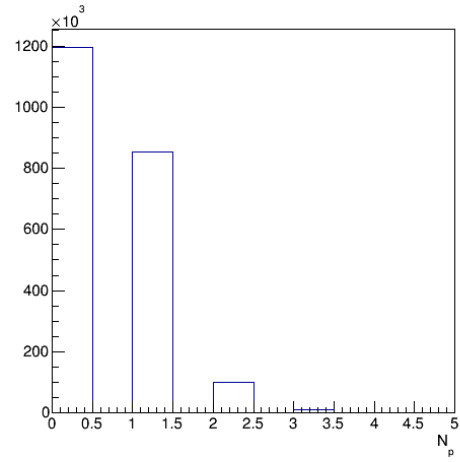


(b)

Figure 79: Multiplicity distributions of π^\pm for ^4He and ^{12}C targets at 2.2 GeV (a) ^4He ; (b) ^{12}C .



(a)



(b)

Figure 80: Multiplicity distributions of protons for ^4He and ^{12}C targets at 2.2 GeV (a) ^4He ; (b) ^{12}C .

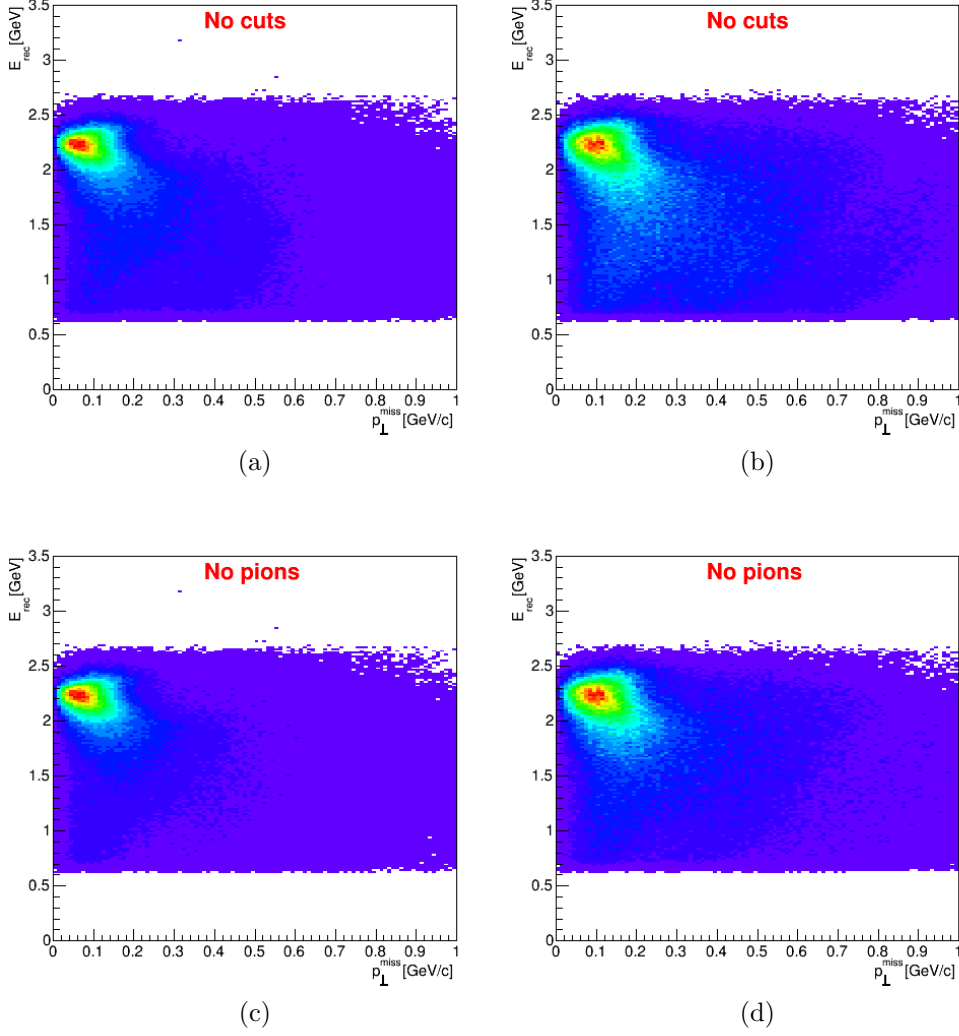


Figure 81: Reconstructed energy E_{rec} obtained using Eq. 7 as a function of the total perpendicular momentum of the scattered electron and the knockout nucleon system for ^4He and ^{12}C targets at 2.2 GeV before (top plots) and after (bottom plots) pion rejection cuts. (a),(c) ^4He ; (b),(d) ^{12}C .

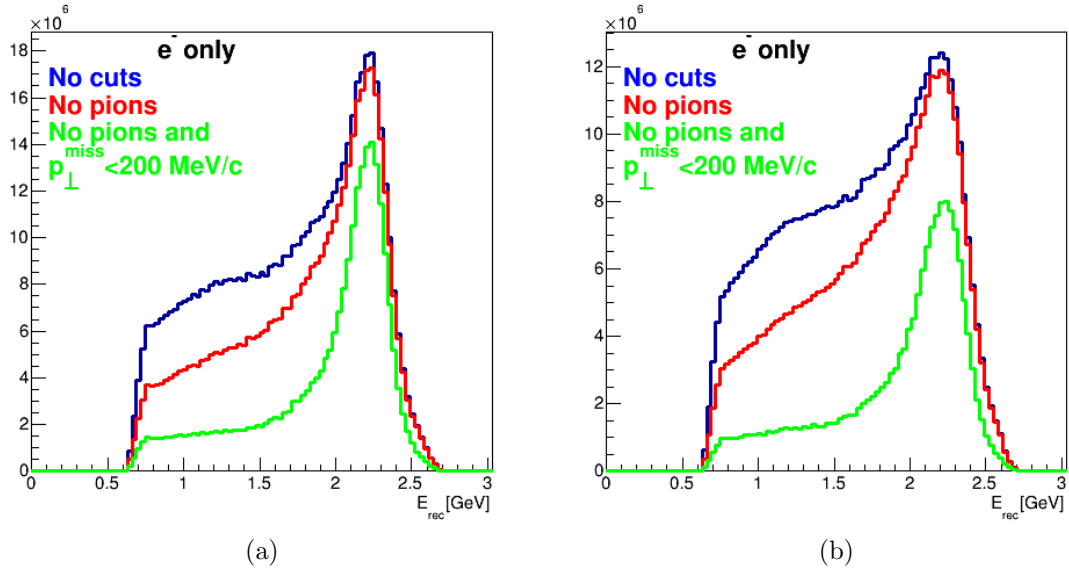
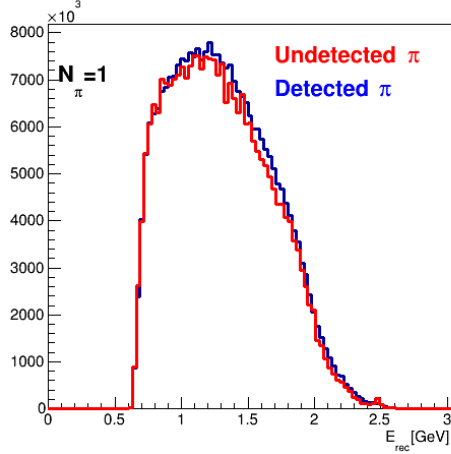
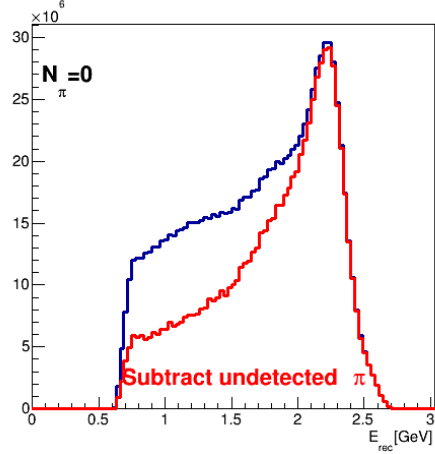


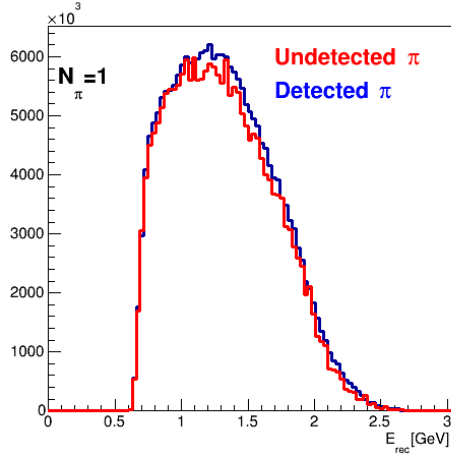
Figure 82: Reconstructed energy E_{rec} of $A(e, e')$ obtained using Eq. 7 with no cuts (blue), with pion rejection cut (red) and with cut on total perpendicular momentum of the scattered electron and the knockout nucleon system $p_{\text{perp}} < 200$ MeV in addition to pion rejection cut for ^4He and ^{12}C targets at 2.2 GeV (a) ^4He ; (b) ^{12}C .



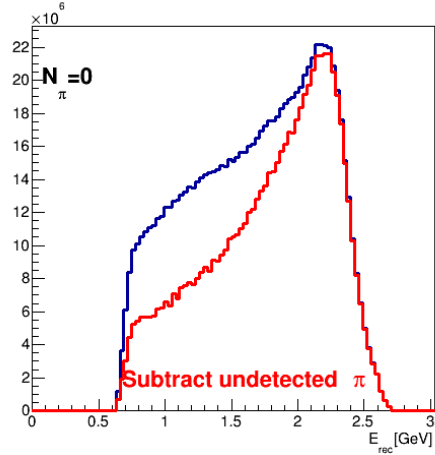
(a)



(b)

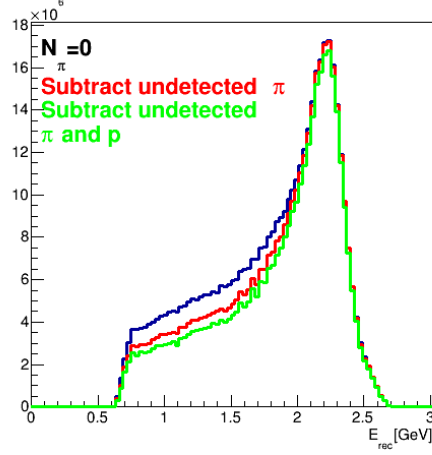


(c)

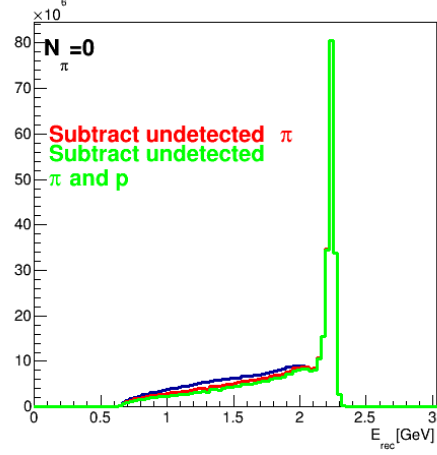


(d)

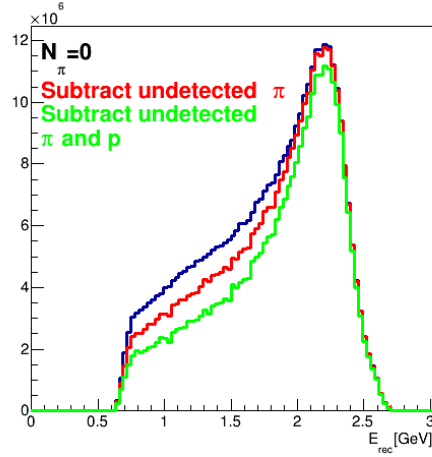
Figure 83: The E_{rec} obtained using Eq. 7, for detected (blue) and undetected (red) 1 pion events for (a) ${}^4\text{He}(e, e'\pi^\pm)$; (c) ${}^{12}\text{C}(e, e'\pi^\pm)$ at 2.2 GeV. Reconstructed energy E_{rec} of $A(e, e')$ no pion spectrum before (blue) and after (red) subtraction for undetected pions for (b) ${}^4\text{He}$ and (d) ${}^{12}\text{C}$ targets at 2.2 GeV.



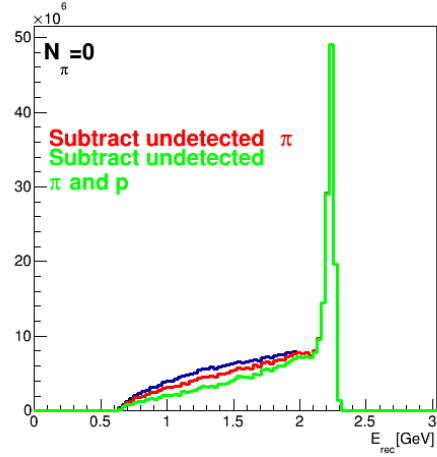
(a)



(b)

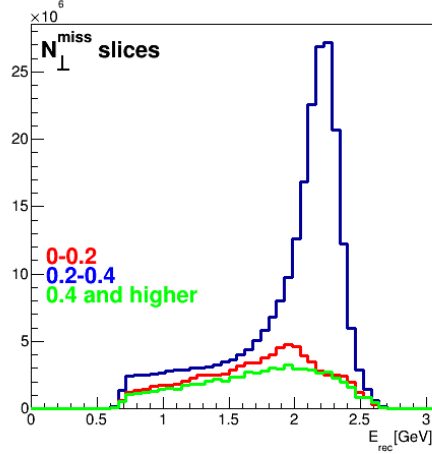


(c)

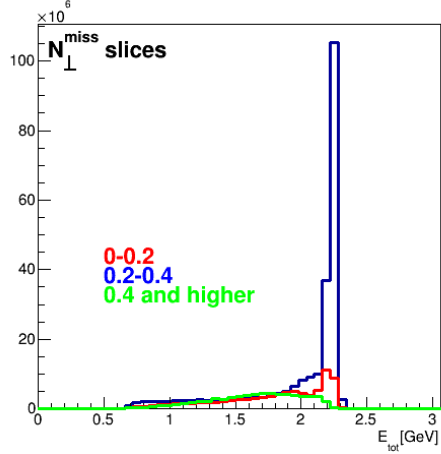


(d)

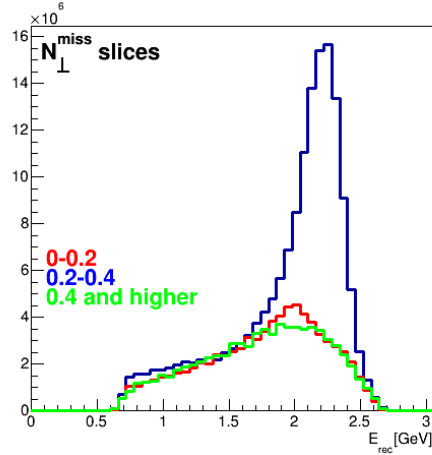
Figure 84: E_{rec} (plots on the left) and E_{tot} (plots on the right) distributions of $A(e, e'p)$ no pion spectrum before subtraction for undetected pions (blue), after subtraction for undetected pions (red) and after subtraction for undetected pions and undetected two proton events (green) for (a), (b) ^4He and (c),(d) ^{12}C targets at 2.2 GeV.



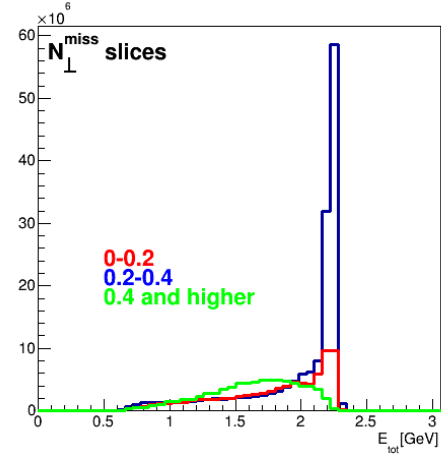
(a)



(b)



(c)



(d)

Figure 85: E_{tot} ((b) and (d)) and E_{rec} ((a) and (c)) distributions of $A(e, e'p)$ no pion spectrum after subtraction for undetected pions and undetected protons for three different regions of p_{perp} ($0-200$ MeV/c, $200-400$ MeV/c and 400 MeV/c and higher) for (a), (b) ^4He and (c), (d) ^{12}C targets at 2.2 GeV.